Towards the Automated Recognition of Assistance Need for Drivers with Impaired Visual Field

Dissertation
der Mathematisch-Naturwissenschaftlichen Fakultät
der Eberhard-Karls-Universität Tübingen
zur Erlangung des Grades eines
Doktors der Naturwissenschaften
(Dr. rer. nat.)

vorgelegt von
Enkelejda Kasneci geb. Tafaj
aus Diber, Albanien

Tübingen
2013

Tag der mündlichen Qualifikation:	10.09.2013
Dekan:	Prof. Dr. rer. nat. Wolfgang Rosenstiel
1. Berichterstatter:	Prof. Dr. rer. nat. Wolfgang Rosenstiel
2. Berichterstatter:	Prof. Dr. med. Ulrich Schiefer

To Zohela, for all the joy and happiness she brings into my life.

Acknowledgments

First and foremost, I would like to thank my husband and my best friend, Gjergji, for his love, help, inspiration, patience, and belief in me and my work. I would like to thank my parents for all their sacrifice and continuous help, and my sisters for their love and support. I am also indebted to my parents and sister in law for their help, support, and love.

This work would have not been possible without the scientific advice of my supervisor Prof. Dr. Wolfgang Rosenstiel. He has been a source of motivation and an inspiring example. I am grateful to him for his supervision, the opportunities he gave me, and his mentorship.

I would like to express my gratitude to Prof. Dr. Ulrich Schiefer for his expert opinion, motivation, and fruitful collaboration during this work. I am also indebted to his team, especially, Elena Papageorgiou, Katrin Aehling, Janko Dietzsch, and Martin Heister.

I would also like to express my appreciation towards my colleagues and collaborators Katrin Sippel and Thomas Kübler at the Department of Computer Engineering who have contributed to the quality of this work. Also my former students Christian Uebber, Sebastian Hempel and Benjamin Jogsch deserve my gratitude for their contribution to the software tools developed during this work. I would also like to thank my colleagues and Margot Reimold at the Department of Computer Engineering for their support.

The driving studies would have not been possible without the support of Daimler AG, who gave us the possibility to use the moving-base driving simulator, and FZI Karlsruhe, who provided a high-tech dual-brake vehicle for the on-road study. Precious financial assistance was provided by PFIZER Pharma GmbH, MSD, SHARP & DOHME GmbH, and the Wilhelm-Schuler-Stiftung. All these cooperation partners and financial supporters deserve my gratitude.

Abstract

Mobility enabled through driving is a crucial aspect of today's social lives. It concerns young and elderly people and is critical for those among us suffering from visual field defects. Since driving primarily involves visual input, such people are often considered as unsafe drivers and banned from driving, although several recent studies, including our own, provide evidence that even severe visual field defects can be compensated through effective visual search strategies. In this context, this work pursues the challenging vision of adaptive driving assistance systems that take the visual deficits of the driver into account to enable a safer driving experience. The main challenges towards this vision are: (1) individual analysis and detection of visual field defects, (2) online analysis of visual search behavior, and (3) integrated analysis of visual deficits, search behavior, and traffic objects to identify and draw the driver's attention towards potential hazards. Each of the above challenges is approached by customized methods. For (1), a mobile method for the assessment of the visual field and an algorithm for the recognition of the type of the visual field defect are proposed. For (2), an online probabilistic method is combined with algebraic analysis of the driver's gaze. For (3), a detailed analysis of the driving scene is combined with the above methods to reliably detect hazardous traffic objects that might be overlooked by the driver. The methods were evaluated on real-world data from driving experiments with patients suffering from visual field defects. In combination, they improve over state-of-the-art techniques by being flexible, adaptive, and reliable. The feasibility of detecting objects that might be overlooked by the driver, and thus an adaptive assistance need, is demonstrated in different user studies.

The methods developed in this work have a broad applicability that reaches beyond the driving context. Their application to a variety of tasks involving visual perception might help better understand its underlying mechanisms. Some of these tasks are already being investigated and will also be presented in this thesis.

Zusammenfassung

Die Erhaltung der Mobilität bis ins hohe Alter ist ein wichtiger Aspekt für die Teilnahme am sozialen Leben. Vor allem das Fahren spielt in diesem Zusammenhang eine entscheidende Rolle. Da das Fahren hauptsächlich auf visuellem Input beruht, können visuelle Defizite die Fahrtauglichkeit beeinträchtigen, z.B. wenn verkehrsrelevante Objekte zu spät oder gar nicht wahrgenommen werden. Von fortgeschrittenen Gesichtsfelddefekten betroffene Personen werden daher oft vom Fahren ausgeschlossen. Viele Studien, einschließlich unsere eigenen, zeigen jedoch, dass Gesichtsfelddefekte durch explorative Augen- und Kopfbewegungen kompensiert werden können. Patienten, die ein solches Explorationsvermögen aufweisen, können durchaus eine gute Fahrleistung erbringen. Zudem könnten Assistenzsysteme, die die individuelle Gesichtsfeldeinschränkung des Fahrers berücksichtigen, um ihn adaptiv zu unterstützen, einen wesentlichen Beitrag zur Erhaltung der Mobilität leisten.

Diese Arbeit verfolgt die herausfordernde Vision der adaptiven, individuellen Fahrassistenz für Personen mit Gesichtsfelddefekten. Im Rahmen dieser Dissertation wurden Grundlagen zur Erkennung des individuellen Unterstützungsbedarfs erforscht. Hierfür müssen drei Aufgaben gelöst werden: (1) Analyse des individuellen Sehdefizits, (2) Echtzeitanalyse des Fahrerblicks zur Identifikation wahrgenommener Objekte und (3) integrierte Analyse des Fahrerblicks, des visuellen Defizits und der Information aus der Fahrszene, um die Aufmerksamkeit des Fahrers in Richtung der Objekte zu lenken, die übersehenen werden könnten.

Zur Erfassung des individuellen, visuellen Defizits wurde (1) eine Methodik zur schnellen und mobilen Messung des Gesichtsfelds und zur automatischen Klassifikation der Gesichtsfelddefektmuster entwickelt. Zur Echtzeitanalyse des Fahrerblicks wurde (2) ein effizientes Verfahren entwickelt, das ein probabilistisches Modell mit Methoden der linearen Algebra kombiniert. Diese Verfahren wurden mit Informationen aus der Fahrszene integriert, um (3) potentiell übersehene Gefahrenobjekte zu identifizieren. Alle Methoden wurden in Fahrexperimenten im realen Straßenverkehr und im Fahrsimulator der Daimler AG evaluiert. Die Machbarkeit einer Echtzeiterkennung des individuellen Unterstützungsbedarfs wurde ebenfalls in diesen Studien getestet.

Die Integration dieser Methoden verbessert den Stand-der-Technik hinsichtlich der Flexibilität, Adaptivität und Zuverlässigkeit. Obwohl die Aktivität des Fahrens als primäre Anwendungsmöglichkeit gesehen werden kann, können die im Rahmen dieser Arbeit entwickelten Methoden breitere Anwendung finden und dadurch zum besseren Verständnis der Mechanismen der visuellen Aufmerksamkeit beitragen.

Contents

1 Introduction

1.1 Motivation

Driving is a complex task that involves a wide variety of cognitive subtasks, such as steering, lane keeping, changing gears, paying attention to traffic signs and participants, controlling the speed, attending to hazardous objects and situations, etc. Scientific analysis of this cognitive task suggests that visual information accounts for up to 90% of driving-related inputs [158], and that even slight disorders in processing this kind of input can have fatal consequences. Reduced visual capabilities are not always obvious; therefore, the assessment of the visual acuity and visual field are important elements of driving ability tests. Common and severe visual impairments that can considerably affect driving capabilities are the so-called *binocular visual field defects*, where the visual field of both eyes is impaired at the same location. Two kinds of such defects are the *homonymous visual field defects* and *glaucoma*. The former occurs mainly after a stroke, whereas the latter is associated with the degeneration of the optic nerve. According to current directives, subjects suffering from binocular visual field defects affecting the central 20 degree region of the visual field are prohibited from driving [36].

Unfortunately, since visual field defects positively correlate with age [62, 121, 124], and as a result of demographic aging, the number of drivers with reduced visual functioning is expected to increase in the coming years. For the affected people, this often means a reduction in mobility, since many of them are considered as unsafe drivers. Mobility, however, will remain an essential aspect of the social life of young and elderly people. Although people suffering from visual field defects are often banned from driving, there is evidence that people who have developed a good visual exploration capability can compensate their impairment by performing frequent head and eye movements (e.g., towards their visual field defect). Hence, instead of a driving prohibition, one should think about ways to assist the affected drivers. For example, a driving assistance system that adapts to individual visual deficits, might help people maintain or even improve their driving fitness, and hence, their mobility and quality of life.

Today's driving assistance systems build on numerous sensors to provide assistance for specific tasks, such as automatic parking, lane keeping, intelligent speed control, emergency braking assistance, and many more. However, many of these tasks are independent of the driver's abilities, let alone her visual deficits. Moreover, the corresponding systems are geared towards reliable, deterministic performance; they do neither adapt to new traffic situations and nor to individual driving capabilities. For example, emergency braking assistance systems are relatively crude in nature, as they are

typically applied as the last mean to avoid an accident.

In this work, we are interested in more fine-grained methods, which take the driver's visual field defects into account to identify overlooked hazardous objects in real-time, possibly without distracting or patronizing the driver.

Besides driving assistance systems, efforts toward autonomous driving [88, 161] have come a long way since their beginnings [114]. For a safe navigation, modern self-driving cars use numerous sensors to analyze position, speed, traffic situation, road conditions, etc. The goal of related projects is to take away the burden of driving from human drivers and shift it to the inbuilt autonomous car system. However, despite the reported driving safety [88] of such systems, there are still many unanswered questions, especially concerning the legislation of driving, e.g., who is responsible in case of accidents, which insurance company covers the costs, etc.

All the methods developed in this thesis leave the burden of driving, and thus the whole responsibility, to the human driver. Their aim is to assist the driver's visual exploration by taking the individual visual deficits into account. In this sense, our methods are rather related to adaptive driving assistance systems, which are of great interest to the automobile industry. In fact, for the experimental evaluation of the proposed methods, our industrial cooperation partner, Daimler AG, in addition to the continuous help and expertise also provided free access to the latest driving simulator equipment (which involves costs of 4000€ per hour) for several days.

The overarching vision of this work is the synergistic combination of such methods as a first step towards the development of driving assistance systems that smoothly guide the driver's visual attention towards potential traffic hazards. This work lays important cornerstones for the implementation of such systems.

1.2 Challenges

While the need for adaptive driving assistance systems is obvious, their design and implementation is highly challenging. Studying and analyzing the visual search behavior of drivers with visual field defects may provide many insights into parameters and strategies that are crucial for driving-related visual exploration. Driving assistance systems could highly benefit from such insights.

However, there are many challenges that are related to the analysis of the visual field in the context of driving:

- **Individual analysis of visual field deficits** There are numerous diseases that may incur impairments of the visual perception. In consequence, there are also various types of visual field defects; their classification is based on patterns of impaired areas

of the visual field. Distinguishing reliably between the different types of defects is challenging even for expert ophthalmologists. Hence, a main challenge here is the reliable detection of the visual field defect type from visual field measurements, especially in the mobile context, where the measurement equipment should be portable and easy-to-use.

- **Online analysis of visual search behavior** People suffering from visual field defects often develop visual exploration strategies that may compensate for the visual deficits. A compensatory exploration strategy often consists of frequent eye and head movements towards the visual field defect area. Therefore, the main challenge here is the real-time detection of the driver's *scanpath*, which consists of *fixations* (i.e., when the gaze is focused on an area of interest), *saccades* (i.e., fast eye movements that enable a shift of the gaze focus), and *smooth pursuits* (i.e., smooth eye movements that enable the visual pursuit of moving objects). A reliable detection of the above scanpath components lays the foundation for the detection of potentially overlooked traffic hazards.

- **Integrated analysis of visual deficits and search behavior** Gaze guidance for drivers with visual impairments is particularly challenging, as it has to be performed under consideration of the specific type of the visual field defect. Moreover, effective visual exploration can only be identified by means of an integrated analysis of the driver's visual field, search behavior, and the objects of interest in the driving scene. Aligning these analysis tasks needs more than reliable analysis components that work in separation. A synergistic integration poses several requirements, such as adaptivity, online performance, and reliability.

1.3 Contribution

In this work, we have addressed all the above challenges by first developing: (1) a method for the mobile analysis of individual visual field deficits, (2) an algorithm for the online analysis of visual search behavior, and (3) a system that combines the above methods for the integrated analysis of visual deficits and visual search behavior. An overview of this system and its components is given in Figure 1.1.

As shown in Figure 1.1, a mobile measurement component, the *Tübingen Mobile Campimeter* (TMC), is employed to assess the visual field. The results of the TMC are forwarded to a scotoma classification method, which recognizes the type of the visual field defect. Devices for tracking the gaze of the driver deliver raw data that is processed by a scanpath analysis component. This latter component detects fixations, saccades, and smooth pursuits of the driver, which are subsequently aligned with the information from the driving scene to detect potential hazards. All these components lay the foundation for the overarching vision of gaze guidance in driving scenarios.

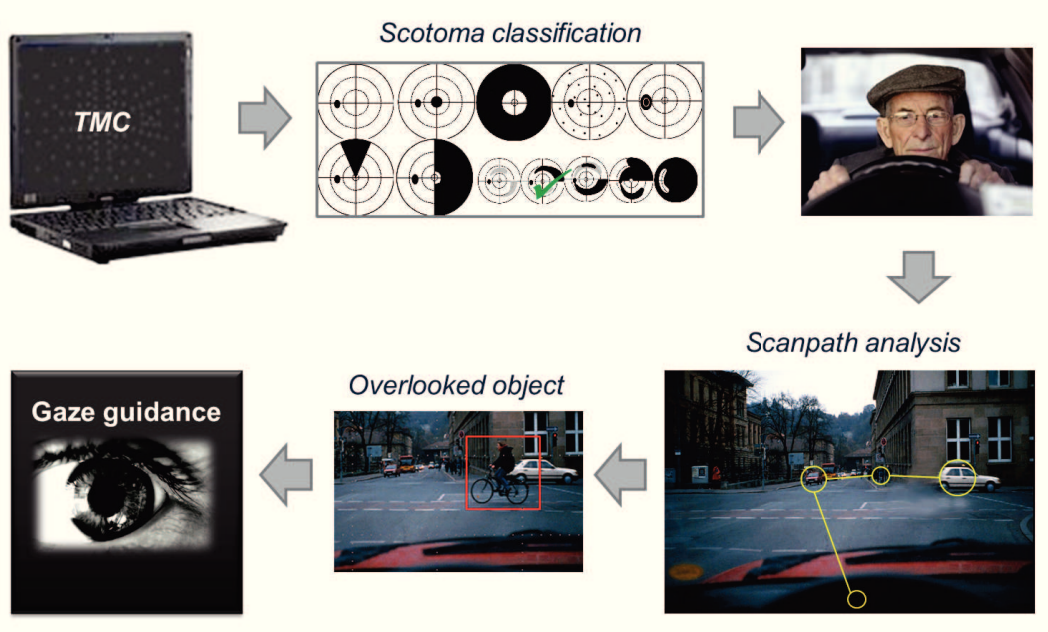

Figure 1.1: Overview of components and methods for the integrated analysis of visual field defects and visual search behavior in alignment with scene information.

In a second step, we have evaluated the practical viability of the above system in two different studies (an on-road study and a driving-simulator study) with patients suffering from binocular visual field defects and healthy-sighted control subjects.

The above research has been published in renowned conferences and journals: For example, the work on the mobile measurement of the visual field has been published in the Proceedings of the 19th Imaging and Perimetry Society (IPS 2010) [152] and in Automotive meets Electronics (AmE 2010) [153], the research on the classification of visual field defects was published in the Proceedings of the 8th IASTED International Conference on Biomedical Engineering (BIOMED 2011) [146]. The algorithms for the online scanpath analysis were published in the Proceedings of the ACM Symposium on Eye Tracking Research and Applications (ETRA 2012) [148] and in the Proceedings of the 23rd International Conference on Artificial Neural Networks (ICANN 2013) [150]. The evaluation results of the feasibility studies have been submitted for publication to Plos One [151], Journal of Vision [77], Vision Research [138], and to Traffic Psychology and Behaviour [78].

Research on the integration of the above methods was published in the Proceedings of the 24th IEEE International Symposium on Computer-Based Medical Systems (CBMS 2011) [149]. A novel method for the assessment of the exploratory field of view was published in the Proceedings of the 6th International Conference on Health Informatics (HEALTHINF 2013) [147].

1.4 Structure

After an introduction to the basics of visual processing and the measurement of the visual field in Chapter 2, the Tübingen Mobile Campimeter for the mobile assessment of the visual field will be presented in Chapter 3. Chapter 4 is devoted to an automated, rule-based method for scotoma classification. An online scanpath analysis method will be presented in Chapter 5. Chapters 6 and 7 will present studies showing the feasibility of an integrated online analysis of the visual field defects and visual search behavior in alignment with information from the driving scene. Other application areas of the methods developed in this thesis will be in the scope of Chapter 8, before concluding in Chapter 9.

2 Visual perception

As the visual input accounts for up to 90% of the driving related-inputs [158], intact visual functioning is a crucial prerequisite for safe driving. The european traffic safety regulations require a binocular visual field of at least 120° in the horizontal extension [36]. Furthermore, subjects suffering from binocular visual field defects affecting the central 20° area are prohibited from driving [76].

In order to understand the impact of visual field defects on driving, this chapter will introduce some basic concepts of visual perception that will be relevant throughout this interdisciplinary thesis. Section 2.1 will explain the concept of visual field and methods for its measurement. Visual field defects and their categorization will be in the scope of Section 2.2. A special focus will be on two types of severe visual field defects, namely *glaucoma* and *homonymous visual field defects* (HVFDs). The focus of Section 2.3 will be on the characteristics of eye movements as a prerequisite for visual perception. Finally, based on findings from previous studies, in Section 2.4, the impact of visual field defects on driving will be discussed.

2.1 The visual field and its measurement

The *visual field* (VF) is the area that can be perceived without any head or eye movement. The monocular visual field describes the area that can be seen with only one eye, spanning ovally approximately 60°, superiorly (the upper half of the VF), and nasally (the vertical half of the VF, near the nose), $70-75°$ inferiorly (the lower half of the VF), and up to 100° temporally (lateral vertical half of the VF) [163]. Due to optical limits of the eye ball and facial features, e.g., nose, the visual fields of the left and right eye may be different. The healthy binocular visual field that considers the visible area of both eyes spans up to 135° vertically and up to 200° horizontally [120, 163].

Perhaps the most apt metaphor describing the visual field has been introduced by H. M. Traquair[1], who describes the visual field as a three-dimensional spatial model, which can be viewed as an "[...] island of vision surrounded by a sea of blindness" [163], illustrated in Figure 2.1. The contours of the island represent various levels of retinal sensitivity with the central peak at the *fovea*, which is the retinal location with greatest sensitivity (sharpest vision). The outer borders correspond to the least sensitive areas in the peripheral visual field [163]. Hence, the slope of the island towards the periphery represents diminishing

[1] Harry Moss Traquair (1875-1954), ophthalmologist and perimetrist.

retinal sensitivity. The physiologic blind spot is represented as a deep well at 15 degrees temporal to the peak of the island.

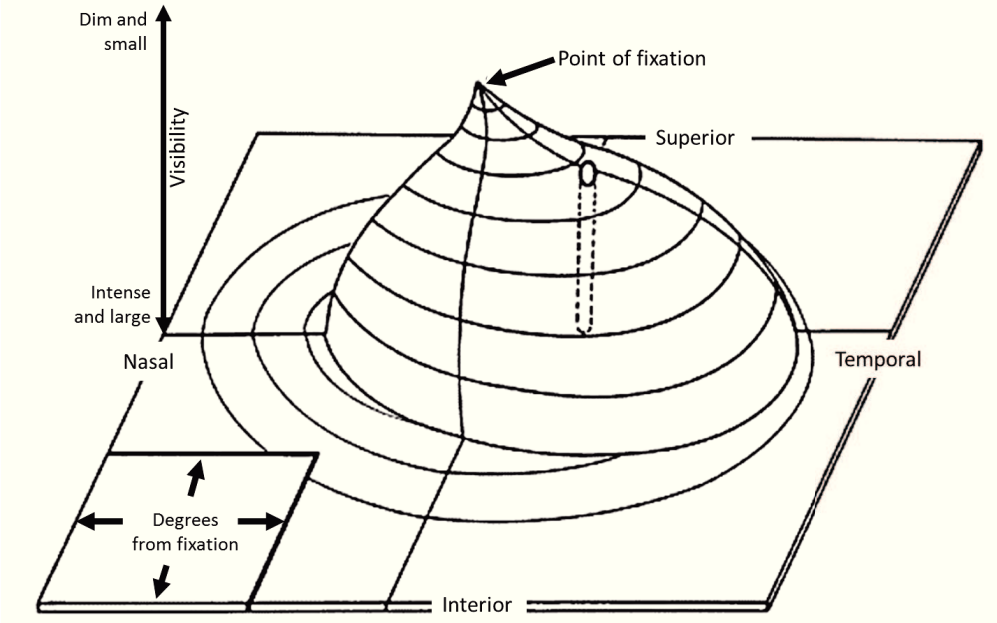

Figure 2.1: The visual field (of the right eye) represented as an island of vision by H. M. Traquair. The highest peak of this island represents the fovea (the retinal location with greatest sensitivity). Towards the periphery of the island, the retinal sensitivity decreases. The outer borders correspond to the least sensitive areas in the peripheral visual field. The deep hole at 15 degrees temporal to the peak represents the physiologic blind spot. Figure was taken from [2].

The measurement of the visual field, i.e., *perimetry*, is very important in the realm of disease management, especially in blindness management [163]. It consists of measuring the sensitivity, mostly in terms of *differential luminance sensitivity* (DLS), of the visual perception as a function of location in the visual field [130]. The most common types of perimetry are the *kinetic* and the *static* perimetry. In both types of perimetry, test objects, most commonly light stimuli, are projected onto a uniform background. The subject (with head fixated and eyes kept stable on a fixed stimulus) is asked to confirm stimulus perception by pressing a button. No response to a stimulus projection is interpreted as failure to see the stimulus. Areas at which stimuli are not perceived or only perceived when the stimuli have high light intensity are called *visual field defects* (VFD) [130], also referred to as *scotoma*. Static and kinetic perimetry are performed by computer assistance using cupola perimeters, such as the Octopus perimeter shown in Figure 2.2(a).

During *static* perimetry, the size and location of a stimulus is kept constant, while its luminance varies until the dimmest stimulus that can be seen by the subject is identified. From the pattern of responses, a threshold estimate can be obtained. The higher the density of stimuli locations and the number of luminance levels, the more precise the

measurement of the visual field, but the longer the examination time. Long examination time may introduce fatigue artifacts and result in reduced attention of the patient, which may interfere with the examination quality.

The most common visual field examination concerns the central 30° visual field. The spatial arrangement of a 30° stimuli grid used in examinations with the Octopus cupola perimeters is presented in Figure 2.2(b). It consists of 192 concentrically arranged stimuli locations. In order to achieve such a high spatial resolution, a so-called threshold-related, slightly supraliminal (i.e., above the threshold of sensation) strategy is applied. This means that at each location the luminance of the presented stimulus is chosen slightly above the presumed age-correlated luminance value at that location. A bracketing (up and down) strategy for local threshold estimation is applied only in case the initially presented stimulus is not perceived.

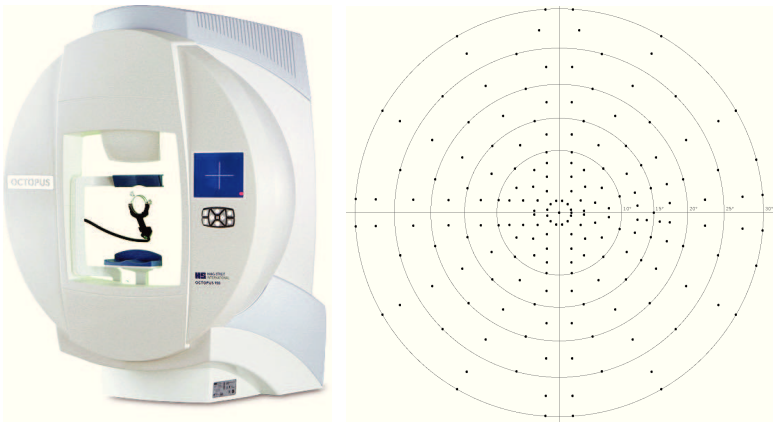

(a) (b)

Figure 2.2: (a) Octopus 900 cupola perimeter (figure from the Octopus 900 user manual of Haag-Streit Inc. Koeniz, Switzerland [50]), (b) a test grid with 192 stimuli locations used for the measurement of the central 30° visual field (figure provided by the University Eye Hospital Tübingen).

Figure 2.3(a) depicts an example of a static perimetric result. Locations of perceived stimuli are marked by black dots. Rectangles represent stimuli locations with reduced visual perception, i.e., such stimuli are perceived only at high luminance level. These locations correspond to *relative scotoma*. The darker the rectangle, the lower the sensitivity at that location. Black-filled rectangles represent stimuli locations with severely reduced luminance sensitivity down to no light perception, i.e., *absolute scotoma*.

In *kinetic* perimetry, a perimetrist moves a stimulus of constant luminance almost perpendicularly toward the assumed visual field defect (scotoma) border. The position at which the presented stimulus is detected marks the boundary of the intact visual field. An example result of semi-automated kinetic perimetry is depicted in Figure 2.3(b). The

(red) dotted line represents the boundary of the intact visual field. This perimetric result indicates a right-sided HVFD, i.e., the loss of visual perception in the right hemifield.

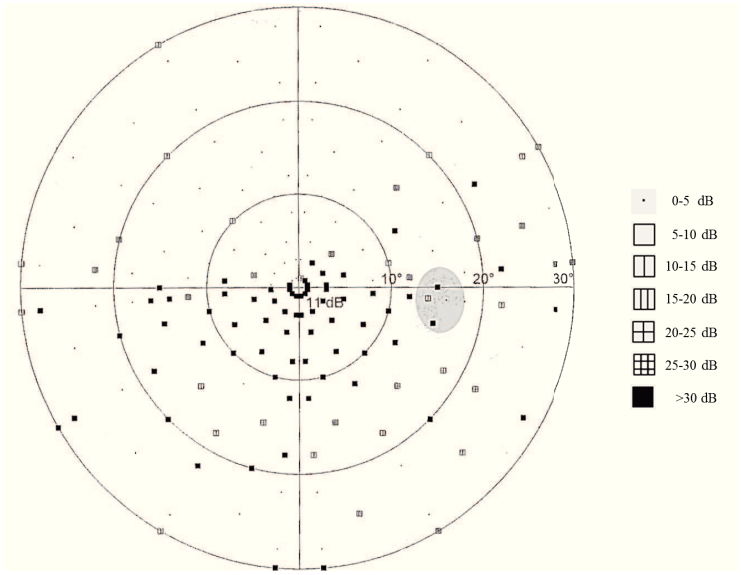

(a) Static perimetric result of the central 30° visual field area (right eye) measured with an Octopus cupola perimeter

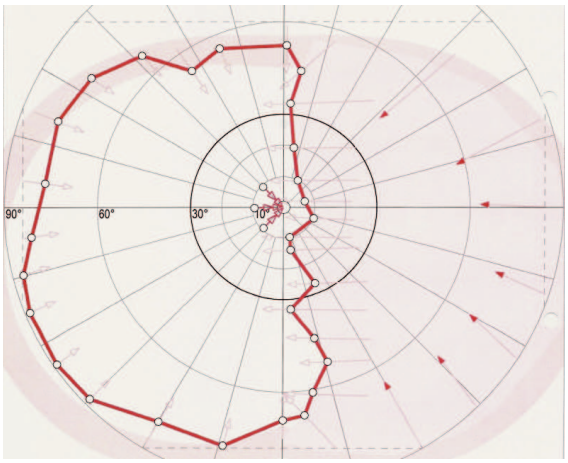

(b) Binocular semi-automated 90° kinetic perimetry

Figure 2.3: Examples of perimetric results: (a) result of a static perimetric examination of a subject with a severe central visual field defect. The black dots represent the locations of perceived stimuli. Rectangles mark locations of reduced visual perception, i.e., relative VFDs (relative scotoma). Black rectangles represent stimuli locations with no visual perception, i.e., absolute VFD (absolute scotoma). (b) shows the result of a standard semi-automated kinetic perimetric examination, where the (red) dotted line represents the boundary of the intact visual field. According to this result, the subject can perceive only those stimuli that are presented within the left hemifield. Figures were provided by the University Eye Hospital Tübingen.

2.2 Visual field defects

Visual field defects usually occur due to damages to anatomical structures that are associated with the visual process. This includes insufficiencies in the retinal structure, lesions of the nerve fibres or in the brain. The type of the visual field defect depends on the location of the lesion [117]. Figure 2.4 illustrates the organization of the visual pathway and, on the right panel, several types of visual field defects which are associated with lesions along it. As shown in this schematic view, visual information from the left side of the scene (1) is transported to and processed in the right brain hemisphere (6) and vice versa. The nerves transporting the visual information from the eye to the brain cross in the optic chiasm (5), which results in information from the same side of each eye being transported and processed next to each other (e.g., see nerves crossing (6)).

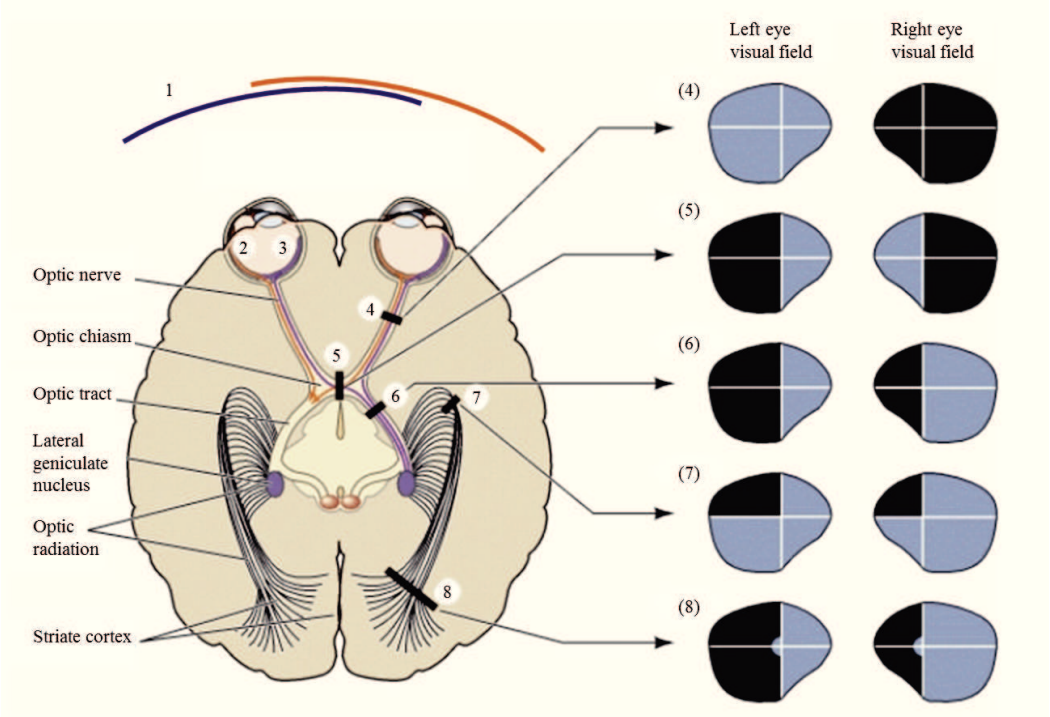

Figure 2.4: Schematic view of the visual pathway and its structures. The left visual hemifield (1) is seen by the nasal side of the retina (3); analogously the right side of the visual field is seen by the temporal (2) side of the retina. The nerve fibers cross in the optic chiasm (5); from there on nerves transporting information about the same side of the visual field run next to each other. The right panel shows visual field defects that are the result of lesions to the associated structures in the visual pathway: (4) complete loss of vision in the right eye, (5) heteronomous hemianopsia, (6) left-sided homonymous hemianopsia, (7) left superior quadrantanopsia. (8) left-sided homonymous hemianopsia sparing the central visual field. Figure was adapted from [117].

The retinal area at which the optic nerve exits the eye and leads back into the brain is known as the blind spot. Due to missing receptors in the retina, no visual information can

be perceived from this area. However, we are mostly unaware of these blind spots. As the blind spot locations in the eyes are symmetrical to each other, the information of one eye can compensate the loss in the other eye. Thus, although the healthy visual field contains one natural scotoma, it does not lead to inconvenience in everyday life. As illustrated in Figure 2.5(a), the visual scene can be perceived without loss of information.

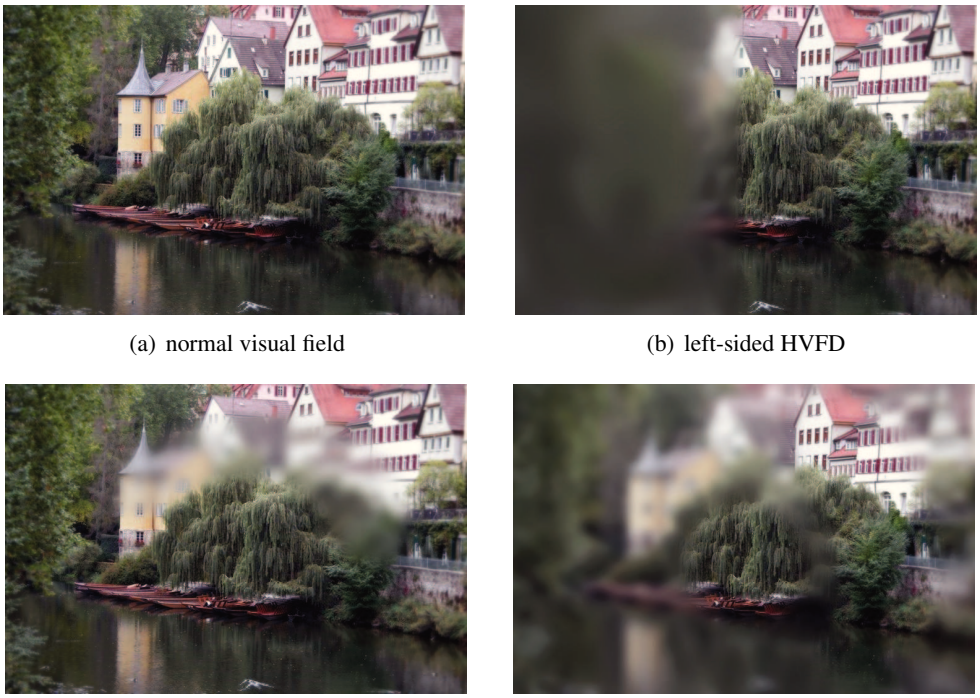

(a) normal visual field (b) left-sided HVFD

(c) early-stage glaucoma (d) late-stage glaucoma

Figure 2.5: (a) shows a scene as it would be perceived by a healthy-sighted person, (b) depicts the perception of the same scene as in (a) with a left-sided HVFD, which would result from a lesion behind the optic chiasm. (c) and (d) show different stages of glaucoma due to degeneration of the optic nerve.

Due to a stroke, brain surgery, traumatic brain injury or tumors, the transportation or processing of the visual information along the structures presented in Figure 2.4 can be corrupted [106]. Post-chiasmal lesions of the visual pathway (as marked by location (6) in Figure 2.4) cause contralateral HVFDs, i.e., the loss of vision on the same side of both eyes, which respects the vertical midline as depicted in Figure 2.5(b). The most common causes of HVFDs are stroke (in approximately 70% of the cases), brain tumor, and trauma [65].

Figures 2.5(c) and 2.5(d) show different stages of glaucoma, another severe visual field defect type occurring due to degeneration of the optic nerve. It is a characteristic optic neuropathy leading to (usually arcuate) visual field defects that follow the course of the affected retinal nerve fibers.

A categorization of visual field defects was proposed by the Tübingen Scotoma Classification Scheme [100], which distinguishes 7 main types of VFDs. Figure 2.6 depicts each type and describes briefly its particular features. Note that this classification scheme has been proposed by expert ophthalmologists with long-term experience. Based on this scheme and expertise, in Chapter 4, a rule-based classifier for the recognition of VFDs will be presented.

In case of *binocular visual field defects*, i.e., when both eyes are affected at the same location, the affected persons may experience severe inconveniences in everyday life. As HVFDs and glaucoma (especially late-stage glaucoma) are among the most severe impairments of the visual field, patients suffering from these diseases are in the focus of this work. Both types of impairments will be discussed in more detail in the following subsections.

2.2.1 Homonymous visual field defects

As introduced above, HVFDs describe the loss of visual perception in the same relative position in both eyes. In literature, HVFDs affecting one half of the visual field are often referred to as *homonymous hemianopsia*. In this work we will refer to both, homonymous hemianopsia and *quatranopsia*, where a quarter of the visual field is affected, as HVFDs. An example of quatranopsia was already shown in Figure 2.4 (7). HVFDs usually occur after a stroke and can highly interfere with the quality of life of the affected people [110]. Unfortunately, in developed countries, stroke is the third most common cause of death after heart disease and cancer. On the other hand, with the decreasing stroke mortality rates, people often have to live with their impairments, including severe impairments of the visual field [49]. According to [43], the prevalence of homonymous hemianopsia is estimated to concern 0.8% of patients over 50 years of age. Approximately 30% of all stroke patients and 70% of those who had a stroke involving the posterior cerebral artery suffer from HVFDs [106, 173]. Alone in Germany, from approximately 550,000 brain-injured patients per year, 135,000 suffer from visual impairments (mostly HVFDs) [110]. In an extensive review of medical records of patients with homonymous hemianopsia between 1989 and 2004, Zhang et al. [171] reported that a spontaneous improvement of homonymous hemianopsia occurs in approximately 60% of patients within the first three months after the brain injury. However, a high number of affected persons have a persistent impairment of the visual field. Often, patients suffering from HVFDs report difficulties in processing scenes, and studies with patients suffering from HVFDs have reported differences to healthy-sighted subjects in the scanning behavior. The main reason for this difference is that HVFDs may lead to inefficient or disorganized scanning, longer search times, or to the omission of relevant scene objects [27, 105, 110, 172]. In consequence, affected people may experience severe limitations in several everyday tasks such as reading, walking, driving, etc., since objects on the blind side are often overseen.

Normal visual field: Less than 7 relative defects may occur anywhere in the visual field, but not in the edges of the grid. No defect clusters besides the physiological blind spot are visible.

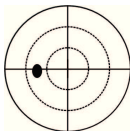

Central scotoma: Absolute or relative defect that occurs mainly within 5° eccentricity without respecting the vertical or the horizontal meridian. Other types of defects within the central visual field are the *Paracentral scotoma* (normal blind spot position) and the *Centrocecal scotoma* (extending from the blind spot towards the central area symmetrically above and below the midline).

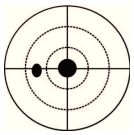

Concentric constriction: Continuous visual field loss sparing the central visual field.

Glaucoma: Progressive defect that occurs in five stages [5], from relative visual field defect (left) to massive absolute defect (right).

Diffuse visual field defect: More than 7 relative defects that are disseminated across the visual field.

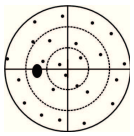

Blind spot enlargement: Defect involving at least two points that are contiguous with the blind spot.

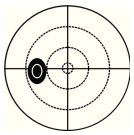

Sector- oder wedge-shaped defect: Wedge-shaped defect respecting neither the vertical nor the horizontal meridian.

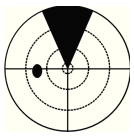

Hemianopic: Defect respecting, at least locally, the vertical meridian.

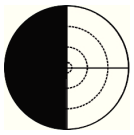

Others: Defects that cannot be attributed to any of the above mentioned classes.

Figure 2.6: Tübingen Scotoma Classification [100].

In literature, several training strategies for the extension of the visual field of patients with HVFDs have been proposed. One technique is based on *visual restorative function training*, i.e., visual stimulation of the border area between the blind and the intact visual field [10, 11, 67, 68, 105, 107, 112]. As the reported findings have been contradictory, this method has been strongly debated [10, 112]. Another approach of visual field extension aims at eliciting eye movements towards the visual field defect [57, 122]. However, other authors could not confirm that eye movements towards the visual field defect would lead to a compensation of the visual field defect [67, 94].

2.2.2 Glaucoma

Glaucoma is considered to be the second leading cause of blindness in the world, with approximately 60.5 million people affected (worldwide) in 2010. Due to demographic aging, 79.6 million are expected to be affected by 2020 [118]. Glaucoma is associated with an increased intraocular pressure, which leads to degeneration of the optic nerve [140]. As depicted in Figures 2.5(c) and 2.5(d), the resulting pattern of the visual field defect is usually arcuate, following the damaged nerves where the central visual field and the visual acuity remain intact. Furthermore, as illustrated schematically in Figure 2.6, glaucoma is a progressive eye disease, where the progression process is described by five Aulhorn stages [5]. Progression can often be slowed down by surgery or medical treatment. However, lost areas in the visual field cannot be restored, and a diagnosis is often made when a significant part of the visual field is already lost.

2.3 Eye movements

Visual perception would not be possible without eye movements. Although we are mostly unaware of them, when viewing a scene, our eyes are constantly moving. This way, eye movements enable the fovea, the retinal part of sharpest vision, to fixate different parts of the scene and thus prevent our visual path from sensory adaptation by refreshing our retinal images. These foveal fixations are known as *Areas of Interest*, AOIs for short. Although it is possible to deploy attention without an accompanying fixation, under natural viewing conditions this is quite rare. Thus, eye movements are assumed to be preceded by a shift in visual attention to a subsequent target. However, the whole process of visual perception involves not only the sensory input mechanisms, but also memory, attention, cognition, and decision making [52, 79, 80].

The question, what drives our eyes over a scene, has been raised in early works of Buswell [23] and Yarbus [169] and, since then, has been in the scope of research in different areas. Especially in recent years, since eye-tracking devices have improved and become broadly available, the number of investigations on eye movements has increased. Several approaches modeling the process of visual attention have been proposed and follow mainly two basic paradigms: the *top-down* and *bottom-up mechanism*. The scanpath theory by Noton and Stark [101] suggests that an internal cognitive model of

what we see not only controls our vision, but also drives the sequences of rapid eye movements and fixations efficiently over a scene [115], e.g., when we are asked to identify a specific object in a scene. This is called the top-down mechanism.

The bottom-up mechanism is based on the idea that an object might attract our attention due to particular features, e.g., a person wearing a red shirt among others wearing white. In this example, the red color is the salient feature. Computer-based models of visual attention have mainly focused on the modeling of bottom-up visual attention by automatically identifying possible fixation targets based on image properties [59, 60]. The detailed description of these models is beyond the scope of this work. A review of visual attention models can be found in [80, 133, 157].

Despite extensive research in this area, so far, it has not been possible to predict the sequence of fixations of an observer looking at an arbitrary scene [133]. The difficulty lies in the complexity of visual processing, for which eye movements are essential. Six types of eye movements are involved in visual processing of a scene: *fixations*, *saccades*, *smooth pursuits*, *optokinetic reflex*, *vestibulo-ocular reflex*, and *vergence* [82]. In this work we focus on fixations, saccades, and smooth pursuits. Hence these types of eye movements will be briefly described, highlighting features that are relevant for this thesis. A detailed description of the physiology and characteristics of eye movements can be found in [32, 80].

2.3.1 Fixation

During a fixation the eye is kept relatively stable on an AOI. It can be assumed that during a fixation, the AOI imaged on the fovea is being visually attended to by the viewer. Fixations usually have a duration of about $200-300ms$, although much longer fixations are possible. The length of fixations is an important research topic in itself, as it relates to the visual information to which the observer is attending as well as to her cognitive state [80].

2.3.2 Saccade

A saccade represents a rapid eye movement to reposition the retinal part of sharpest vision (fovea) to fixate different areas of a scene [115]. A saccade occurs at maximum frequency of about $4s^{-1}$ (e.g., during reading) and maximum velocity of approximately $500^{\circ}/s$ [80]. Saccades are performed by both eyes conjugately. As introduced above, a saccade can be triggered in a bottom-up manner, e.g., by a suddenly moving target or a new stimulus, or in a top-down way. Saccade duration varies between $10ms$ and $100ms$ [32]. The reaction time for externally driven saccades is usually $150-200ms$. Furthermore, saccade latency increases with increasing eccentricity [80].

2.3.3 Smooth pursuit

A smooth pursuit occurs whenever the eye follows a moving target [32]. Similarly to saccades, smooth pursuits are conjugate eye movements that are performed at lower velocities of approximately $15^{\circ}/s$ [80]. They are elicited by moving targets and cannot be executed voluntarily without a target that is visually pursued.

2.4 Impact of binocular visual field defects on driving

The driving ability of patients with binocular visual field defects has been investigated in several studies - both in simulated environments and on-road. Numerous assessment approaches have been used, such as the self-assessment of subjects by means of questionnaires, evaluation of the driving performance of subjects by driving examiners or the analysis of scene camera recordings. These approaches will be briefly reviewed in the following paragraphs.

In an early study on the influence of glaucoma on the driving ability, Owsley et al. [104] investigated visual risk factors for vehicle crashes caused by elderly drivers. The authors analyzed the relation between age and the number of accidents each participant was involved in during the last five years. They reported that the restricted useful field of view and glaucoma seem to be the only significant independent predictors of injurious crash involvement [104]. In 2004, McGwin et al. [92] reported that elderly people with glaucoma were safer on the road than their healthy counterparts due to the discipline and the self-control of these patients, e.g., they did not drive by night or on rainy days. In a later work, the same authors found out that the risk of being involved in a vehicle collision is higher for glaucoma patients than for visually healthy control subjects [91]. In 2008, Haymes et al. [53] evaluated the on-road driving performance of glaucoma patients using a checklist completed by a driving instructor and found no significant difference between patients with glaucoma and control subjects.

Several studies that have investigated the driving behavior of subjects with binocular visual field defects have reported a lowered detection rate on the blind side [16], and a positive correlation between the size of the visual field defect area and the degradation of the driving performance [18]. Furthermore, problems with speed matching and lane keeping have been reported for HVFD patients [165].

Overall, as it can be seen, the reported findings regarding the driving performance of subjects with HVFDs are controversial and contradictory. For example, [16, 75, 143, 155] report significantly worse driving performance for HVFD patients than for healthy-sighted subjects, whereas other studies could not entirely confirm these findings [120, 132]. However, the general consensus is that there are large differences between individuals in driving performance and that visual functioning tests are of limited use in identifying unfit drivers [29]. A further consensus concerns the compensation of VFDs through frequent head and eye movements, a finding that has been confirmed in several studies [89,

108, 165]. The bottom line of these studies is that persons who have developed a good exploration capability are able to obtain information from the impaired areas of the visual field.

2.4.1 On-road studies

The driving ability of patients with binocular visual field defects has been investigated in few on-road studies. Elgin et al. [34] assessed the driving performance of patients with HVFDs in an on-road study based on a six point rating scale. They reported that, although HVFD drivers received poorer ratings, they performed comparably to healthy subjects. However, a common problem for HVFD drivers was the lane keeping ability [34]. The same group of authors used a larger number of scoring criteria to assess driving-related parameters such as lane keeping, steering steadiness, vehicle control, speed adjustment and reaction to unexpected events, which were evaluated by driving examiners during the drive [165]. Two years later, the same authors conducted another on-road study with HVFD patients and improved the study design through recordings of the driving scene and the driver, in order to observe head, shoulder, and eye movements. Thus, the evaluation became more objective [166]. Wood et al. [166] reported that some of the HVFD patients were safe drivers, although they had a similar visual field defect as patients who failed the driving test. Thus, although some patients may suffer from the same visual field defects, their visual search performance may vary and depend on their compensatory ability to effectively perform eye and head movements. However, since no eye tracking has been employed in the above mentioned on-road studies, the evaluation of eye movements and compensatory strategies calls for more precise studies, which are not merely based on observations of human evaluators.

The main drawback of on-road studies is the lack of inter-drive comparability, as different traffic situations arise for different subjects. Furthermore, as such studies are very costly, the number of subjects involved is low. Moreover, the choice of technical instruments is of particular importance, e.g., when eye-tracking equipment is used, it has to be made sure that the eye tracker itself does not interfere with the driving performance.

2.4.2 Driving simulator studies

In an early simulator study with HVFD patients, Szylk et al. [143] reported difficulties in lane keeping. In this study, drivers with HVFDs showed more lane boundary crossings and had greater variability in lane position than healthy-sighted drivers. However, the drive was very short ($\sim$5 minutes). Furthermore, due to the small number of subjects involved in the study, their findings were difficult to interpret from a statistical point of view. A later study with HVFD patients was conducted by Schulte et al. [132]. The authors found no significant differences in driving performance between healthy-sighted drivers and drivers with impaired visual field. A further study with HVFD patients was conducted by Bowers et al. [17, 16]. In a simulated drive, the subjects had to detect pedestrians in hazardous situations. They reported that patients with HVFDs had blind-side detection rates that

seem incompatible with safe driving [16]. Furthermore, patients with HVFDs showed difficulties in lane keeping and positioned themselves within the lane in such a way that the safety margin on their blind side could be increased [17]. Thus, HVFD patients seem to intuitively enlarge the safety distance on their blind side.

In a recent study, the effect of HVFDs on collision avoidance of dynamic obstacles at an intersection was investigated under virtual reality conditions [108, 109]. The authors observed a high performance variably among HVFD patients [108]. Furthermore, patients with a good overall task performance showed more exploratory eye and head movements than patients with poor performance, in particular with respect to moving objects that occurred on their blind side [109]. Another descriptive simulator study suggests that HVFD patients who manage to compensate their visual field impairment perform an increased number of saccadic eye movements towards the side of the visual field defect [51]. The authors did not identify head movements as part of the compensatory behavior of these patients. However, this may be due to the more limited field of view used in this study.

Note that the circumstances in which the above studies were conducted were not sufficiently realistic. The employed driving simulators were fixed-base simulators, which do not allow a realistic driving experience. Acceleration forces, circumferential visibility of the virtual reality and the interior of the simulator are essential elements for making such a simulation as realistic as possible. All these elements were missing in the above studies. Furthermore, eye and head movements were not recorded and, in consequence, could not be analyzed thoroughly.

2.5 Conclusion

All in all, the above studies agree on certain aspects: (1) The driving performance varies among individuals, (2) binocular visual field defects do not always lead to poorer driving performance and are thus not necessarily a reason for driving prohibition. In fact, the findings agree that (3) binocular visual field defects can be compensated by effective head and eye movement strategies.

In light of the above findings and the hints that effective visual exploration can mitigate the disadvantages of patients with binocular visual field defects, the goal of providing individual and adaptive driving assistance, e.g., through gaze guidance, becomes more and more important.

3 Mobile assessment of the visual field

An essential requirement for the development of assistance systems for drivers with visual field defects is the mobile and reliable measurement of their visual field to detect areas of impaired vision. Since standard perimetric devices are not portable, they are not suitable for such measurements in the automotive context. For this purpose, we developed a computer-based campimeter, the *Tübingen Mobile Campimeter* (TMC) [152, 153], which enables the mobile, automated, fast, and low-cost measurement of the visual field. Because of its flexibility and ease of use, the TMC can be quickly deployed even by non-experts. In the vision of a driving assistance system that takes the visual field defects of the driver into account, the TMC could be used by an engineer to measure the visual field of the driver and calibrate the assistance system accordingly for individual assistance.

Section 3.1 will introduce work related to the mobile assessment of the visual field. The computer-based Tübingen Mobile Campimeter will be subject of Section 3.2. Section 3.3 will introduce the *Visual Search Examination Tool* (Vishnoo) [149], which was developed in the context of this work and combines the TMC with other configurable search tasks and eye-tracking capabilities. A special feature of Vishnoo is that it enables the detailed analysis of both the visual field and the visual attention. The TMC was evaluated in a user study, the results of which will be presented in Section 3.4. Finally, Section 3.5 will conclude this chapter.

3.1 Related work

As introduced in Section 2.1, perimetry (the measurement of the visual field) is usually performed by computer assistance using cupola perimeters, such as the Octopus device shown in Figure 2.2(a). During a perimetric examination, the differential luminance sensitivity of visual perception as a function of location in the visual field is measured [130]. In static as well as kinetic perimetry, light stimuli are projected onto a uniform background and the user response (usually by pressing a button) is considered as successful stimulus perception, see Section 2.1. The most common visual field examination concerns the central 30° of the visual field.

Admittedly, automated perimetry with cupola perimeters enables a precise examination of the visual field. Unfortunately, such perimeters are not portable and thus not suitable for the measurement of visual deficits in the mobile or automotive context. Driven by the need for mobile assessment of the visual field, e.g., for usage in emergency or intensive care units or for bed-ridden patients, several campimetric methods have been developed.

In *campimetry* the visual field is examined on a flat surface. The proposed approaches include both manual and semi-automated portable solutions [3, 22, 24, 72, 86, 95, 96, 98] and will be briefly reviewed in the following subsections.

3.1.1 Non-computerized methods

Several non-computerized methods have been proposed to assess the visual field, mainly aiming at fast and low-cost assessment of visual field defects. A simple test was proposed by Mandahl [86], where a test card consisting of four red squares surrounding a black dot (fixation target) was used for the rough measurement of visual field defects. Mutlukan et al. [96] developed a multi-fixation chart for glaucoma screening, which was a hand-held screen with a central black test stimulus on a white background and 26 numbered fixation targets arranged around the stimulus at various locations. A commercial campimetric solution that is widely used is the Damato Campimeter (Precision Vision™) [123, 168], which is also a hand-held device available with different stimuli charts.

A new solution, the *Mechanical Tübingen Mobile Campimeter* (MTMC), was introduced by Bruckmann et al. [22]. As shown in Figure 3.1, the MTMC consists of a semi-transparent Plexiglas screen, a bright energy-saving lamp as stimulus source, and a thin lens holder integrated in a chin rest construction that is used for near vision correction. This device uses a subset of the Octopus 30°-grid (see Figure 2.2(b)) consisting of 84 concentrically arranged stimuli locations.

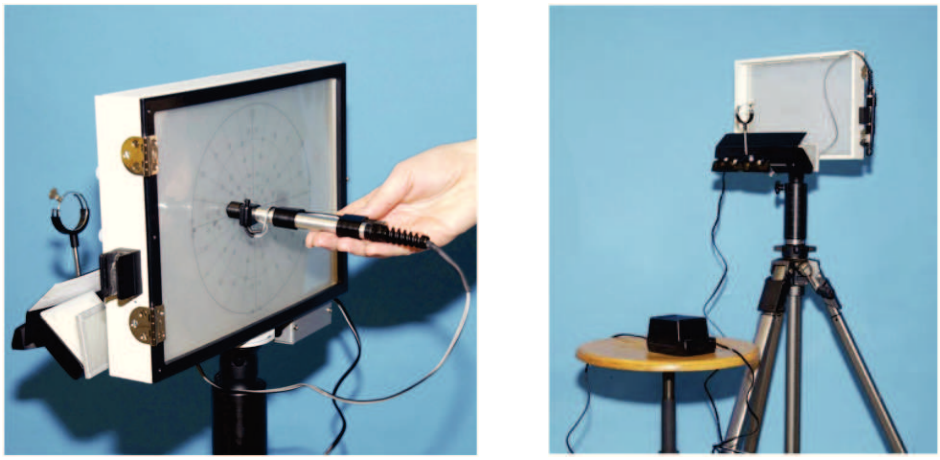

(a) (b)

Figure 3.1: The Mechanical Tübingen Mobile Campimeter [22].

The MTMC allows a fast examination of the visual field, but it lacks flexibility and is thus not suitable for usage in the automotive context, as stimuli have to be manually projected onto the test screen by using a hand-held lamp, see Figure 3.1(a).

The main disadvantage of non-computerized methods over computerized ones is that the examination and its results cannot be processed in an automated manner. Moreover, the examinations require the full examiner's attention. A further disadvantage concerns the inflexibility in the choice of test grids for stimuli locations.

3.1.2 Computerized methods

In [95], Mutlukan presented a computerized examination of the central visual field using low-contrast, static dark-on-bright stimuli and reported high accuracy in the measurement for the presented method.

There are also other approaches, such as the pupil campimetry, where the assessment of the visual field is based on the pupil response to presented stimuli [131]. However, since the pupil response can only be captured at constant ambient light conditions (most precisely in darkness), the method is not applicable to the measurement of the visual field in normal light conditions.

In a recent work, Koiava et al. [72] presented an online visual field test as part of a free-to-use web-based therapy application for patients with HVFDs. An earlier work had already paved the way for computerized multi-fixation campimetric tests; the proposed system is available online [31].

Most of the above devices come with predefined set of test grids, and the inclusion of new test grids is often difficult. Hence, despite the existence of different approaches, none of them has been established in the clinical routine.

3.2 Computer-based Tübingen Mobile Campimeter

The goal for the development of the Tübingen Mobile Campimeter (TMC) has been to provide a portable solution with automated, computerized means for the measurement of the visual field. In contrast to prior campimetric approaches (computerized or non-computerized), the focus for the TMC has been on the flexibility of the measurement process. The TMC enables automated campimetry at full flexibility in the choice of stimuli grids and the stimuli presentation strategy. Furthermore, it has been integrated with the *VIsual Search ExaminatioN TOOl* (*Vishnoo*) [149] which, in addition to campimetry, enables the analysis of the visual search behavior on various search tasks. Vishnoo will be presented in Section 3.3.

The software for the TMC is written in Java and is based on a lean design aiming at efficient measurement of the visual field. Hence, the TMC can be run on common hardware platforms without restriction. One of the most commonly used test grids that is provided by the TMC for the measurement of the central 30° visual field is shown in Figure 3.2.
During the campimetric examination, the subject with a potential visual field defect has

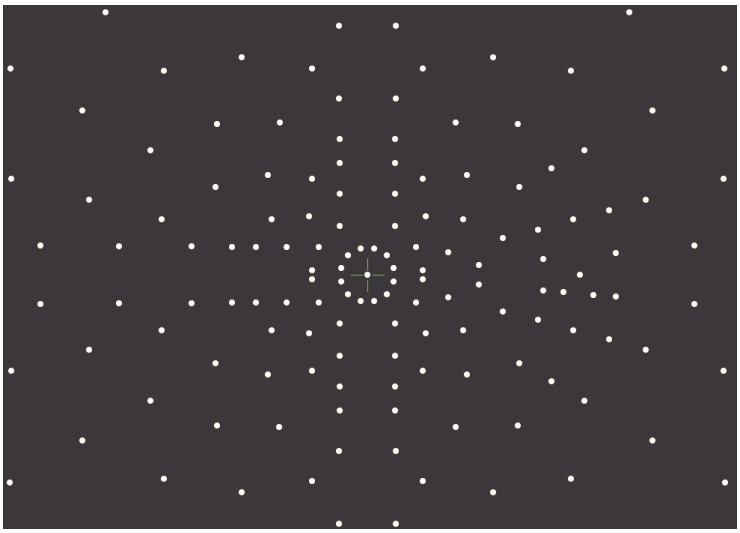

Figure 3.2: Excerpt of the test grid used for the measurement of the central 30° area of the visual field with the TMC [153].

to fixate a stimulus in the middle of the screen. A predefined series of stimuli is loaded from file and the stimuli are displayed successively. The subject can indicate stimulus perception by pressing a mouse button or touchpad.

The architecture of the TMC builds on a Model-View-Controller design pattern with three main components: (i) the *Examination view*, which implements the projection of light stimuli and allows the adaptation to the physical screen parameters, i.e., screen size, screen resolution, and the distance between the subject's eye and the TMC screen; (ii) the *Strategy*, which is responsible for processing the stimuli; and (iii) the *Controllers*, which process the stimuli display and monitor and process user feedback. The examiner can interactively modify an ongoing examination at any time using an external panel.

Three types of examination strategies are made available by the TMC:

- *Suprathreshold (one zone/one level) strategy*: Stimuli are processed in random order. Each stimulus is displayed at maximal luminance, thus no threshold determination is possible. This strategy can be used to assess absolute blind areas of the visual field.
- *German Adaptive Threshold Estimation (GATE) strategy*: GATE [129] is a fast perimetric strategy that provides threshold determination within a short overall testing time by considering for each stimulus location, the results of previous examinations. GATE is based on a modified $4-2-dB$ staircase strategy. This means that when an initial stimulus is detected, it is made dimmer step-wise by 4 dB until it is not seen by the subject. Then the stimulus luminance is increased by 2 dB, and the test is terminated for that stimulus location; the corresponding threshold value is the value between the dimmest stimulus seen and the brightest

stimulus not seen [129]. If an initial stimulus is not detected, in the next step, it is presented at maximum luminance. In case the stimulus is still not detected, the test is terminated for that stimulus location. If the stimulus is detected at maximum luminance, the test is resumed at 4 dB brighter than the initial presentation and successively increased by 4 dB until it is detected by the subject. Then it is made dimmer by 2 dB. Again, the threshold at the corresponding stimulus location is the value between the dimmest stimulus seen and the brightest stimulus not seen.

The GATE strategy begins with an initialization phase, the GATE-i algorithm. Five predefined seed locations are tested with the 4-2-dB stair-case strategy and the smallest absolute deviation from the normal hill of vision is used to translate the values of the entire hill of vision of the testing subject. All remaining locations are tested with stimuli of initial luminance slightly above the previously adjusted values [129]. In a second phase, the GATE algorithm is applied. GATE is basically GATE-i with the difference that the starting stimuli values are slightly brighter than the local thresholds determined at the initialization.

- *Manual*: The examiner defines a list of stimuli over an external panel. The defined stimuli are then processed in the order they appear in the list. This strategy can be used for a more precise localization of a visual field defect, e.g., by defining a higher density of stimuli locations than the density foreseen by standard test grids.

The TMC is part of the software tool Vishnoo [149], which will be briefly introduced in the following section.

3.3 Visual Search Examination Tool

Vishnoo is an integrated framework that combines visual field examination (TMC) with configurable search tasks and eye-tracking capabilities, thus enabling the analysis of both the visual field and the visual attention.

Scientific work on vision and visual search is based on the design and configuration of a specific psychophysical task and the analysis of user behavior. For example, a specific task could be the localization of a randomly positioned target between distractors. Such a task represents a simplified, common visual search activity, e.g., finding a specific item in a supermarket shelf, recognizing an important traffic sign amidst other traffic objects, etc. Such tasks are often designed for a specific study and are typically not made available to the research community for reuse. An important criterion for the repeated simulation of search tasks is a platform that integrates visual search tasks with eye-tracking facilities. Although commercial eye trackers, e.g., Dikablis [35], Interactive Minds Eye Tracker [81], SMI [136] or Tobii [159], and open-source solutions, e.g., ITU Gaze Tracker [126], provide powerful algorithms for eye tracking, synchronization of scanpaths with stimuli events, analysis, and visualization of the visual scanpaths, they do not provide user-friendly interfaces for stimuli generation or task programming. On the other hand,

there are several tools for stimulus presentation in experimental studies conducted in vision research, neuroscience and psychology; examples are: the Psychtoolbox for Matlab [20], PsychoPy [111], SuperLab [26], Presentation [99], or E-Prime [116]. These products offer stimulus delivery and experimental control but they lack the integration of eye-tracking and scanpath analysis.

In contrast to the above products, Vishnoo provides configurable search tasks in combination with eye tracking and visual scanpath analysis. More specifically, it has four built-in visual search tasks and algorithms for eye tracking and visual scanpath analysis. The built-in tasks include a comparative search task, a pop-out task, a conjunctive search task, and a video-plugin for the analysis of the visual processing of a natural scene, images, or videos. In addition to these tasks, Vishnoo also provides the previously discussed TMC module (i.e., the mobile campimetry). The examination workflow is depicted schematically in Figure 3.3.

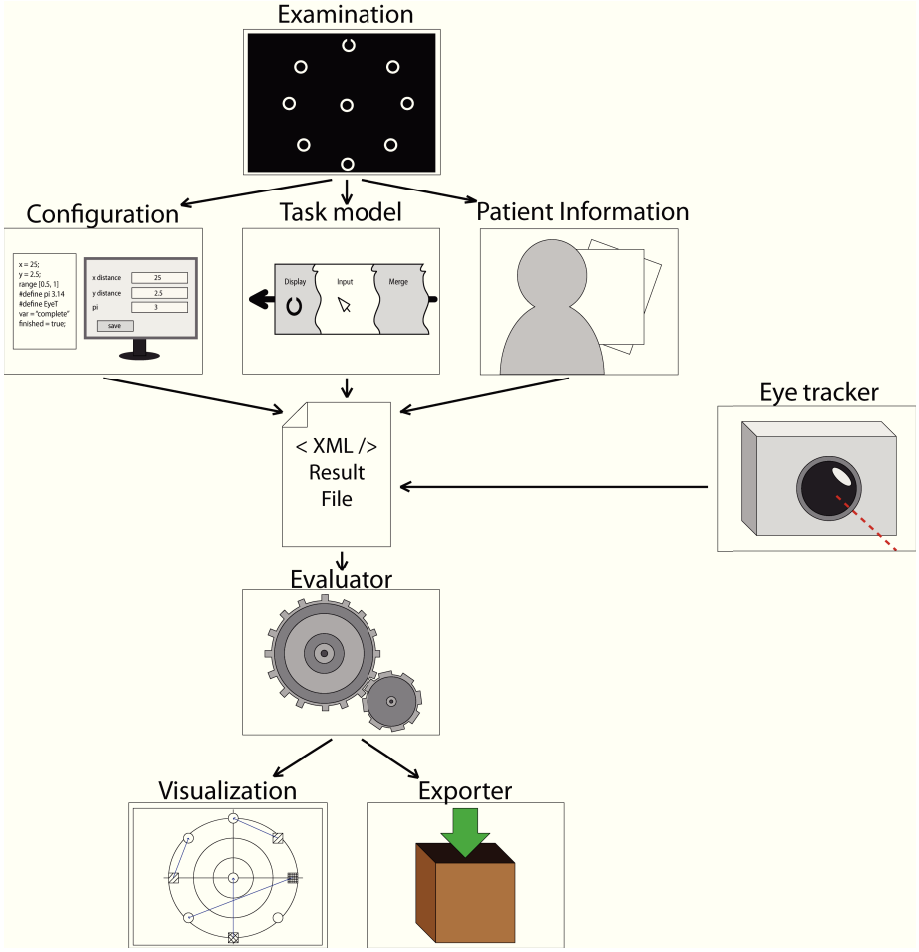

Figure 3.3: Schematic view of Vishnoo's examination workflow [149].

The *examination* module in Figure 3.3 represents either the TMC or one of the four built-in visual search tasks (see also Figure 3.4). The *patient information* module manages the subjects's information, e.g., name, ID, date of birth, and other examination-related parameters. This data is further integrated into the examination result. The *configuration* module allows task-specific configurations, such as the time interval of stimuli presentation. Several visualization and export routines are summarized in the *evaluator* module. Furthermore, several plugins can be linked dynamically during runtime, e.g., for eye tracking.

The four built-in visual search tasks are the following:

- *The Modified Attended Field Of View task, (MAFOV)* is a "pop-out" search task that can be used to investigate the pre-attentive mechanisms of visual perception. A Landolt ring (stimulus of a special shape) is presented among annuli (distractors), see Figure 3.4(a). The user marks the position where she believes to have perceived the presented stimulus. Currently, this task is being used in studies that aim at the analysis of the visual search behavior and exploration capability of subjects with binocular visual field defects.

- *Comparative search tasks*, such as the one depicted in Figure 3.4(b), are typically used to measure the visual span. The user has to detect a local match or mismatch between two displays that are presented side by side. During such visual tasks, subjects may perform very differently depending on the visual scanning strategy they use.

- *Conjunction search tasks* aim at investigating the process of searching for a target that is defined by a combination of two or more features, e.g., shape and color. Vishnoo implements the Machner test developed by Machner et al. [84], as depicted in Figure 3.4(c). For example, a search task might consist in finding all red rectangles in the presented image. In contrast to pop-out tasks such as MAFOV, where the subject's performance depends mainly on the pre-attentive visual perception, in conjunction search, the user's performance depends above all on higher cognitive functions like the visual search strategy and the spatial working memory. Apart from its application in vision research, the Machner test can also be used for rehabilitation in medicine, e.g., training subjects with impaired visual field to employ new search strategies and gain a better perception of their environment.

- *Free search tasks* are enabled by the video plugin, which allows the presentation of natural scene images, such as the example shown in Figure3.4(d). This plugin is useful in research studies aiming at the evaluation or further development of established computational models of visual attention.

During a search task, eye movements are recorded. The visual scanpath can then be analyzed with respect to the number of fixations and saccades. The recognition of the pupil in the recorded images is based on the Starburst algorithm [83], a hybrid eye-tracking

method that combines feature-based and model-based algorithms for the pupil detection in infrared images. More details are presented in [149]. Vishnoo is available for download at: www.vishnoo.de.

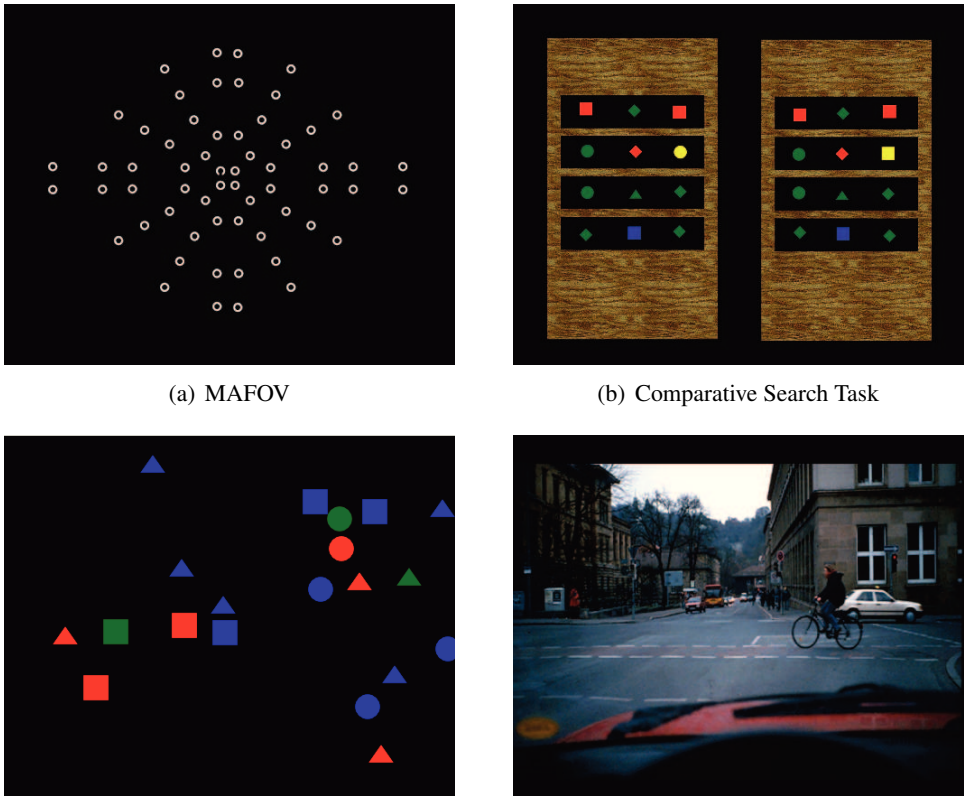

(a) MAFOV (b) Comparative Search Task

(c) Conjunction Search Task (d) Free Search Task

Figure 3.4: Visual search tasks in Vishnoo [149].

In the next Section, we will present the experimental evaluation of the Tübingen Mobile Campimeter based on a user study.

3.4 Evaluation of the Tübingen Mobile Campimeter

The computer-based TMC was evaluated in a pilot user study by comparing its measurements of the blind spot area of nine healthy-sighted subjects to the measurements obtained by an Octopus 101 perimeter for the same subjects. The blind spot is a natural scotoma, an absolute loss of the local differential luminance sensitivity due to missing of light-detecting photoreceptor cells on the retina, where the optic nerve passes through. As the blind spot is a very small area, the concordance of the TMC measurement with the Octopus measurement is a good indicator of the applicability and measurement accuracy of the TMC.

The visual field measurement was performed using the suprathreshold (one zone/one level) strategy, see Section 3.2, where a predefined series of stimuli were projected randomly, only once per location and at maximal luminance. The TMC was run on a 2,4 GHz laptop-PC of screen size 15", at background luminance $10cd/m^2$ and maximal stimuli luminance $270cd/m^2$. The size of a stimulus was Goldmann III, which corresponds to $2mm^2$. We measured the visual field of the right eye of the subjects. For both examinations, the grid type Grid 30-NO, which is suited for testing the central 30° of the visual field and contains 192 stimuli locations (see Figure 2.2(b)), was chosen.

The area and location of the blind spot detected by the Octopus 101 perimeter was compared to the area and location of the blind spot detected by the TMC. In both measurements, the blind spot size was approximated by calculating the minimal enclosing circle of the failed stimuli. Concordance of location and size of the blind spot were then defined as the ratio of intercept areas (i.e., the intersection of blind spot areas detected by the TMC and the Octopus 101) and union areas obtained from both instruments. The results for the measurement of the blind spot for each subject are shown in Table 3.1.

	Measurement with O-101		**Measurement with TMC**		
Subject	**Size (deg^2)**	**Location (deg)**	**Size (deg^2)**	**Location (deg)**	**Concordance**
s1	13.99	[14.2; -0.15]	13.99	[14.2, -0.15]	1
s2	9.69	[15.65; -1.35]	8.37	[16.63, 0.06]	0.86
s3	15.72	[15.53; -2.73]	11.2	[16.05;-2.81]	0.71
s4	8.41	[16.55; -2.9]	8.75	[16.66; 0]	0.96
s5	24.33	[14.75; -2.35]	19.1	[14.94;-1.47]	0.81
s6	9.69	[15.65; -1.35]	9.69	[15.65;-1.35]	1
s7	9.69	[15.65; -1.35]	8.37	[16.63; 0.06]	0.86
s8	13.99	[14.2; -0.15]	13.99	[14.2; -0.15]	1
s9	12.14	[14.75; -1.95]	9.69	[15.65;-1.35]	0.79

Table 3.1: Comparison of the measurements of the blind spot with Octopus 101 (O-101) and the Tübingen Mobile Campimeter (TMC). The location and size of the blind spot are given in degree (deg) and square degree (deg^2), respectively; these measurement units are typically used for the quantification of location and size in ophthalmology. The concordance between the O-101 and TMC measurements is defined as the ratio of intercept areas and union areas of the blind spot obtained from both instruments.

A t-test was run to see whether the difference between the areas and locations determined by the two instruments is significant. For a confidence level of $\alpha = 0.05$, a p-value of 0.43 was found. Thus, the null hypothesis (i.e., that there is no significant difference between the measurements obtained from the two instruments) had to be retained.

As presented in Table 3.1, the visual field measurements obtained from the TMC are highly concordant with the measurements of the Octopus 101 perimeter. The mean concordance in the detected size of the blind spot was 0.89, which can be interpreted as a high agreement between the TMC and Octopus 101 measurements. The average examination time was 5 minutes for Octopus 101 and 4 minutes for the TMC.

As an example, Figures 3.5(a) and 3.5(b) show the blind spot area for subject *s*1 measured with the Octopus 101 perimeter and the TMC, respectively.

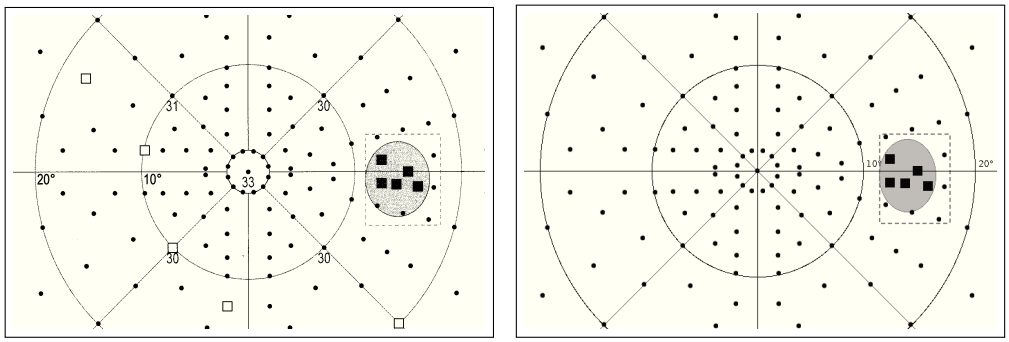

(a) (b)

Figure 3.5: Blind spot detection with (a) the Octopus 101 perimeter and (b) the TMC.

3.5 Conclusion

The Tübingen Mobile Campimeter can reliably assess the driver's visual field at low cost. Furthermore, it is portable on different hardware platforms, user-friendly, and transportable. Although initially developed for the mobile assessment of the visual field in the automotive context, further application scenarios arise in the medical context, such as the usage for the assessment of the visual field in emergency units, bed ridden patients, and intensive care.

Further improvements of the TMC could be achieved through an automated fixation control (i.e., keeping the gaze stable on a central stimulus) during the visual field measurement. As the TMC is integrated in Vishnoo, so far, fixation control is enabled through an infrared camera and the algorithms for pupil recognition provided by Vishnoo. A simpler solution might leverage webcams, as they are available in almost every portable PC. However, such a solution would require more robust eye-tracking algorithms, as the representation of the pupil size would be much smaller than in the present solution, more sensitive to changing light conditions, and, in consequence, harder to track.

4 Rule-based classification of visual field defects

The location, extent, and shape of a visual field defect, as determined during perimetry or campimetry, e.g., by using the Tübingen Mobile Campimeter, is crucial for the adequate diagnosis of the underlying disease of the visual system. In the automotive context, the extent and location of visual field defects is necessary for the individual assistance of the driver. Thus, the reliable classification of visual field defect types from visual field measurements is of particular importance. A classification scheme for visual field defects, the Tübingen Scotoma Classification Scheme, was already introduced in Section 2.2, Figure 2.6. Such a classification of visual field defects from perimetric results is based on expert know-how and long-term experience and is used for the manual classification of visual field defects in the clinical routine. A major requirement for the automated recognition of visual field defect types (from perimetric measurements) is that the reliability of the approach be comparable to the classifications provided by a field expert. Therefore, in this work, an automated rule-based classifier that emulates the decision strategies of expert ophthalmologists has been developed. The classification method is in the scope of this chapter.

Section 4.1 will review related work in the field of automated scotoma classification. The main characteristics of the input data for the proposed classification algorithm as well as the evaluation data set will we presented in Section 4.2. Section 4.3 will give an overview of the overall method. A technique that builds on *Self-Organizing Maps* and *Hierarchical Agglomerative Clustering* to derive new features for the defects revealed in perimetric examination results will be subject of Sections 4.4 and 4.5. The derived features concern size, shape, and location of defect clusters. Once these parameters are derived from the perimetric results, a rule-based classifier leverages them for the reliable recognition of the type of visual field defects. This classifier will be presented in Section 4.6. The experimental evaluation of the method will be discussed in Section 4.7, and Section 4.8 will conclude this chapter.

4.1 Related work

The automated classification of visual field defect types from perimetric examinations is a challenge, especially because of the high variability of the disease manifestation in perimetric results. This challenge has been addressed in several approaches, usually using machine learning algorithms.

Most of prior research aiming at disease management, more specifically disease progression, has focused on the automated classification of glaucomatous defect patterns or the detection of glaucoma progression from perimetric examinations. As described in Section 2.2.2, glaucoma is a progressive disease that is becoming more present due to demographic aging. As appropriate treatment can slower its progression, it is important to detect a worsening of the visual function. Moreover, patients suffering from glaucoma but not showing visual function damage or very slow disease progression would be spared treatment [102].

In 1993, Keating et al. [69] used a back-propagation neural network for the classification of visual field data. They trained and evaluated their approach on simulated data of a subset of visual field defect classes. The reported accuracy varied between 74% and 96%, depending on the class of the visual field defect. A similar approach was presented in 1994 by Goldbaum et al. [48]; it was based on a two-layered back-propagation neural network to distinguish glaucoma from a healthy visual field with an overall accuracy of 74%. However, the evaluation was conducted on a small data set. Another approach was presented by Mutlukan and Keating in the same year. Their classification method used a three-layer back-propagation neural network: an input layer, where each unit corresponds to a stimulus location, a hidden layer of processing units, and an output layer, where each unit corresponds to a particular type of visual field defect pattern [97]. The network was trained on simulated visual field examination results. The classification accuracy reported by the authors ranged from 65% to 100% on genuine perimetric results, depending on the class of the visual field defect. A back-propagation neural network was also used by Brigatti et al. [21] to identify glaucoma progression. The achieved sensitivity and specificity values were 73% and 88%, respectively. Further work hinting at the potential of neural networks in glaucoma diagnosis and management was presented by Bizios et al. [13]. The authors reported sensitivity and specificity values of 93% and 94%, respectively. Another approach using neural networks to detect glaucoma patterns in perimetric results was presented by Henson et al. [55], where a 2-dimensional Kohonen self-organizing feature map (SOM) organized on a square grid was used. However, the authors do not report whether and how their method can be applied to the detection of other visual field defect types. In 2002, Jürgens et al. [64] presented a classification method based on a two-layer neural network to classify the visual field defect classes contained in the Tübingen Scotoma Classification Scheme. The neural network was evaluated on a test set of 1000 perimetric results with an overall classification accuracy of 95%. However, it remains unclear how the accuracy of the algorithms varies with decreasing quality of the data from perimetric results. In contrast, our approach has been evaluated on perimetric results of different quality levels.

The main drawback of methods that are based on neural networks is their dependence on the training procedure, as the overall classification performance can be negatively influenced by missing correlations and noise in the input data [7, 55]. In contrast, a rule-based classifier is not necessarily dependent on correlations in the training or input data.

In 2004, Fink [39] presented an approach that was based on an Hopfield-attractor network, which obtained its input from perimetric examination results. In this approach, predefined visual field defect patterns were stored as attractors of the network. In an iterative relaxation process, the states of the neurons were determined dynamically. Fink reported an overall classification accuracy of about 80% on a relatively small data set [39]. The main advantage of this approach over the above mentioned methods is that no iterative neural learning process is required. Although several recommendations were outlined by the author to improve the classification performance, an improved version of the method has not been presented yet.

Apart from neural network algorithms, several other approaches have been proposed. In 2002, Goldbaum et al. [47] compared different machine learning classifiers regarding their accuracy for the classification of glaucomatous visual field patterns. Multilayer perceptrons (MLP), support vector machines (SVM), mixture of Gaussians (MoG), and mixture of generalized Gaussians (MGG) were compared. The classifiers were trained and tested by cross validation on normal and glaucomatous perimetric results. Best classification results (accuracy $\approx$70%) were achieved by MoG [47]. In a later work, the same authors compared quadratic discriminant analysis (QDA) to support vector machines with Gaussian kernel (SVMg) to classify glaucomatous visual field defect patterns [15]. They reported that QDA was superior to SVMg in terms of sensitivity. The performance of both classifiers was measured in terms of the areas under the receiver operating characteristic curve (AUC-ROC). The AUC-ROC values for SVMg and QDA were 0.85 and 0.92, respectively. In another approach, Goldbaum used a variational Bayesian Independent Component Analysis mixture model to find glaucomatous clusters [45]. The sensitivity and specificity values achieved by this approach on a relatively small data set were 68.6% and 98.4%, respectively [46].

Note that many of the above approaches have a relatively narrow focus (e.g., recognition of glaucoma) and their extension and applicability to the recognition of other defect types has not been investigated. In general, despite the diversity of methodologies, especially for the detection of glaucoma and its progression, reliable progression detection still remains a challenge [102].

In contrast to the above methods, which are highly dependent on training data, in a hand-in-hand collaboration with expert ophthalmologists of the Tübingen University Eye Hospital, we have derived reliable rules that allow the recognition of each of the eight classes of visual field defects (see Section 2.2, Figure 2.6). This has led to a classification method that combines expert rules with parameter settings that can be optimized through correlation analysis on real-world, hand-labeled perimetric results.

4.2 Input data

As input data for our classification method, we used results from static perimetric examinations of the central 30° area of the visual field, such as the example presented in Figure 2.3(a). The algorithm was developed for primary usage with Octopus perimeters, such as the Octopus 900 depicted in Figure 2.2(a), but is not limited to this device type.

The stimuli grid used for the examination of the central visual field consists of 192 concentrical stimuli locations. The spatial arrangement of such a stimuli grid was already introduced in Figure 2.2(b). The result concerning the detection of a stimulus location by the test subject is represented by a stimulus vector $s_i = (x_i, y_i, dd_i)$, $i \in \{0, \ldots, 191\}$. (x_i, y_i) represents the position of the stimulus, e.g., in our application, for the central 30° area of the visual field: $x_i, y_i \in \{-30, \cdots, 30\}$. Note that x_i and y_i are not Cartesian coordinates, but azimuth and eccentricity. dd_i represents the defect depth that is related to the measured differential luminance sensitivity (DLS) at location (x_i, y_i). The range of defect values from 0 dB to over 30 dB is subdivided into 7 intervals, i.e., $dd_i \in \{0, \cdots, 6\}$ classes. A perimetric result can be represented as a matrix of stimuli vectors:

$$\mathbf{M} = \left[\begin{pmatrix} x_0 \\ y_0 \\ dd_0 \end{pmatrix} \cdots \begin{pmatrix} x_{191} \\ y_{191} \\ dd_{191} \end{pmatrix} \right] \tag{4.1}$$

In order to evaluate the classification method, 8,868 anonymized visual field examination results that were carried out in the Centre for Ophthalmology at the University Eye Hospital Tübingen during the last years were used. The data was hand-labeled by expert ophthalmologists. In addition, a classification quality, representing the physician's certainty for the identification of the visual field defect, was provided.

Total	Quality 4	Quality 3	Quality 2	Visual field defect class	Label
2,435	690	1,622	123	Normal visual field	C_1
1,080	16	634	430	Central scotoma	C_2
175	13	111	51	Concentric constriction	C_3
4,080	125	2,956	999	Glaucoma	C_4
19	1	16	2	Diffuse visual field defects and artifacts	C_5
430	9	268	153	Blind spot enlargement	C_6
27	0	19	8	Sector- or wedge-shaped defect	C_7
622	105	315	202	Hemianopic defect	C_8
8,868	**959**	**5,941**	**1,968**		

Table 4.1: Distribution of defect types in the perimetric examination results used for evaluation of the classification method.

The classification quality is $q \in \{1,2,3,4\}$, where $q = 4$ is the highest quality level, i.e., the defect type could clearly be identified. In this work, examinations with $q \geq 2$ were considered. Table 4.1 presents the distribution of perimetric results among the defect classes according to the Tübingen Scotoma Classification scheme, presented in Figure 2.6.

Furthermore, several artifacts may occur during examinations due to eyelid or eyebrow anatomy or due to the rim of the correction glass. Such artifacts are schematically depicted in Figure 4.1. Examination results that were prone to such effects were assigned to the defect type *Diffuse visual field defects and artifacts* in Table 4.1.

The eyelid or eyebrow (e.g., when tilting the head forward) may cause difficulties within the upper visual field.

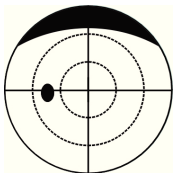

The rim of the correction glass may lead to defects mostly at high eccentricity.

Figure 4.1: Potential examination artifacts [100].

4.3 Overview of the classification method

The recognition of the visual field defect type from a perimetric result is based on clustering and consists of three steps:

1. In a first step, structures in perimetric examinations, i.e., clusters of stimuli locations with impaired visual perception, have to be found. This was conducted using two methods of unsupervised learning, namely *Hierarchical Agglomerative Clustering* (HAC) [33] and *Self-Organizing Maps* (SOMs) [71]. In a two-level approach, SOMs were used to compute prototype clusters, which were then combined to final clusters using HAC.

2. In the next step, for the original perimetric result new features are derived from the clusters found in Step 1, e.g., centroid position, cluster size, average defect depth of stimuli locations in the cluster, etc.

3. Finally, first-order logic rules check the class membership of the enriched perimetric result (i.e., with the above features). The rules have been designed in close collaboration with expert ophthalmologists. Uncertain decision parameters (e.g., decision thresholds) have been optimized by means of correlation analysis.

The details of each of the above steps will be presented in the following sections.

4.4 Clustering for the feature enrichment of perimetric results

The most decisive benefit of the above two-level clustering is noise reduction. As the cluster prototypes computed by a SOM are based on the local density of the data, they are less sensitive to random variations in the original data, e.g., relative defects due to a subject's inattention. As investigated by [87], SOMs outperform hierarchical methods in clustering noisy data, which could also be confirmed by previous work in the context of visual field measurement [55].

For completeness, the concepts of HAC and SOM will be briefly described in the following subsections. A detailed review of these unsupervised methods can be found in [33, 71].

4.4.1 Abstract definition of clustering

The problem of clustering can be stated as follows: Select m centroids (Equation 4.3), and assign all data points from the set I to one and only one cluster, (Equation 4.4), such that the sum of the distances from all points to their respective cluster centroid is minimized (Equation 4.2) [87]:

$$min\ Z = \sum_{I}\sum_{J} d_{ij}\, x_{ij} \tag{4.2}$$

where:

$$\sum_{J} x_{jj} = m, \tag{4.3}$$

$$\sum_{J} x_{ij} = 1\ \forall i,\ \ x_{ij} \leq x_{jj},\ \ x_{ij} \in \{0,1\}\ \forall i,j \tag{4.4}$$

In the above minimization problem, d_{ij} stands for the distance between data point i and the centroid of cluster j, x_{ij} is a binary variable indicating whether data point i is assigned to cluster j, and $x_{jj} = 1$ indicates that the j'th point is the centroid of the j'th cluster; I is the set of n data points, and J is the set of clusters [87].

It can be shown that clustering according to the above definition is an NP-complete problem [87]. Several heuristics have been proposed, which address two difficulties: (i) determining the number of clusters that exist in a data set, and (ii) assigning data points to one of the clusters.

4.4.2 Hierarchical Agglomerative Clustering

HAC is a widely used heuristics that is based on a simple principle: Clusters of points are constructed in a bottom-up manner; starting with each point as a singleton cluster, clusters that are close to each other, according to a predefined similarity or distance measure, e.g., the Euclidean distance, are merged iteratively until a single, all-encompassing cluster remains [61, 154]. Thus, each intermediate level is a combination of two clusters from the lower level. Several agglomerative methods that differ in the way in which clusters

are merged are known. The most prominent methods are described in the following paragraphs.

Single-linkage clustering is based on merging clusters according to a local criterion: The similarity of two clusters c_i and c_j is defined as the similarity of their most similar data points according to a distance function D. As in [40], the linkage function can be defined as:

$$L_{single}(c_i, c_j) = \min_{x \in c_i, y \in c_j} D(x, y) \tag{4.5}$$

The goal of every merge step is to find and merge clusters c_i, c_j that minimize $L_{single}(c_i, c_j)$.

The main drawback of single-linkage clustering is known as *chaining* and describes iteratively growing clusters due to a chain of points that are close to each other [61].

Complete-linkage clustering considers the entire structure of clusters; the similarity, according to a distance function D, between two clusters c_i and c_j is defined by the similarity of their most dissimilar data points. The goal of every merge step is to find and merge a pair of clusters c_i, c_j that minimize $L_{complete}(c_i, c_j)$, which is defined as [40]:

$$L_{complete}(c_i, c_j) = \max_{x \in c_i, y \in c_j} D(x, y) \tag{4.6}$$

This strategy mitigates chaining, but is sensitive to outliers, as a single data point can increase the cluster diameter, thus leading to cluster degeneration and a high variance in cluster sizes [61].

Centroid-linkage clustering defines the cluster distance as the distance between their centroids [40]. The centroid μ of a cluster c is the point y that minimizes the sum of squared Euclidean distances to the other cluster points $x \in c$ [40]:

$$\mu = \arg\min_{y} \sum_{x \in c} \|x - y\|^2 \tag{4.7}$$

The goal of every merge step is to find and merge a pair of clusters c_i, c_j that minimize the linkage function $L_{centroid}(c_i, c_j)$:

$$L_{centroid}(c_i, c_j) = D(\mu_i, \mu_j) \tag{4.8}$$

In our classification method, HAC with centroid-linkage is used on top of a pre-clustering of stimuli locations by means of Self-Organizing Maps to derive coherent defect clusters. The features of such clusters (e.g., size, shape, location) are added as new features to the original perimetric result. The enriched perimetric results are used by the rule-based classification method to determine the visual field defect type.

4.4.3 Pre-clustering through Self-Organizing Maps

The concept of Self-Organizing Maps (SOMs) was introduced by Kohonen, initially for speech recognition [70]. It is an unsupervised learning method that is based on artificial neural networks with competitive learning due to lateral inhibition connections between neurons. In a SOM network, the N-dimensional input data is mapped to a lower dimensional arrangement (grid) of neurons, such that the topological order is maintained [71]. Thus, adjacent units map similar data points. Usually, 2-dimensional grids (mostly rectangular or hexagonal) are used. The particularity of a SOM is that it can be used at the same time for both the reduction of data complexity (by clustering) and the nonlinear projection onto a lower-dimensional space [66]. In the following, the main features of SOMs are summarized; a comprehensive description can be found in [71].

Each neuron, also called *unit*, is assigned a reference vector m_i containing the synaptic weights. These reference vectors are initialized prior to the SOM training, usually randomly. During training, the reference vectors of the map units are iteratively adapted to fit the input data best. Given the input data point x, for each unit, the distance between its reference vector and x is computed. The Kohonen unit c with the minimum distance to x (usually the Euclidean metric is used) is the winner neuron, also called *Best Matching Unit, BMU*, Equation 4.9:

$$c = c(x) = \arg min_i \{\|x - m_i\|^2\} \tag{4.9}$$

Thus, the BMU determines the spatial location of a topological neighborhood of excited neurons, thereby providing the basis for cooperation among neighboring neurons.

In each new iteration step $t+1$, the reference vectors are adapted to the input from the previous iteration step, $x(t)$, according to the gradient descent rule in Equation 4.10.

$$m_i(t+1) = m_i(t) + \alpha(t) h_{ci} [x(t) - m_i(t)] \tag{4.10}$$

$\alpha(t)$ represents the learning rate over time (which typically decreases with learning progress), whereas h_{ci} represents the neighborhood kernel, typically a Gaussian kernel, around the BMU c.

SOM quality measures A question that arises when using SOMs concerns the measurement of the mapping quality. Several methods regarding the topology preservation and vector quantization have been proposed. A survey and comparison of these methods is presented in [113]. In this work, the quality of the SOM was measured based on the *Topographic Error* and the *Quantization Error*:

- The Topographic Error (TE) is measured based on the assumption that the BMU and the second BMU should be adjacent nodes on the map. If this is not the case, the occurrence of a local error is assumed. The total error is computed as the quotient of

the sum of local errors and sample data. Usually TE is a normalized value in $[0, 1]$, where 0 represents perfect topology preservation [113].

- The Quantization Error (QE) is given by the average distance of the input vectors to the unit reference vectors. In consequence, the quantization error can be reduced by increasing the number of units in the lattice.

SOMs are trained considering both parameters, TE and QE, which are orthogonal to each other, i.e., lowering QE may lead to a fine-grained mapping with many topological clusters, whereas lowering the TE may result in a low number of clusters. Hence, TE and QE have to be adapted based on the specific problem.

Figure 4.2 illustrates how the SOM was used in this work for the analysis of visual field defects in perimetric examination results. A perimetric examination result depicting an enlarged blind spot area is shown in Figure 4.2(a). A SOM grid of 12×6 units was trained on the normalized perimetric data from Figure 4.2(a) based on the Matlab SOM Toolbox [1]. Figure 4.2(b) shows the mapping of the SOM units (represented by black circles) on the normalized perimetric data. Note that a 3-dimensional representation has been used for the sake of better visualization. The topographic and quantization error for this mapping were $TE = 0.063$ and $QE = 0.065$. In this example, the visual field defect and the intact area of the visual field form well-separated clusters.

Visualization and clustering of the SOM Several visualization techniques have been proposed for data exploration on the SOM. Perhaps the most widely used is the *Unified Distance Matrix, U-matrix* for short [160]. The U-Matrix visualizes the Euclidean distance between reference vectors of neighboring units, usually color-coded. Note that the U-Matrix is larger than the SOM grid, as it displays the distance between all adjacent units. An example of a U-Matrix for the SOM trained in Figure 4.2(b) is shown in Figure 4.2(c). The distances between units are represented by a gray-scale, where black stands for small Euclidean distance. Implicitly, the U-Matrix visualizes the data clusters mapped by a SOM. As is can be seen in Figure 4.2(c), a bright set of cells separates two dark areas that correspond to the clusters (i.e., of stimuli locations) in the perimetric result. Thus, since the topological order in a SOM is maintained, i.e., data points that are similar in the input space are mapped to adjacent units, SOMs can effectively be used for clustering. Note that separating the clusters of the SOM from Figure 4.2(b) according to the corresponding U-Matrix is straight-forward for the presented example, which was chosen for the sake of a comprehensible demonstration of the method. However, note that in general, the U-Matrix may suggest multiple clusters with non-obvious boundaries between them. For such cases further analysis is needed to separate the clusters. Therefore, we applied HAC on top of the SOM results to separate clusters based on their hierarchical dependencies derived from the centroid-linkage strategy. This was also done to detect the clusters of units on the SOM from Figure 4.2(c). The corresponding dendrogram and the clustering result are presented in Figure 4.2(d).

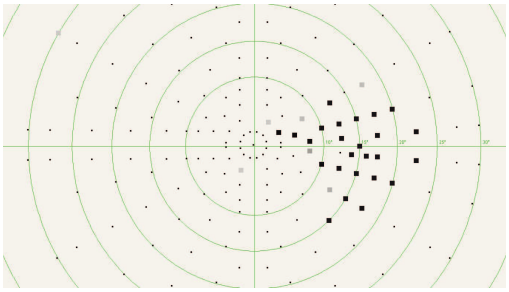

(a) Static perimetric result showing an increased blind spot area

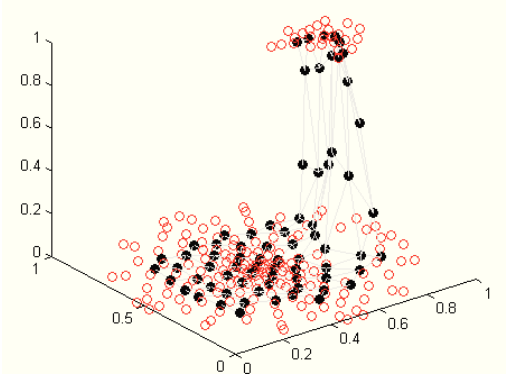

(b) The normalized perimetric data from (a) (red circles) and a mapped SOM with a lattice of 12x6 units (black circles), $TE = 0.063$, $QE = 0.065$; a 3-dimensional representation has been used for the sake of better visualization

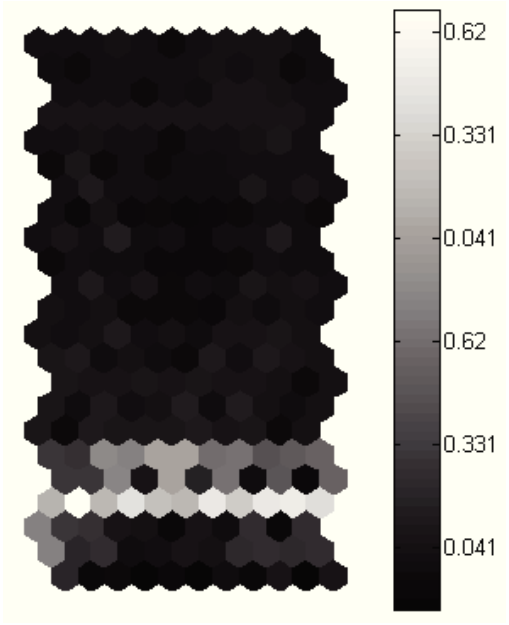

(c) U-Matrix visualizing the Euclidian distance between reference vectors of neighboring units of the SOM from (b)

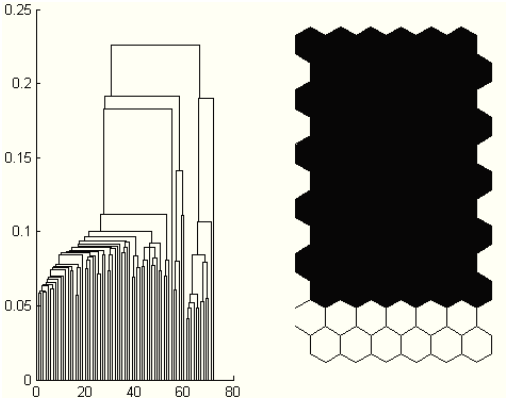

(d) Dendrogram and clusters resulting from HAC with centroid-linkage on the SOM from (b)

Figure 4.2: An example of SOM usage for clustering perimetric results.

4.5 Why SOM-based clustering?

For the scenario of clustering stimuli locations, the SOM-based clustering approach has several advantages over other popular alternatives, such as k-means or expectation-maximization-based methods. Such methods require that the number of clusters is known in advance. In our scenario, we have no prior knowledge on the number of clusters. In the SOM approach, the only parameter that is decisive for the number of clusters is an empirically established threshold on the distance of neighboring neurons. That is, neighboring neurons with a distance greater than the threshold belong to different clusters. While several flat-clustering algorithms can be adapted to take such a threshold into account, they often face the problem of unstable results in the presence of noise. In fact, noise is the most difficult aspect to deal with in the scenario of clustering stimuli locations. Although the example depicted in Figure 4.2(a) is a fairly simple one (we have chosen it for the sake of better presentation of the SOM approach), in most of the cases, the three-dimensional vectors representing the stimuli locations are very noisy, especially with respect to the defect depth value (i.e., the third coordinate). The SOM-based dimensionality reduction handles much of this noise and returns the correct clusters in the overwhelming majority of the cases (see also the experimental evaluation in Section 4.7).

4.6 Recognition of visual field defect classes

The features of the clusters derived by the SOM-based approach (e.g., cluster centroid, cluster size, average defect depth of stimuli locations in a cluster, etc.) are used to enrich the original perimetric result. This enriched result becomes the input of the scotoma classifier by which it is mapped to one of the eight visual field defect classes introduced previously and summarized in Table 4.1.

More specifically, the classifier has been designed as a function $f : \mathscr{X} \rightarrow \mathscr{C}$, $\mathscr{C} = \{C_1, C_2, \ldots, C_8\}$, that maps an input $\mathbf{x} \in \mathscr{X}$ to one of the 8 classes in $\mathscr{C}$ in a way that is similar to how an expert ophthalmologist would decide, namely based on rules derived from frequently occurring observations. Hence, the classification method consists of a collection of rule-based binary classifiers that operate based on a one-versus-all scheme. For each of the 8 classes, a first-order logic rule has been manually assembled by considering decision rules used by ophthalmologists and also by empirically analyzing a hand-labeled data set of perimetric results of quality levels 3 and 4, see Table 4.1. This data set was recommended by an expert ophthalmologist and included 20 representatives of each scotoma class, except for the classes C_5 and C_7, which were represented by 10 perimetric results each. In order to identify appropriate values for some of the input features (i.e., for values that are prone to uncertainty), a correlation analysis was run on this data set with the goal of increasing the accuracy of the scotoma classifier. To this end, the *Matthews Correlation Coefficient, MCC*, was computed on the number of *true positives (TP)*, *true negatives (TN)*, *false positives (FP)*, and *false negatives (FN)* for a

given class: $MCC = \frac{TP \times TN - FP \times FN}{\sqrt{(TP+FP)(TP+FN)(TN+FP)(TN+FN)}}$ [6].

An input $\mathbf{x} \in \mathscr{X}$ consists of the following features:

- the set $\mathbf{M}$ of 192 three-dimensional vectors representing the stimuli locations (see Equation 4.1)
- the number n_d of defects in the perimetric examination result
- the number n_c of clusters derived by the SOM-based clustering
- the set of cluster means $\{\mu_1, ..., \mu_{n_c}\}$
- the set of cluster sizes $\{S_1, ..., S_{n_c}\}$
- the set of the numbers of stimuli locations in each cluster $\{sc_1, ..., sc_{n_c}\}$
- the set containing the average defect depth in each cluster $\{\overline{dd}_1, ..., \overline{dd}_{n_c}\}$

The above features are used to build a binary rule-based classifier for each of the eight classes of visual field defects (see Figure 2.6). The classifiers operate based on a one-versus-all scheme. Although rather rarely, it may nevertheless happen that two or more rules representing different classifiers fire (i.e., become true) on the same input, thus implying ambiguity in the assignment of the perimetric result to a defect class. These cases, however, mostly concern perimetric results of low quality, $q \leq 2$, (i.e., for which the experts themselves were not sure about the exact class). In a pragmatic solution to this problem, the scotoma classifier iterates through the rules and maps the input to the class corresponding to the first rule that fires. In the following paragraphs, the classification rules are presented in the order of their iteration. The characterization of each class is based on the Tübingen Scotoma Classification scheme from Figure 2.6.

Normal visual field (C_1) The normal visual field is characterized by only one cluster of failed stimuli locations, i.e., defects that correspond to the physiological blind spot and few sporadic defects that occur due to the patient's inattention. The correlation analysis on the data revealed a maximum number of 10 relative or absolute defects. Note that this threshold is in accordance with typical thresholds used by expert ophthalmologists, which range between 8 and 11. This number includes the failed stimuli locations within the blind spot cluster $c_{blindspot}$ with centroid $\mu_{blindspot}$ and size $S_{blindspot}$, and few sporadic defects, e.g., due to the patient's inattention. The values $\mu_{blindspot}$ and $S_{blindspot}$ stem from the Tübingen Scotoma Classification scheme and are in accordance with expert knowledge.

$$(n_d \leq 10 \ \wedge \ n_c = 1 \ \wedge \ \mu \approx \mu_{blindspot} \ \wedge \ S \approx S_{blindspot}) \rightarrow C_1 \tag{4.11}$$

Central scotoma (C_2) A central scotoma is characterized by absolute or relative defects that do not respect the vertical or horizontal meridian in the central visual field. A perimetric examination result is assigned to this class if it fulfills the rule

$(RC \vee RCC) \rightarrow C_2$, where RC and RCC are defined in the Formulas 4.12 and 4.13, respectively.

The RC part of the rule stems entirely from expert knowledge: All 13 stimuli locations within 2° eccentricity are checked; if more than 50% of these locations, i.e., more than 6, are defects, the presence of a central scotoma is assumed.

$$[RC]: \quad \sum_{s_i \in M} (\|(x_{s_i}, y_{s_i})\|_2 \leq 2)(\overline{dd}_{s_i} \geq 1)) \geq 6 \tag{4.12}$$

RCC stems also to a large extent from expert knowledge: A *paracentral scotoma* is assumed whenever there exists a central cluster of defects with centroid within 10° eccentricity, containing more than 5 stimuli. The minimum number of stimuli locations within the central cluster was derived from correlation analysis (i.e., MCC analysis) on the data. The value 5 was revealed as a reliable threshold.

$$[RCC]: \quad \exists c_i : \|\mu_i\|_2 \leq 10 \ \wedge \ sc_i \geq 5 \ \wedge \ \overline{dd}_i \geq 3 \tag{4.13}$$

Concentric constriction (C_3) According to the Tübingen Scotoma Classification, see Figure 2.6, this defect type is manifested by an intact central visual field and a peripheral field constriction. Thus, we consider a central (within 15° eccentricity) and a peripheral defect cluster and check their positions. In addition, the average defect depths in the clusters are compared. The defect depth in the peripheral defect cluster is expected to be at least 1.3 times larger than the defect depth in the central cluster. The values 15 and 1.3 were established by means of MCC analysis on the data.

$$\left(\exists c_i, c_j : \mu_i \approx (0,0) \ \wedge \ \forall s_k \in c_i : \|(x_{s_k}, y_{s_k})\|_2 \leq 15 \ \wedge \ \mu_j \approx (0,0) \ \wedge \ \overline{dd}_j \geq \overline{dd}_i * 1.3\right) \rightarrow C_3 \tag{4.14}$$

Glaucoma (C_4) This type of defect is characterized by arcuate-shaped defects. However, the perimetric results for this class only rarely showed well-separated defect clusters as depicted in the schematic view of Figure 2.6. In reality, the defect clusters were often distorted. Furthermore, the five stages of glaucoma reveal different cluster shapes. However, progression detection or distinguishing between the glaucoma stages was not in the scope of this work. The focus was primarily on the detection of blind areas, as their detection is important in the context of driving. A perimetric examination is classified as glaucomatous if there exists a cluster with at least 15 defects spanning over the right and left hemifield according to the rule in Equation 4.15. While a minimum average defect depth of $\overline{dd}_i = 3$ is a typical value observed by experts, the remaining thresholds were established by means of MCC analysis.

$$\left(\exists c_i : \ sc_i \geq 15 \ \wedge \ \overline{dd}_i \geq 3 \ \wedge \ \exists s_j, s_k \in c_i : x_{s_j} > 10 \ \wedge \ x_{s_k} < -10\right) \rightarrow C_4 \tag{4.15}$$

Diffuse defects and examination artifacts (C_5) A diffuse visual field defect is characterized by relative and absolute defects that are spread across the entire visual field. Examination artifacts occur due to eyelid anatomy or when a correction glass is used, see Figure 4.1. A perimetric examination result is assigned to this class, if it fulfills the rule $(RD \vee REL \vee RCL) \rightarrow C_5$, where RD, REL, and RCL are given in the Formulas 4.16, 4.17, and 4.18.

- *Diffuse defects* are defects that are spread across the visual field, see Figure 2.6. Clustering the corresponding stimuli locations typically yields one large cluster encompassing more than half of the visual field (i.e., ≥0.5*VF). Experts also expect to observe an average defect depth of at least 2 in this cluster.

$$[RD] : \exists c_i : S_i \geq 0.5 * VF \ \wedge \ \overline{dd}_i \geq 2 \tag{4.16}$$

- *Eyelid artifacts* occur in the upper visual field, see Figure 4.1. This is found by searching for an isolated defect cluster, i.e., with centroid μ_i in the very upper visual field, between 20° and 30° eccentricity. Furthermore, expert ophthalmologists expect to observe an average defect depth of at least 3 in the defect cluster. Analysis on the data revealed that an upper bound of 7 and a lower bound of 5 on the number of stimuli locations in the cluster further improves the recognition accuracy of this class.

$$[REL] : \exists c_i : 20 \leq |\mu_i|_2 \leq 30 \ \wedge \ 5 \leq sc_i \leq 7 \ \wedge \ \overline{dd}_i \geq 3 \tag{4.17}$$

- *Correction lens artifact* refers to defects that occur when a correction glass is used, since certain stimuli locations are covered up by the rim of the correction glass, see Figure 4.1. The corresponding perimetric examination results are typically characterized by the following features: a cluster of defects in the lower hemifield with centroid between 10° and 20° eccentricity, and a circle of absolute defects at the periphery, between 25° and 30° eccentricity. Further analysis on the data revealed that if in the above defect circle at least 70% of the peripheral stimuli have an average defect depth greater than 2, the recognition accuracy for the class can be considerably improved.

$$\begin{aligned} [RCL] : \quad & \exists c_i : \ \wedge \ 10 \ \leq |\mu_i|_2 \leq 20 \ \wedge \ y_{\mu_i} < 0 \\ \wedge \quad & \frac{\sum_{s_j \in M} (25 \leq \left\|(x_{s_j}, y_{s_j})\right\|_2 \leq 30)(\overline{dd}_{s_j} \geq 2))}{\sum_{s_k \in M} (25 \leq \|(x_{s_k}, y_{s_k})\|_2 \leq 30)} \geq 0.7 \end{aligned} \tag{4.18}$$

Blind spot enlargement (C_6) According to the Tübingen Scotoma Classification, this class refers to defects that occur due to the enlargement of the blind spot. Such cases are typically assumed when there is a defect cluster close to the blind spot area, for which the centroid or the size does not correspond to the centroid or the size of the

normal physiological blind spot cluster. The following is a decision rule used by expert ophthalmologists for this class of defects.

$$(\exists c_i : \mu_i \neq \mu_{blindspot} \ \vee \ S > S_{blindspot}) \rightarrow C_6 \tag{4.19}$$

Sector- or wedge-shaped defects (C_7) This class refers to defect areas in the visual field that are wedge-shaped. A perimetric examination result is assigned to this class, if there is a defect cluster with the following features: (i) it contains more than 8 defect stimuli, (ii) it is not the blind spot, and (iii) the angle between the sides of the wedge-shaped cluster (l_l and l_r) is between 30° and 90°. The values for the minimum number of defect stimuli in (i) and the minimum average defect depth in (ii) were established by means of MCC analysis. The angle between the cluster sides stems from expert knowledge. In order to approximate the sides of a wedge-shaped cluster, first the cluster is split into a left and a right part with regard to the line passing through the origin and the cluster centroid. Then, the points in each of the parts are approximated by a straight line regression through the origin.

$$\begin{aligned}(\exists c_i : \mu_i \neq \mu_{blindspot} \ \wedge \ S_i \neq S_{blindspot} \ \wedge \ sc_i \geq 8 \ \wedge \ \overline{dd}_i \geq 2 \\ \wedge \ 30 \leq \angle(l_l(c_i), l_r(c_i)) \leq 90) \rightarrow C_7\end{aligned} \tag{4.20}$$

Hemianopic defect (C_8) According to the Tübingen Scotoma Classification, this defect class refers to visual field defects that expand over one hemifield respecting the vertical meridian of the visual field. The corresponding perimetric examination results are typically characterized by an impaired left or right visual field side, where most of the stimuli were not recognized. The other half of the visual field is intact, except for the blind spot area and few relative or absolute defects, e.g., due to patient's inattention. To detect this defect type, the algorithm counts the number of defects in each half of the visual field. Correlation analysis on the data, by means of MCC, revealed that a left-sided hemianopic defect is found, if at least 60% of the stimuli locations of the left side (i.e., with x coordinate $x \leq 0$) of the visual field are absolute defects (i.e., stimuli locations with defect depth $dd \geq 3$). The threshold 3 for the defect depth of a stimulus is based on expert knowledge. The right side of the visual field is considered intact, if there are less than 10% of relative defects (i.e., stimuli locations with defect depth $dd \leq 2$). The rule for the detection of the left-sided hemianopic defect is defined by *RHL* in Formula 4.21. The detection of a right-sided hemianopic defect is defined by *RHR* in the Formula 4.22 and is symmetric to *RHL*. In summary, a perimetric examination result is assigned to this defect class if it fulfills the rule $(RHL \vee RHR) \rightarrow C_8$.

$$[RHL]: \ \frac{\sum_{s_i \in M}((x_{s_i} \leq 0)(dd_{s_i} \geq 3))}{\sum_{s_i \in M}(x_{s_i} \leq 0)} \geq 0.6 \ \wedge \ \frac{\sum_{s_j \in M}((x_{s_j} > 0)(dd_{s_j} \leq 2))}{\sum_{s_j \in M}(x_{s_j} > 0)} \leq 0.1 \tag{4.21}$$

$$[RHR]: \frac{\sum_{s_i \in M}((x_{s_i} \geq 0)(dd_{s_i} \geq 3))}{\sum_{s_i \in M}(x_{s_i} \geq 0)} \geq 0.6 \ \wedge \ \frac{\sum_{s_j \in M}((x_{s_j} < 0)(dd_{s_j} \leq 2))}{\sum_{s_j \in M}(x_{s_j} < 0)} \leq 0.1 \quad (4.22)$$

4.7 Experimental evaluation

The presented algorithm was evaluated on all 8,848 perimetric examination results of quality levels 4, 3, and 2 from Table 4.1, in a one-against-all scheme. The classification performance was measured by means of *accuracy* (ACC) and *specificity* (SP). Accuracy is defined as $ACC = \frac{TP+TN}{TP+FP+FN+TN}$ and describes the proportion of correctly classified perimetric results [40]. Furthermore, as a high proportion of correctly classified negatives has to be ensured in the context of scotoma type recognition, the performance of the algorithm was also measured in terms of specificity. SP is defined as $SP = \frac{TN}{TN+FP}$ and measures the proportion of correctly classified negatives [40].

The evaluation results of the classification method are presented in Table 4.2. For each scotoma class and the corresponding quality level, the ACC and SP values are reported. In addition, for each scotoma class and quality level, the number of perimetric examination results is presented. Furthermore, weighted average values for ACC and SP are shown per defect type, as well as for the entire data set.

The overall classification accuracy and specificity of the presented rule-based classification method were 83% and 85%, respectively. For examination results of quality level 4, the average (weighted) accuracy and specificity values were 92% and 98%, respectively. Considering the three defect classes with the largest number of instances, namely *normal visual field*, *glaucoma*, and *hemianopic defect*, the algorithm shows very good performance, i.e., ACC and SP values of above 90%.

With decreasing data quality (from examination results of quality level 4 to examination results of quality level 2), which corresponds to increasing uncertainty in classification by the ophthalmologists, we found that the performance of our algorithm also decreases, see Table 4.2. For examination results of quality levels 3 and 2, there was a decrease in the average ACC and SP values to 87% and 85% (for quality level 3) and 79% and 78% (for quality level 2), respectively. This effect could be observed for each scotoma class. The main reason for this effect is the high diversity of manifestations of a scotoma type, which may lead to uncertainty in the classification result by the physician or a miss-classification by the algorithm.

	Weighted avg.		**Quality 4**			**Quality 3**			**Quality 2**		
Visual field defect class	**ACC (%)**	**SP (%)**	**#**	**ACC (%)**	**SP (%)**	**#**	**ACC (%)**	**SP (%)**	**#**	**ACC (%)**	**SP (%)**
C_1 : Normal visual field	91	97	690	91	98	1,622	91	97	123	90	92
C_2 : Central scotoma	83	82	16	91	91	634	86	85	430	80	78
C_3 : Concentric constriction	88	89	13	97	98	111	89	90	51	84	85
C_4 : Glaucoma	76	78	125	93	95	2,956	77	79	999	74	73
C_5 : Diffuse visual field defects and artifacts	88	88	1	95	95	16	88	88	2	86	86
C_6 : Blind spot enlargement	83	84	9	94	95	268	85	85	153	81	82
C_7 : Sector- or wedge-shaped defect	88	88	0	97	97	19	88	89	8	87	87
C_8 : Hemianopic defect	91	92	105	97	98	315	90	91	202	89	90
Overall	**83**	**85**	959	**92**	**98**	5,941	**87**	**85**	1,968	**79**	**78**

Table 4.2: Evaluation of the rule-based classifier on $8,848$ anonymized perimetric examination results that were provided by the Center for Ophthalmology at the University Eye Hospital Tübingen. The data was hand-labeled by expert ophthalmologists and assigned to a quality level 4, 3 or 2 that represents the expert's certainty for the identification of the visual field defect. $q = 4$ is the highest quality level, i.e., the defect type could clearly be identified. For each data quality level and each visual field defect class, the table presents the number of corresponding perimetric examination results, the classification accuracy (ACC), and specificity (SP). In addition, the weighted average values for ACC and SP are shown per defect class, as well as for the entire data set.

4.7.1 Limitations of the rule-based classification approach

The largest loss in ACC (i.e., from 93% for data of quality level 4 to 74% for data of quality level 2) is found in the recognition of glaucoma. Indeed, the recognition of glaucomatous patterns is considered particularly challenging [102], mainly because of its manifestation in 5 Alhorn-stages, as depicted schematically in Figure 2.6. Two examples of miss-classification of glaucoma are shown in the Figures 4.3(a) and 4.3(b). Figure 4.3(a) has been classified by an expert ophthalmologist as a glaucoma stage II defect, although there are many intact test locations within the manually marked defect clusters. Our algorithm has assigned this perimetric result to the class of diffuse defects, since it fulfills the corresponding rule in Formula 4.16. Here, the decision taken by the ophthalmologist was not primarily based on the perimetric result, but under consideration of further patient-related features, such as the intraocular pressure. Such features, however, are often difficult to quantify and were thus not considered in the rule-based classification method.

Another example for miss-classification of a perimetric result is shown in Figure 4.3(b). This perimetric result has been labeled by an expert ophthalmologist as a glaucoma stage I defect. However, when comparing this perimetric result to the schematic depiction of glaucoma stage I, as defined by the Tübingen Scotoma Classification in Figure 2.6, we notice that the typical glaucomatous clusters (i.e., of arcuate shape) are not present. Again, the decision taken by the expert was based on further patient-related features. The presented algorithm has recognized here an enlargement of the blind spot based on the rule shown in Formula 4.19.

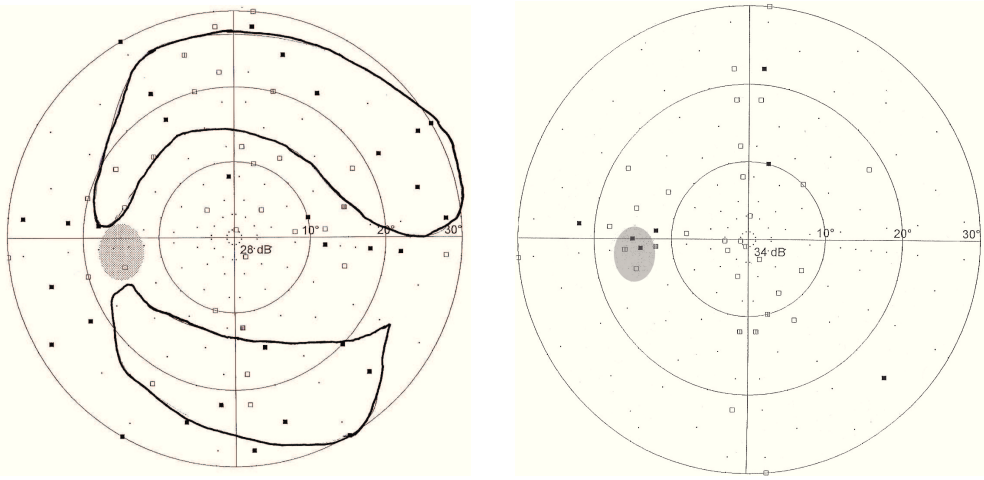

(a) Glaucoma stage II; defect clusters are marked by a physician

(b) Glaucoma stage I

Figure 4.3: Different manifestations of the glaucoma defect class. Defects (failed test locations) are represented by rectangles: Black-filled rectangles represent absolute defects and unfilled rectangles represent relative defects.

In some cases, especially for data of low quality, (e.g., quality level 2) more than one of the presented decision rules might fire. Under the assumption that each perimetric examination result belongs to one and only one defect class, the presented rule iteration order interferes with the classification performance. Figure 4.4(a) presents an examination result that was assigned to the class of central scotoma (C_2), as it fulfills the rule given in Formula 4.14. The ophthalmologists assigned this perimetric result to the class of sector-shaped defect (C_7), although with high uncertainty. As the rule for C_2 is checked before the one for C_7, the algorithm miss-classifies the instance, for which the rule for C_7 would have fired as well.

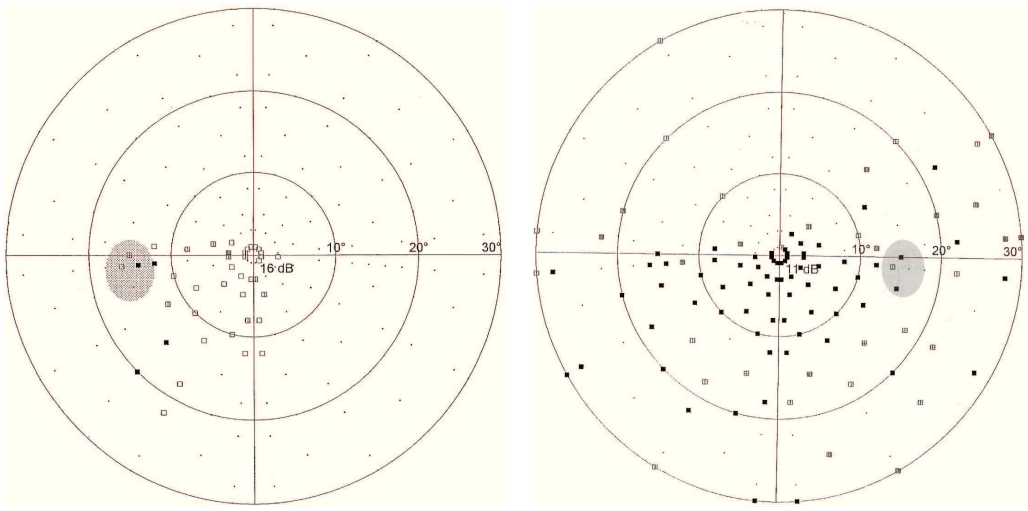

(a) Paracentral scotoma or sector-shaped defect (b) Central scotoma or other defect type

Figure 4.4: Examples of perimetric results of quality level 2.

A last example of a perimetric result of quality level 2 is shown in Figure 4.4(b). According to the rule in Formula 4.12, this perimetric result was classified by the algorithm as a central visual field defect. This assignment is in accordance with the decision taken by the ophthalmologists, despite the fact that a huge defect cluster expanding over the lower half of the visual field is found. However, as all clusters are computed by the presented SOM approach, this defect cluster might be further leveraged, for example in the context of a driving assistance system, which would not only consider the central defect area, but also other defect clusters found in the perimetric result.

Further improvements of the presented algorithm include: (1) the refinement of the decision rules and the investigation of further features, such as features related to the patient's general health condition, with the focus on the glaucoma defect type, (2) further evaluations of our approach on different perimetric devices, (e.g., Humphrey perimeters), and examination grid types, and (3) the development of a user-friendly interface for individual threshold adaptation.

4.7.2 Evaluation results in the context of related approaches

Unfortunately, since we did not have access to the algorithms presented in Section 4.1 or the data that was used for their evaluations, we can only refer to the reported classification results.

Most of the related approaches have focused on a small subset of scotoma classes and especially on the recognition of glaucomatous patterns or glaucoma progression. In our approach, the classification accuracy regarding the detection of glaucoma varied from 74% (for data of quality level 2) to 93% (for data of quality level 4), see Table 4.2. The overall weighted average accuracy for glaucoma recognition was 76%, which is well in line with other approaches [15, 21, 45, 46, 47, 48, 54, 97]. However, note that these approaches were evaluated on relatively small data sets consisting of a few hundred perimetric examination results, whereas our algorithm was evaluated on 4,080 perimetric results of glaucomatous visual field defect cases.

An approach that has considered a larger subset of visual field defect classes was presented by Keating et al. [69], where a back-propagation neural network was used for the classification of visual field data. The achieved accuracy reported there varied from 74% to 96% on simulated perimetric results of the following defect types: (1) central visual field defects, (2) concentric constriction, and (3) hemianopic defects. Our algorithm outperforms this approach for all the mentioned defect types and all data quality levels. For the class of central scotoma (C_2), the classification accuracy achieved by our rule-based classifier varies from 91% (for quality level 4) to 80% (for quality level 2), see Table 4.2. For the visual field defect class of concentric constriction (C_3), the accuracy of our classifier varied from 97% (for quality level 4) to 84% (for quality level 2), whereas for hemianopic visual field defects (C_8), the classification accuracy varied from 97% (for quality level 4) to 89% (for quality level 2), see Table 4.2.

In comparison to the classification accuracy of 80% that was achieved by Fink [39], where a Hopfield-attractor network was used to recognize the visual field defect classes, our algorithm performs better when considering the overall accuracy on data of quality levels 4 and 3. For data of quality level 2, our approach yields similar accuracy results as the approach of [39].

In comparison to the approach presented by Jürgens et al. [64], our algorithm shows similar performance on data of quality level 4, where about 1,000 perimetric results were classified.

In summary, the main advantage of our rule-based scotoma classifier is the integration of expert knowledge into the automated classification method. In contrast to approaches based on neural-networks, the rules can be easily adapted and new features can be included. It is important to note that it is unclear how the above approaches would have performed on data sets of varying quality levels.

4.8 Conclusion

The rule-based scotoma classifier presented in this chapter can be used for the automated analysis of perimetric or campimetric results regarding location, size, and type of the visual field defect. Like the Tübingen Mobile Campimeter (TMC), the scotoma classifier is integrated into the Visual Search Examination Tool (Vishnoo). As the scotoma classifier is decoupled from the perimetric hardware and can be run on any common computer, it can be used beyond the mobile context, such as in local diagnostic processes, e.g., assisting the clinical routine and tele-medicine.

In the automotive context, the TMC and the scotoma classifier can be used by a trained engineer as a screening device to calibrate a camera-based driving assistance system to mitigate the impact of the individual visual field deficits on driving. With the knowledge on impaired areas of the visual field, such a system would track the driver's gaze with the goal to recognize objects that could be overlooked and, in case of an upcoming hazard, warn the driver in advance. An algorithm that lays the foundation for this vision will be presented in the next chapter.

5 Online classification of eye-tracking data

Although we are mostly unaware of it, during visual perception our eyes are constantly moving. As introduced previously in Section 2.3, eye movements enable the retinal part of sharpest vision (i.e., the fovea) to fixate different parts of the scene by involving six types of eye movements [82], among which fixations, saccades, and smooth pursuits are the most studied (see Section 2.3). During a fixation, the eye is kept relatively stable on an area of interest (AOI), whereas saccades correspond to rapid eye movements enabling the fovea to fixate different areas of the scene [115]. Smooth pursuits occur whenever the eye follows a moving target [32]. Thus, the process of looking at a scene can be described as a sequence of fixations, saccades, and smooth pursuits.

Research on visual perception has largely benefited from the development of eye-tracking devices. Accurate methods for quantifying eye movements, e.g., state-of-the-art eye trackers, allow the recording of eye movements at high sampling rates, thus enabling a detailed analysis of visual behavior. Performing such an analysis in an online fashion to detect fixations, saccades, and smooth pursuits in a driver's visual behavior is the main subject of this chapter. The reliable detection and distinction between the above types of eye movements in an online fashion is a crucial step towards the automated identification of objects that might be overlooked by the driver, i.e., potential traffic hazards. While performing such a detection on eye-tracking data in alignment with information from the visual scene is reliably feasible by us humans, reliable automated clustering of eye movements is still challenging; even more so, when the visual scene changes in an online fashion, such as in driving scenarios.

In this chapter, an online, adaptive algorithm for the reliable detection of the above types of eye movements will be presented. Related work on the classification of eye movement data will be discussed in Section 5.1. An overview of our method will be presented in Section 5.2. Our classification method is a two-step approach, where in the first step, saccades are separated from other types of eye movements based on a Bayesian online mixture model, and in a second step, fixation clusters are separated from smooth pursuits based on Principal Component Analysis. The Bayesian online mixture model will be in the scope of Section 5.3. Section 5.4 will present the detection of smooth pursuits based on Principal Component Analysis. Results from experimental evaluations of the proposed algorithms will be presented in Section 5.5, and Section 5.6 will conclude this chapter.

5.1 State of the art methods

Since the first work on classification of eye movements [90, 164], several approaches have been proposed that fall into three main categories: (i) dispersion-based methods, (ii) velocity- and acceleration-based methods, and (iii) probabilistic methods based on statistical Markov models. All groups of algorithms will be briefly discussed in the following subsections. A detailed review can be found in [56].

5.1.1 Dispersion-based methods

Dispersion-based algorithms distinguish between different types of eye movements (mostly between fixations and saccades) based on the distance between subsequent eye position points. Usually, dispersion-based algorithms aim at detecting fixation clusters by identifying data points that are close to each other within a predefined time window, whereas all other data points are not considered [56]. A method that is representative of this group, is the *Dispersion Threshold Identification (I-DT)* algorithm [125], where the separation of fixation clusters from saccades is based on the dispersion of consecutive data points within a temporal window. In I-DT, the dispersion D is defined as the sum of the maximum and minimum differences between the x and y coordinates of the points within the temporal window, i.e., $D = [max(x) - min(x)] + [max(y) - min(y)]$. If D is below a predefined threshold, the data points within the window belong to a fixation. Otherwise, a saccade is found. Similar approaches that use a temporal threshold as in I-DT, but differ in the way the dispersion is calculated have also been presented in [14, 56, 125, 137].

Another prominent algorithm from this group is the *Identification of eye movements based on Minimum Spanning Trees (I-MST)* [56, 125]. As presented in [125], this algorithm first builds a minimum spanning tree (MST) on a predefined number of eye position points that fall within a temporal window. Then, from each node v of the MST, all other MST nodes are visited in depth-first search up to a predefined depth threshold. The mean and the variance of the length of the edges that were visited during the depth-first search are assigned as meta information to v. Based on the meta information of the end nodes of an edge, a decision can be taken concerning the type of eye movement it represents, i.e., a saccade or fixation [125].

Other dispersion-based approaches are based on clustering algorithms. For example, in [127] a mean shift clustering algorithm for the detection of fixation clusters was used. In another approach [162], fixation clusters have been detected based on projection clustering. Typical clustering algorithms, such as the well-known and widely used k-means algorithm, are only applicable to the problem of identifying fixations clusters, when the number of fixation clusters is known a priori. Hence, such algorithms cannot be applied to the analysis of eye movements when viewing dynamic scenes, e.g., such as those occurring while driving, where the number of resulting clusters is not known.

Other approaches in this realm have divided the viewing area into a regular grid and

recorded the time spent inside each square [125]. While such approaches are well-suited for static scenes, e.g., reading a page, they are not applicable to dynamic scenarios, where no a priori information about the viewing area is given. The same holds for techniques that provide visualizations of the areas of interest, i.e., fixation clusters, by adapting the original image [167].

Over the last years, dispersion-based approaches have been implemented in both academic and commercial tools [56], e.g., faceLab [134], SMI BeGaze [135], Gazetracker [37], etc. Although they offer several useful features, their main drawback is that they come as black-box solutions and can hardly be integrated in self-designed applications. Moreover, in most cases, commercial analysis software provides only offline analysis of eye movements. Academic tools such as the MATLAB-toolbox GazeAlyze [9] based on ILab [44] or ASTEF [25] can be easily integrated in self-designed applications but, unfortunately, only for the offline analysis. Another major drawback of dispersion-based methods is that they often rely on thresholds (e.g., length of the temporal window, dispersion threshold, etc.) that have to be empirically adjusted to the individual viewing behavior, the viewing area, and the specific task, thus being inadequate for the task of adaptive, online scanpath analysis [56].

5.1.2 Velocity- and acceleration-based methods

Velocity- and acceleration-based algorithms distinguish between different types of eye movements based on velocities or accelerations between subsequent eye data points [56]. An approach that is representative of this group is the *Velocity-Threshold Identification (I-VT)* algorithm. In I-VT, a point is identified as a saccade point, if the implicit velocity along the distance from the previous data point to that point exceeds a predefined threshold (e.g., $>$ 300 deg/sec). Otherwise the data point is assigned to a fixation cluster [125]. Approaches based on acceleration thresholds work similarly. Due to their simplicity, algorithms of this group have been implemented in several commercial software packages, e.g., Tobii [159], SMI [135], EyeLink [141]. Several recommendations for task specific settings of velocity thresholds have also been made [56].

In general, this group of algorithms is best suited for the analysis of eye data tracked at high sampling frequency ($>$ 200 Hz) [56]. However, as with the dispersion-based methods, a major drawback of the I-VT algorithm and methods related to it is that the applied threshold values need to be empirically adjusted to the eye data at hand. For this reason and because of the fact that velocity profiles are strongly physically- and physiologically- dependent, such methods are not reliable, especially when real-time analysis of eye-tracking data is needed. An additional issue concerns the detection of smooth pursuits. Most velocity-based methods have primarily focused on the separation of fixation clusters from saccades without considering smooth pursuits as an additional class. In [58] a velocity-based approach, which classifies fixation and smooth pursuit clusters into a general “intake" category has been presented. Although saccades and fixations could be separated based on threshold values, smooth pursuits could not be

distinguished from fixation clusters. Commercial implementations, such as the Tobii Fixation Algorithms [159] and the EyeLink parser [141], work similarly [56]. Two-step approaches that use two velocity thresholds to first detect saccades and then separate smooth pursuits from fixations, were presented in [38] and [74]. Offline Eigenvector analysis on data points and velocities within a temporal window has been proposed as an approach to distinguish fixations from smooth pursuits in [8]. Although reliable, the static nature of such offline methods makes them inadequate for the application to dynamically changing scenes. In [74], a combination of velocity and dispersion thresholds was used with the I-VT algorithm (coined I-VDT in [74]) to classify saccades, smooth pursuits, and fixations. As above, following a two-step approach, first saccades are separated from the other two types of eye movements based on a velocity threshold; then, a dispersion threshold is used to separate fixations from smooth pursuits [74]. As with all the presented threshold-based methods, the thresholds of I-VDT have to be chosen carefully, based on thorough data analysis and the specific task.

In summary, most of the dispersion- and velocity-based approaches are based on a considerable number of input parameters that can have significant influence on the classification result. Although several recommendations regarding thresholds for specific tasks have been made, they mostly consider eye-tracking data from viewing behavior on static images.

5.1.3 Probabilistic methods

The most prominent methods that are representative of this realm are Hidden Markov Models (HMM). Such models are simple dynamic Bayesian networks with variables representing values from a discrete state and observation space. Because of their sequential nature, such models are a popular choice for the analysis of successively arising data points (i.e., observations). For the detection of fixations and saccades from eye data, HMMs have been used with velocity observations between successive data points, thus allowing the adaptation of the model to the physiological viewing behavior [125]. In the model of [125] (coined I-HMM), the two states used represent velocity distributions over fixations and saccades. Transition probabilities between the states represent the probability of the next sample belonging to a fixation cluster or a saccade, given the current state [56]. Due to the probabilistic representation of velocities (i.e., no thresholds are needed), the I-HMM is reported to perform better than fixed-threshold methods, such as I-VT [125]. The dynamic and probabilistic nature of HMMs makes them an adequate choice for sequential data arising in an online fashion and containing variability in its features.

Another similar probabilistic approach was presented in [73, 128] and was based on a Kalman-Filter that models and predicts the velocity of eye movements based on previous eye data points. The proposed model could distinguish saccades from fixations.

In summary, with respect to their application to the online analysis of eye data generated in

the context of driving, many of the related approaches reviewed in this section suffer from one or more of the following problems: (i) they require several static input parameters, which makes them inadequate for online usage, (ii) they do not adapt to changing scene information or to the subject's viewing behavior, or (iii) they do not successfully generalize to the detection of smooth pursuits in addition to fixations and saccades [74].

In contrast, our method, which can be assigned to the family of probabilistic models, performs reliably on the task of online classification of fixations, saccades, and smooth pursuits (see Section 5.5.1).

5.2 Method overview

The method for classifying eye-tracking data consists of two steps: In the first step, a Bayesian online mixture model is employed to distinguish saccades from data points that might represent fixations and smooth pursuits. In a second step, a fine-grained Principal Component Analysis (PCA) is conducted to distinguish fixations from smooth pursuits. Both steps are presented in the following sections.

5.3 Bayesian mixture model for the online recognition of fixations and saccades

5.3.1 Theoretical background

Imagine a temporally ordered sequence of two-dimensional data points, $\mathbf{S} = \{s_i \mid 1 \leq i \leq T\}$, e.g., recorded by an eye tracker and representing the visual scanpath of an observer over time. In such a representation, a dense region of successive points (i.e., successive points that are close to each-other in terms of the Euclidean distance) might reflect an AOI (or, more specifically, an object that attracts the observer's attention). According to [103], a fixation location is manifested in eye-tracking recordings as a cloud of points that are normally distributed around the center of the object of interest. Assuming such a normal distribution of fixation points, one could leverage the covariances derived from the coordinates of the data points to approximate the Gaussian distribution that governs them. However, when the number of observation points is rather moderate, such an approximation typically leads to a poor estimation of the underlying distribution. Hence, the proposed algorithm makes use of the intuition that the distances between successive fixation points in an AOI and the distances between successive saccade points come from two distinct Gaussian distributions; thus, following the idea that the structure of two-dimensional data points can be implicitly understood by looking at the distances between them. The resulting (reduced) dimensionality allows the algorithm to effectively deal with a moderate number of observations. The parameters of the two Gaussian distributions (i.e., means and variances) that govern the two different types of distances are learned through a generative mixture model. The Bayesian network in Figure 5.1 depicts

the mixture model for the two Gaussian distributions.

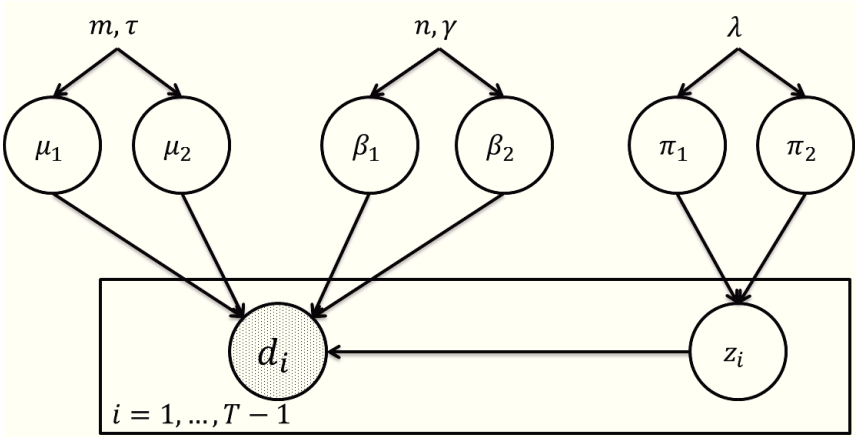

Figure 5.1: Bayesian mixture model for the online detection of fixation clusters and saccades. d_i is a continuous variable representing the distance between the eye data points i and $i+1$, the binary variable z_i represents the choice of either the first or the second Gaussian distribution to generate the ith observation. The rectangle surrounding the variables d_i and z_i is a commonly used, so-called plate notation denoting multiple occurrences of d_i and z_i ($T-1$ in this case). π_1 and π_2 are variables for the prior probabilities for the first and second Gaussian distribution, respectively. The parameter variables (i.e., mean and precision) for each Gaussian distribution are represented by μ_1, β_1 and μ_2, β_2. For the online version of the model, m and τ are parameters of prior distributions that generate the means of the Gaussian distributions. Similarly, n and γ are parameters of prior distributions that generate the precisions of the two Gaussian distributions. λ is the parameter of a prior distribution generating π_1 and π_2.

Let $\mathbf{D} = \{d_i \mid 1 \leq i \leq T-1\}$ be the set of distance variables between points $s_i, s_{i+1} \in \mathbf{S}$. $\boldsymbol{\Theta} = \{\mu_1, \beta_1, \mu_2, \beta_2 \pi_1, \pi_2\}$ denotes the complete parameter set of the mixture model that is depicted in Figure 5.1. The mixture component is denoted by the variable z_i and the observed distances by the observed variables d_i. The simplifying assumption here is that the distances are generated sequentially in an independent and identically distributed fashion. More specifically, each distance between two successive points is generated independently by the most likely Gaussian distribution.

The joint probability distribution of the model is given by:

$$\begin{aligned} p(\mathbf{D}, \mathbf{z} | \boldsymbol{\Theta}) &= \prod_{i=1}^{T-1} p(z_i | \boldsymbol{\pi}) p(d_i | \mu_{z_i}, \beta_{z_i}) \\ &= \prod_{i=1}^{T-1} \pi_{z_i} N(d_i; \mu_{z_i}, \beta_{z_i}) \end{aligned}$$

where $\mathbf{z} = \{z_1, \ldots, z_{T-1}\}$, with $z_i \in \{1, 2\}$ being the index of the mixture component chosen for distance d_i, and $\boldsymbol{\pi} = \{\pi_1, \pi_2\}$ denotes the set of mixture parameters.

We have used Infer.NET [93] to specify the model with the following distributions.

(1) The factorized distribution over the probabilities of each mixture component:

$$p(\mathbf{z}|\boldsymbol{\pi}) = \prod_{i-1}^{T-1} \pi_{z_i}$$

(2) The factorized prior distribution over the model parameters:

$$p(\boldsymbol{\Theta}) = p(\boldsymbol{\pi})p(\boldsymbol{\mu})p(\boldsymbol{\beta})$$

Furthermore, for the online version of the model, the following definitions are needed.

(3) The prior distribution generating the π_1 and π_2 (i.e., the mixture parts) is defined as a symmetric Dirichlet distribution:

$$p(\boldsymbol{\pi}) = Dir(\boldsymbol{\pi};\lambda) \tag{5.1}$$

Note that the Dirichlet distribution is the so-called conjugate prior of the Multinomial distribution governing π_1 and π_2. This means that the posterior distribution on $\boldsymbol{\pi}$ has a similar mathematical form as the Dirichlet distribution, allowing the Dirichlet prior to be updated by the posterior distribution as more observations are made [12]. Similar reasoning holds for the following definitions.

(4) The prior distribution over the means as a product of Gaussians:

$$p(\boldsymbol{\mu}) = N(\mu_1;m,\tau)N(\mu_2;m,\tau) \tag{5.2}$$

(5) The prior distribution over the precisions as a product of Gammas:

$$p(\boldsymbol{\beta}) = Gam(\beta_1;n,\gamma)Gam(\beta_2;n,\gamma) \tag{5.3}$$

Figure 5.2 represents the Gaussian distributions for fixation clusters and sccades, learned by the above model on a real-world data set.

5.3.2 The online model

The above Bayesian model comes with the great benefit that it can be easily turned into an online learning model. In general, for given model parameters $\boldsymbol{\Theta}$ and observations $\mathbf{D}$, after applying Bayes' rule follows that the probability of the parameters $\boldsymbol{\Theta}$ in light of the data $\mathbf{D}$ is:

$$p(\boldsymbol{\Theta}|\mathbf{D}) = \frac{p(\mathbf{D}|\boldsymbol{\Theta})p(\boldsymbol{\Theta})}{p(\mathbf{D})}$$

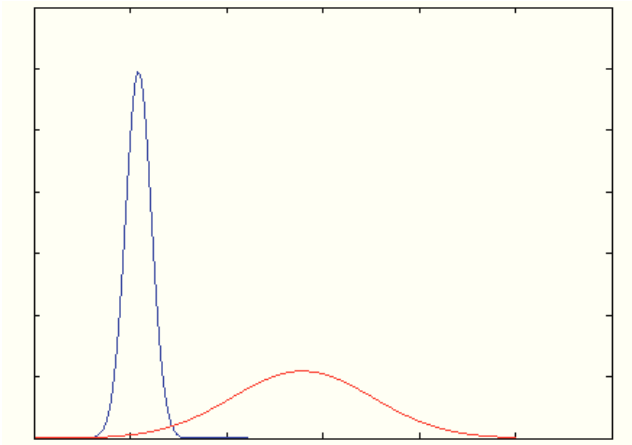

Figure 5.2: Two Gaussian distributions learned by the Bayesian mixture model. The left distribution represents distances between successive eye-tracking points that belong to fixation clusters, and the right distribution reflects distances between successive saccadic data points.

More generally, we can write:

$$p(\mathbf{\Theta}|\mathbf{D}) \propto p(\mathbf{D}|\mathbf{\Theta})p(\mathbf{\Theta})$$

The above formula suggests that in an online setting the prior of the parameters $p(\mathbf{\Theta})$ can be iteratively substituted with the posterior $p(\mathbf{\Theta}|\mathbf{D})$, while the likelihood on the parameters $p(\mathbf{D}|\mathbf{\Theta})$ helps readjust the model, as more and more observations are made (see also [12]).

The above formulation allows the model to readjust the learned parameters $\boldsymbol{\mu}, \boldsymbol{\beta}, \boldsymbol{\pi}$ as more and more eye movement data is available. To this end, we use Gaussian distributions as conjugate priors for the means μ_1, μ_2 (see Equation 5.2), Gamma distributions as conjugate priors for the precisions β_1, β_2 (see Equation 5.3), and Dirichlet distributions as conjugate priors for π_1, π_2 (see Equation 5.1). All these distributions belong to the so-called exponential family of distributions, meaning that they have the same abstract mathematical form. This allows the above prior distributions to be iteratively updated by the posterior distributions on the corresponding variables of the model as new data points are observed. The whole model was implemented in C# and Infer.NET. Also, for the probabilistic inference on the model, we have used Variational Message Passing as implemented by Infer.NET.

5.3.3 Demonstration of functionality on exemplary, real-world driving situations

To showcase the functionality of the above algorithm, we used eye-tracking data, collected from on-road driving sessions with different subjects. The study will be presented in detail in Chapter 6. The fragment of the data that we have chosen for the following demonstration represents three exemplary situations from the driving sessions of two

different subjects. The eye movements of the subjects were recorded by a Dikablis [35] infrared eye tracker, at a sampling rate of 25 Hz. The scene is captured at an image resolution of 768×576 px. After a three-point calibration routine, the gaze and scene information is synchronized online.

The raw eye-tracking data was used as input for the online Bayesian mixture model. The aim was to identify AOIs (i.e., perceived traffic objects) of the driver. As the detection of AOIs was performed online, and the gaze points were processed sequentially, the information used by the algorithm consisted only of the coordinates of the gaze points in the scene image. Data points with coordinates $x = 0, y = 0$ were excluded from processing as they were either related to blinks or missing pupil position (e.g., due to unsuccessful pupil detection by the eye-tracking system).

Figures 5.3, 5.4, and 5.5 depict representative frames from longer video sequences. More specifically, for each driving situation (depicted in each figure), multiple subsequent frames were used to detect the fixations and saccades. In order to avoid an overload of scene images, the detected, subsequent fixation clusters (depicted in Figure 5.3 and Figure 5.4) or saccade points (in Figure 5.5) are presented in separate images above or below the scene. Different colors stand for different fixation clusters. Dotted lines connect the detected clusters with the corresponding objects or traffic participants that were fixated by the subject in the sequences. The single red points in Figure 5.5 represent sequential saccade points. The chronological viewing order of the entities in the scene is denoted by time stamps t_i.

The first 200 gaze points (corresponding to 8 seconds) at the beginning of each driving session were used by the model to learn the individual viewing behavior of the subject. This allows the algorithm to adapt to the viewing behavior of the corresponding subject. All the remaining gaze points were processed in an online fashion, allowing the algorithm to update the parameters according to changes in the scene or viewing behavior, as described in Section 5.3.2. It is important to note that, depending on the driving speed, the scene information can change very quickly. At high speed, objects and traffic participants appear within the driver's visual field for a very short time. Furthermore, for every new entity appearing on the scene, when the entity is fixated by the subject, the algorithm needs to recognize a new cluster in an online fashion. This means (1) that small subsequent fixation clusters (corresponding to different objects) have to be separated and (2) that the number of possible clusters is not known beforehand. In consequence, clustering algorithms that require a fixed number of clusters beforehand or algorithms that detect fixation clusters and saccades based on thresholds (e.g., on velocity, dispersion, etc.) are not suitable for these scenarios.

As depicted in Figures 5.3, 5.4, and 5.5, the viewing behavior during driving is characterized by brief fixations. Hence, the algorithm has to efficiently make sense of very few new gaze points and quickly decide whether they correspond to a fixation cluster or to saccades. In all the scenarios depicted in this section, the algorithm dealt with the

incoming data in real time. We hypothesize that the performance would be unchanged, even if the gaze points were sampled at a much higher eye-tracking rate. Furthermore, although the raw data is noisy and the viewing behavior is subject-dependent, the proposed algorithm adapts very quickly to the individual viewing characteristics of each subject and performs robustly in detecting the AOIs in an online fashion.

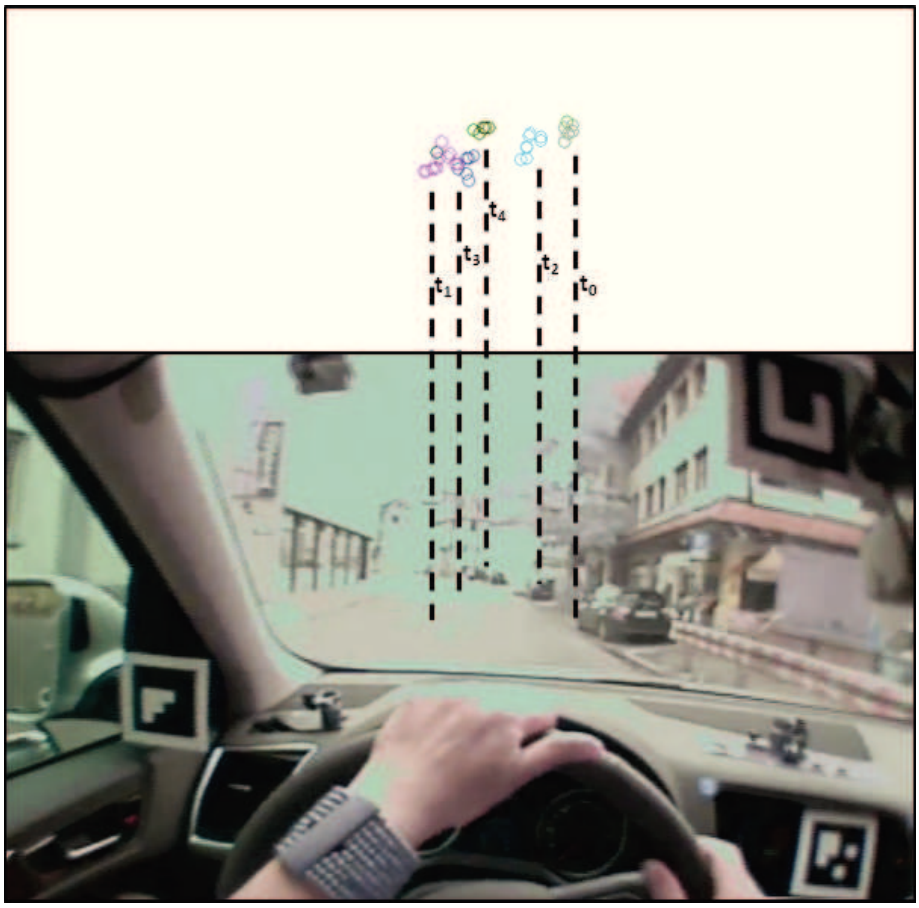

Figure 5.3: Areas of interest (AOIs) for a driving sequence of 1.76 sec length (subject 1). During this driving sequence (corresponding to 44 frames) the model detects 5 fixation clusters time-stamped according to their chronological order $t_0 \ldots t_4$. At the beginning of this sequence the subject was fixating the first car on the right side of the road (t_0). A few frames later the gaze was directed toward the middle of the road (t_1). The AOI in the actual frame corresponds to the car connected to the cluster at time stamp t_2. Yet a few frames later, the subject fixates again the road (t_3) and finally, in the last frames, a car (t_4) in the rear of the road is fixated.

Overall, the mentioned strengths allow the presented Bayesian mixture model to be applied to independent viewing sequences, containing only few gaze points. This flexibility makes it adequate for broad applications in vision research, where the online analysis of gaze-based interaction (e.g., tracking a subject's attention or detecting overlooked entities) is crucial.

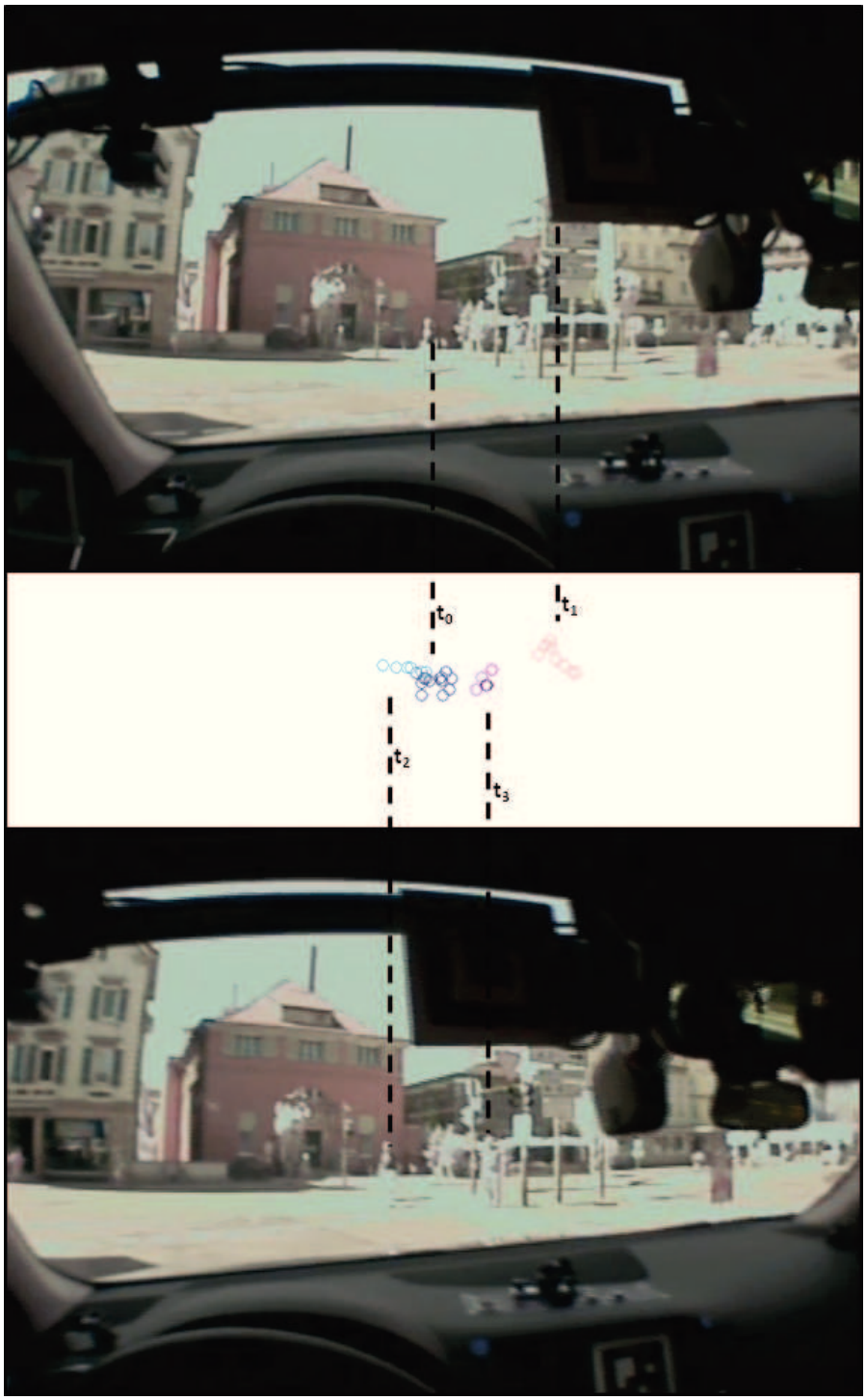

Figure 5.4: AOIs in a road junction scene (subject 2). The four clusters (or AOIs) detected here correspond to the entities fixated during a driving sequence of 1.2 seconds. The frame on the top presents the scene at the beginning of this sequence. First the subject fixates the person crossing the street (time-stamped by t_0). After that, the gaze of the subject is directed towards the traffic sign on the right side (t_1). The lower frame corresponds to a scene image captured about 700 ms later. At this point in time, the subject fixates again the person crossing the street (t_2) and moves later his gaze towards another person crossing the street (t_3).

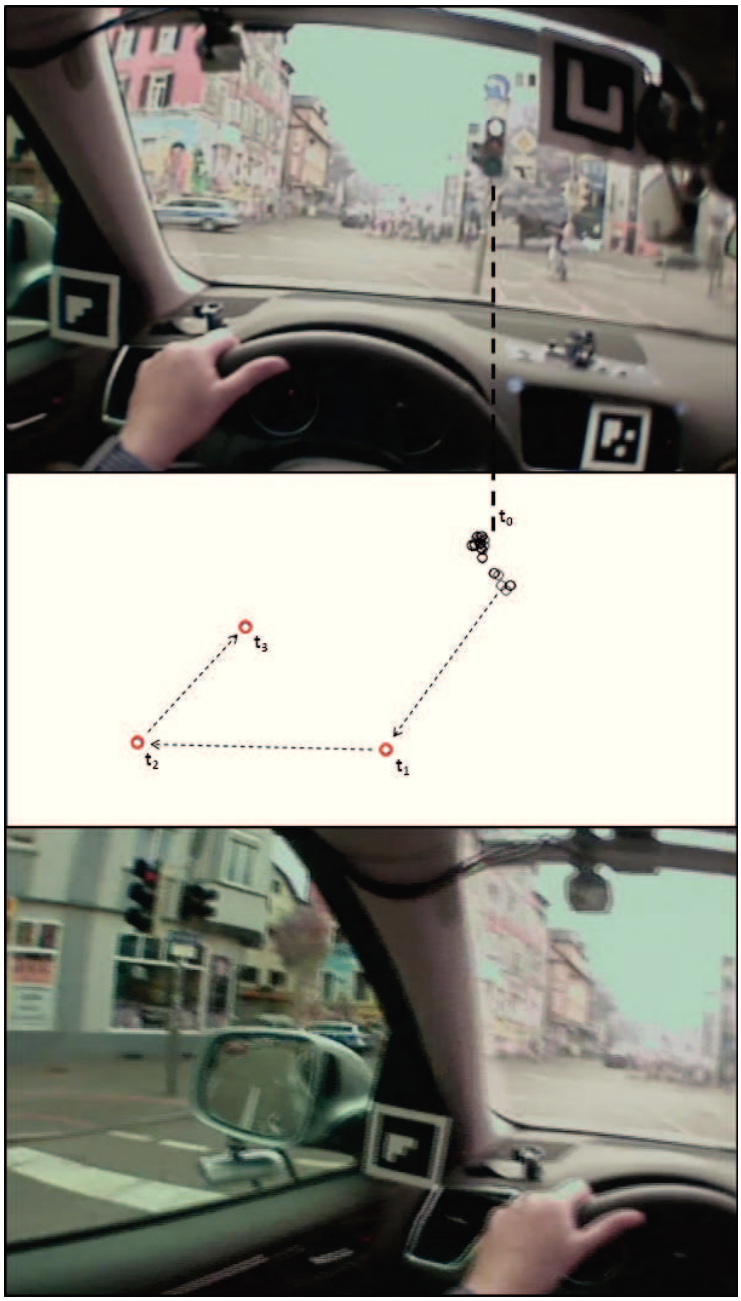

Figure 5.5: Fixation cluster and saccade points at a traffic light (subject 1). The single cluster detected in this sequence corresponds to the traffic light fixated by the subject (see frame on top) in the beginning of the sequence (time-stamped by t_0). A few frames later, the subject's gaze is directed towards the traffic light on the left side of the road (see lower frame). This happens over three saccades (t_1, t_2, t_3), which were detected correctly by the algorithm. It is interesting to see that for the t_0-cluster the algorithm has decided that all gaze points belong to the same cluster, thus indicating that the algorithm has correctly adapted to the subject's viewing behavior.

5.4 Principal Component Analysis for the detection of smooth pursuits

Reliably distinguishing fixations from saccades is an important first step towards automated driving support and the prediction of hazardous situations. However, in driving scenarios, objects are typically in motion relative to the driver. Therefore it is crucial to automatically recognize objects that are being pursued by the driver's gaze and others that are not. To address this issue, we have extended the above method to also recognize smooth pursuits. We first describe the general idea and then the details of the algorithm.

Let us assume that the last k gaze points were labeled by the above mixture model as fixation points. The key question is whether these points are centered around a relatively stable target or correspond to a moving object that is being pursued by the driver's gaze. In the former case, the vector that represents the highest variability in the k data points and the one representing the second highest variability will have approximately similar lengths. In the latter case though, there will be a notable difference in the lengths of the two vectors. Note that these vectors correspond to the first and the second eigenvectors of the covariance matrix of the data points. We rely on Principal Component Analysis [63] to efficiently retrieve these vectors.

More specifically, let $\mathbf{M}$ be the matrix holding the last k successive data points that were all labeled as fixation points, such that each row of $\mathbf{M}$ contains the coordinates of a point after subtracting the (empirical) mean of the distribution of all points. Through singular value decomposition, $\mathbf{M}$ can be decomposed into $\mathbf{U}\mathbf{\Sigma}\mathbf{V}^T$, where $\mathbf{U}$ contains the orthonormal eigenvectors of the covariance matrix $\mathbf{M}\mathbf{M}^T$, $\mathbf{\Sigma}$ is a diagonal matrix containing the positive roots of the eigenvalues of $\mathbf{M}\mathbf{M}^T$, and $\mathbf{V}$ contains the orthonormal eigenvectors of $\mathbf{M}^T\mathbf{M}$. This decomposition is unique up to different orderings of the values in $\mathbf{\Sigma}$. This means that if the values are ordered decreasingly (with the largest value in the upper-left corner of the matrix) in $\mathbf{\Sigma}$, then the first and the second column of $\mathbf{U}$ correspond to the first and second eigenvector of $\mathbf{M}\mathbf{M}^T$, respectively.

In order to decide whether the last k data points describe a smooth pursuit, we compute:

$$\frac{\sigma_2^2 \cdot \|u_2\|}{\sigma_1^2 \cdot \|u_1\|} = \frac{\sigma_2^2}{\sigma_1^2} \leq t$$

where t is an empirically established threshold, σ_1 and σ_2 are the largest and the second largest values in $\mathbf{\Sigma}$, respectively, and u_1 and u_2 are the corresponding eigenvectors.

An example scenario of an online smooth pursuit detection is depicted in Figure 5.6, where a hazardous situation arises from the white car cutting into the lane from the right. The figure shows video frames from a driving scene that was generated in a driving simulator (see Chapter 7). The driver's eye movements were tracked by means of a mobile Dikablis eye tracker at a sampling rate of 25Hz.

Figure 5.6(a) shows the moment when the driver's attention is caught for the first time by the white car. The black arrow shows the shift of visual attention in the most recent time frame of 1s. Figure 5.6(b) depicts the situation 400ms later, when the driver has come closer to the white car. During this time, the driver's gaze has pursued the relative movement of the white car. According to the variability of the gaze points, which were labeled as a fixation cluster by the online Bayesian mixture model, the PCA-based analysis has classified them as belonging to a smooth pursuit.

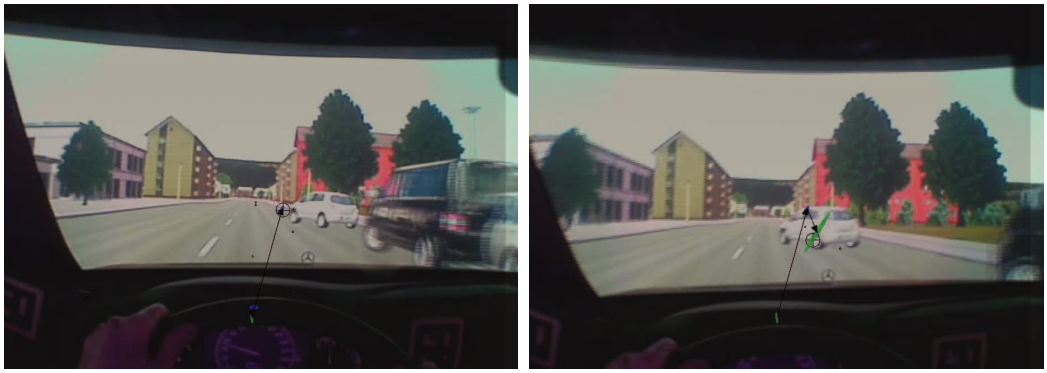

(a) (b)

Figure 5.6: An example scenario of smooth pursuit.

5.5 Experimental evaluation

In this section, we first demonstrate the superior quality of the online Bayesian mixture model over a state-of-the-art model for detecting fixations and saccades and then showcase the quality of the PCA-based detection of fixations, saccades, and smooth pursuits based on a real-world, hand-labeled data set.

5.5.1 Evaluation of the Bayesian mixture model in comparison with a Hidden Markov Model

Competitor For the quality evaluation of the Bayesian Mixture Model (BMM), we compared its prediction performance to that of a Hidden Markov Model (HMM), such as the one presented in [73, 125]. These types of models come with several advantages over threshold-based methods: (1) no fixed thresholds are needed, instead the parameters of the model (i.e., state transition probabilities and label emission probabilities) are learned from labeled data, (2) in consequence, HMMs can adapt to the individual (i.e., physiological) viewing behavior of a subject and to the specific task, and (3) given their dynamic sequential structure, they are naturally suited for sequentially arising data points,

such as eye-tracking data. Note also that both models, HMM and BMM, belong to the family of probabilistic models.

We implemented a two-state HMM according to the description of the I-HMM in [125]. However, the observed sequences for the I-HMM were velocities between the eye-tracking data points, whereas in the HMM version that we have implemented, the sequences consist of distances between successive data points. Based on training (i.e., labeled data points) such distance observations can be mapped to a discrete set of observations, which in our context consist of (1) the mean of distances between saccade points and (2) the mean of distances between fixation points. Note that this is very similar to the BMM, which continuously updates these means in a Bayesian way; thus both models operate on comparable conditions. As with the I-HMM [125], the two states of the HMM represent a distribution over fixations and saccades. Such a distribution as well as the transition probabilities between the states can be learned from labeled data, by computing the corresponding maximum likelihood estimations. A Viterbi-based, forward-backward algorithm [42] was implemented to compute the most probable state sequence of the HMM for a given observation sequence.

Data set In order to learn the above parameters, and to evaluate the performance of the HMM and BMM, two real-world, eye-tracking data sets were employed. Each data set consisted of 750 data points and was analyzed frame-wise by two PhD students. An eye-tracking data point was thereby labeled as belonging to a saccade or fixation only if both of the judges agreed. Blinks and disagreements were excluded from the data. Note that this annotation task is very laborious, as the eye-tracking data has to be labeled manually with respect to the information on the scene.

This annotation process led to the following data sets:

- **Data set I** consisted of 628 eye-tracking data points that were recorded during an on-road driving session (for more details, see Chapter 6). Out of these points 15 were labeled as saccades, and the remaining ones as fixations.

- **Data set II** consisted of 713 eye-tracking data points that were recorded during a driving session in a simulator (for more details, see Chapter 7). This data set contained 67 saccade points and 646 fixation points.

The HMM parameters were trained on random samples of the above data sets, from which the weighted average values of the parameters (transition and state probabilities) were computed. In contrast, the BMM, which updates the learned parameters in an online fashion (i.e., as new data points are observed) was trained on the first 200 data points of each data set. Once the parameters were learned for both models, their prediction quality was tested on each data set.

Evaluation results Table 5.1 gives a summary of the performance of each of the competing models, HMM and BMM, for each data set, and for each class of data points (i.e., saccade, fixation). The performance is summarized in terms of true positives (TP), false positives (FP), true negatives (TN), and false negatives (FN) for each class. Note that in this binary setting, the third and the fourth column (and the fifth and the sixth column) of Table 5.1 are symmetric in the sense that a true positive for the one class is a true negative for the other. The last two rows in the table show the number of positives and negatives contained in each data set.

Method	Outcome type	Data set I		Data set II	
		Saccade	Fixation	Saccade	Fixation
HMM	TP	11	545	34	636
	FP	68	4	10	33
	TN	545	11	636	34
	FN	4	68	33	10
BMM	TP	13	610	67	644
	FP	3	2	2	0
	TN	610	13	644	67
	FN	2	3	0	2
Ground truth	P	15	613	67	646
	N	613	15	646	67

Table 5.1: Comparison of the HMM and the BMM in terms of absolute numbers of TP, FP, TN, and FN for the detection of saccades and fixations based on two hand-labeled data sets.

A detailed analysis of the quality of both algorithms with respect to the detection of saccades and fixations is shown in the Tables 5.2 and 5.3, respectively. Both tables show quality results in terms of the following measures: *Precision* ($\frac{TP}{TP+FP}$), *Recall* ($\frac{TP}{TP+FN}$), *F1-measure* ($\frac{2 \cdot Precision \cdot Recall}{Precision+Recall}$), which represents the harmonic mean of precision and recall, and *Accuracy* ($\frac{TP+TN}{TP+FP+TN+FN}$).

Table 5.2 shows that the BMM clearly outperformed the HMM with respect to the detection of saccades, which, in this context, is the more critical class, since a correct detection of saccades implies a correct separation of fixation clusters. Note that in general the proportion of saccade points is much smaller than that of fixation points, e.g., the proportion of saccades in Data sets I and II was 2.4% and 9.4%, respectively. For a model such as the HMM, which aims at maximizing the joint probability of a sequence of states and corresponding observations, it is safer to focus on the most probable states and observations; these are fixations (97.6% for Data set I and 90.6 % for Data set II) and the corresponding distance means. These findings are also in line with the findings presented in [73].

In contrast, for the detection of saccades, the BMM achieved an astounding precision of 81% and 97% for Data sets I and II, respectively. It also showed higher recall values than

the HMM on this very difficult task for both data sets, i.e., it achieved values of 87% and 98% for Data sets I and II, respectively. This implies that, most of the time, successive fixation clusters are correctly separated by the BMM.

	Model	Precision	Recall	F1-measure	Accuracy
Data set I	**HMM**	0.139	0.733	0.234	0.885
	BMM	0.813	0.867	0.839	0.992
Data set II	**HMM**	0.773	0.507	0.613	0.939
	BMM	0.971	1.0	0.985	0.997

Table 5.2: Quality comparison of the HMM and the BMM for the class of saccade points.

Indeed, a much better performance of the HMM is shown in Table 5.3, where the precision with respect to the detection of fixation points was 99% and 95% for Data sets I and II, respectively. The BMM achieved a similar precision on Data set I and a maximum precision of 1.0 on Data set II. For Data set I, the recall of the HMM with respect to the detection of fixation points is remarkably lower than that of the BMM, because the HMM does not manage to adapt well enough to varying distances between fixation points. This is different for the BMM, which can adapt to varying distances in an online fashion. On Data set II, the recall of both methods is comparable. Despite the improved performance of the HMM on the second data set, it was still notably outperformed by the BMM with respect to all measures.

	Model	Precision	Recall	F1-measure	Accuracy
Data set I	**HMM**	0.993	0.889	0.938	0.885
	BMM	0.997	0.995	0.996	0.992
Data set II	**HMM**	0.951	0.984	0.967	0.939
	BMM	1.0	0.997	0.998	0.997

Table 5.3: Quality comparison of the HMM and the BMM for the class of fixation points.

These results highlight the superior performance of the online Bayesian mixture model in comparison to a Hidden Markov Model. Especially, on the difficult task of reliably detecting saccades, which is crucial for the correct separation of fixation clusters, the Bayesian mixture model achieves highly satisfiable precision, and recall values. In addition, a reliable detection of well-separated fixation clusters is a prerequisite for the reliable performance of the PCA-based classification technique from Section 5.4.

5.5.2 Overall evaluation of the classification technique

The PCA-based extension of the Bayesian mixture model to detect smooth pursuits, in addition to fixations and saccades, was evaluated on Data set II, which was presented in the previous section. To this end, each fixation cluster had to be manually annotated as a smooth pursuit or simple fixation cluster, as presented below.

Data set Overall, there were 47 situations in Data set II that could be clearly assigned (i.e., in agreement by two PhD students) to a fixation or smooth pursuit cluster. 39 of the above situations were labeled as fixations clusters and 8 as smooth pursuit clusters. 67 eye data points were labeled as saccade points. Note that due to the low sampling rate of the eye tracker (i.e., 25 Hz) clusters of saccades were not frequent. Therefore, instead of looking into clusters of saccades, we will look into the absolute number of saccade points that were present in Data set II. Note that the above manual annotation of fixation clusters, saccades, and smooth pursuit clusters is very laborious, since successive frames have to be carefully analyzed in alignment with objects occurring on the scene.

Evaluation results Table 5.4 shows the per-class true-positive and false-positive counts. While our algorithm detected all saccades correctly, it classified two fixation points as saccades. In consequence this lead to the separation of two fixation clusters into four (smaller) fixation clusters. In addition, it classified one fixation cluster as a smooth pursuit cluster, and one smooth pursuit as fixation. It correctly identified 7 out of 8 smooth pursuit clusters and 36 out of 39 fixation clusters. Although preliminary in nature, these results are very promising and we plan to further evaluate the algorithm on larger labeled data sets.

Eye movement type	Annotation	TP	FP
Fixation clusters	39	36	5
Smooth pursuit clusters	8	7	1
Saccade points	67	67	2

Table 5.4: True and false positive counts for the detection of fixation clusters, smooth pursuit clusters, and saccade points.

5.6 Conclusion

We have presented an adaptive online algorithm for clustering eye movement data. The experimental evaluation on raw eye-tracking data, collected from on-road and simulated driving sessions with different participants has demonstrated the reliable performance of the proposed algorithm. Its superior prediction quality was shown in comparison with a state-of-the-art Hidden Markov Model. Its demonstrated ability to reliably detect smooth pursuits, in addition to fixation clusters and saccades is a remarkable feature that distinguishes the proposed algorithm from many state-of-the-art algorithms, which mainly focus on fixations and saccades. In this sense, the proposed algorithm is a highly advanced method for the online analysis of scanpaths in driving scenarios. Its real-time application and its adaption to the driver's viewing behavior is enabled by the underlying online Bayesian mixture model, which continuously adapts its parameters in light of new data. This is also witnessed by the two studies presented in Chapters 6 and 7, where the proposed algorithm is used for the real-time scanpath analysis. An important question of future research concerns the applicability of the proposed method to the real-time analysis of eye-tracking data sampled at high frequency, e.g., above 200 Hz.

6 Analyzing driving and viewing behavior of subjects with visual field defects in an on-road study

As mentioned in Section 2.4, subjects suffering from binocular visual field defects, such as glaucoma or HVFDs, are often prohibited from driving. In the same section, an important consensus stemming from several scientific studies on the driving performance of subjects with binocular visual field defects was highlighted; namely, that people with an effective visual exploration capability are able to compensate the defect of the visual field.

In order to assess the driving performance and identify gaze-related parameters that correlate with it, we conducted an on-road study with patients with binocular visual field defects and healthy-sighted subjects. A dual-brake vehicle was used. Eye movements were captured by means of a mobile eye tracker. In addition, the behavior of the driver and the driving scene were recorded. In order to analyze the visual exploration of the subjects, all previously introduced methods were employed. Therefore, this study can be seen as a feasibility study for the integrated application of the methods that have been presented throughout this thesis.

The information about the impaired areas of the visual field was extracted using the scotoma classifier that was presented in Chapter 4. The raw eye-tracking data was analyzed using the classification algorithm that was presented in Chapter 5.

After an introduction of the methodology that has been used in this study in Section 6.1, the results regarding the driving performance of the subjects and their viewing behavior will be presented in Section 6.2. Section 6.3 will discuss our findings, before concluding in Section 6.4.

6.1 Study materials, setting, and methods

6.1.1 Participants

Ten HVFD patients (we refer to this group as HP for short), ten glaucoma patients (GP for short), and 20 healthy-sighted, age- and gender-matched control subjects (C for short) participated in the study. In the group HP, four patients had a right-sided defect (HR), whereas six had left-sided HVFDs (HL). All patients and control subjects were recruited by the Department of Neuro-Ophthalmology at the University of Tübingen.

To be included in the study, all participants were required to be at least 18 years old. They had to undergo medical examinations (e.g., visual function testing, examination of health condition, etc.) and several cognitive tests. Since our focus was on persistent visual field defects and a spontaneous improvement six months after a lesion onset is rather improbable, a requirement for the HP group was that the lesion onset occurred at least six months ago. Short interviews reveled that many patients from the HP group had quited or reduced driving to a minimum shortly after the incident that had lead to the visual field defect (e.g., stroke, accident, etc.). A requirement for each patient in the GP group was the presence of an open angle glaucoma with advanced binocular visual field defect (stages II-IV according to the Aulhorn classification [5]). Interviews with patients from the GP group revealed that only few of them had reduced driving.

The research study was approved by the Institutional Review Board of the University of Tübingen (Germany) and was performed according to the Declaration of Helsinki. Following verbal and written explanation of the experimental protocol, all subjects gave their written consent, with the option of withdrawing from the study at any time.

6.1.2 Vehicle and route

The on-road driving performance of the subjects was assessed under in-traffic conditions using an Audi Q5 SUV, provided by the Research Center for Computer Science (FZI) in Karlsruhe. The vehicle was equipped with a dual brake and two scene cameras, see Figure 6.1. The first camera was directed to the road to record the forward driving scene, marked by (b) in Figure 6.1. The second camera was pointing towards the driver to record the driver's behavior, marked by (c) in Figure 6.1. A certified driving instructor, who was aware of the medical status of the participants, sat in the front passenger seat and was responsible for monitoring driving safety. A driving instructor in the role of a driving examiner, who was unaware of the participants' medical characteristics, sat in the right back seat and evaluated the driving performance.

The driving route was designed to meet the requirements of the German driving test procedure. The overall length of the course was 20 km including a variety of scenarios, such as urban traffic, motorway, passages through residential areas, backing into a parking space, etc. Depending on the daytime and the traffic volume, the driving test lasted between 30 to 40 minutes. Prior to the on-road assessment, the participants were introduced to the vehicle and its usage by the driving instructor.

Eight representative driving scenes covering a wide range of traffic situations were selected for detailed analysis of the driving and visual search behavior. The chosen route sections with their particular challenges are listed in Table 6.1.

Figure 6.1: A participant wearing (a) a mobile eye-tracking head unit, (b) a camera recording the driving scene, and (c) a camera recording the driver and the car interior during the drive. (d) markers used for the calibration of the eye tracker. (e) marker used in post-processing of the raw eye-tracking data.

Scene	Name	Important factors
1	Urban traffic	Respecting traffic signs, appropriate scanning, gap judgment
2	Merging into floating traffic	Respecting signs, exploration of the scene, scanning, gap judgment
3	Roundabout traffic	Scanning, gap judgment
4	Left turn	Exploration of the scene, gap judgment
5	Motorway	Lane keeping, steering steadiness, following the speed limit
6	Motorway access	Gap judgment, scanning, exploration
7	Motorway	Scanning, lane keeping, steering steadiness, following the speed limit
8	Backing into a parking space	Gap judgment, scanning

Table 6.1: The representative driving scenes that were used for evaluating the driving performance.

6.1.3 Eye tracking

A mobile eye tracker (Dikablis, Ergoneers Inc., Manching, Germany) [35] was used to record the eye movements during the driving task. It consists of two cameras: a field camera directed to the forward scene (marked by (a) in Figure 6.2) and an eye camera directed to the driver's eye in order to record the eye movements (marked by (b) in Figure 6.2). The resolution of the images provided by the eye and field camera was 384×288 pixels and 768×576 pixels, respectively [35]. Eye movements were recorded at a frequency of 25 frames per second.

The equipment was light-weighted and could be worn over the subject's glasses, see Figure 6.2. The head unit of the eye tracker was connected to a small transmitter mounted at the subject's neck. The transmitter was coupled with the head unit and had a wireless connection to the processing unit, which consisted of a receiver and the recording notebook. The subjects reported that they were not hindered by the eye tracker during the on-road driving.

Figure 6.2: Participant wearing a Dikablis eye tracker (Ergoneers Inc., Manching, Germany). (a) field camera, (b) eye camera.

6.1.4 Driving skill parameters

The driving examiner assessed the driving performance (as passed/failed) of the subjects according to the German driving license regulations. For example, in case of an intervention by the driving instructor to avoid an accident, the driving test was rated as failed. Such events were noted down by the driving examiner. Based on this rating, the overall *failure rate*, i.e., the percentage of drivers who failed the test, was calculated.

In addition, according to [165], a detailed analysis of the following driving skill parameters was performed based on recordings of the driver's behavior and of the scene:

Lane keeping refers to the ability to keep the position within the lane.

Speed refers to the ability to drive at an appropriate speed, following the speed limit or to speed adaptation to the traffic conditions.

Gap judgment refers to the ability to keep an appropriate distance in or when entering traffic flow, at intersections, or when passing other cars.

Scanning refers to the ability to scan the traffic scene appropriately (e.g., using mirrors) and to pay attention to traffic signs and other traffic participants.

Head and shoulder movements refers to the ability to perform appropriate visual exploration of the traffic scene.

The driving performance with regard to these parameters was assessed based on a 6-point rating scale from 0 (representing bad performance) to 5 (representing very good performance). Head and shoulder movements were also quantified based on the same 6-point scale (0=not excursive, 5=highly excursive).

6.1.5 Gaze-related parameters

Eye-tracking data was first post-processed by the D-Lab software tool [35]. The extraction of the correct pupil position was perhaps the most laborious task. Due to changing illumination conditions during the drive, the automated detection of the pupil position could not be correctly determined and thus had to be manually annotated on the frames of the recordings. The detection of fixations and saccades from eye-tracking data was then computed using the Bayesian algorithm introduced in Chapter 5 in a simulated real-time processing of eye-tracking data.

In order to quantify the frequency and duration of a subject's gaze towards the visual field defect or towards the peripheral visual field, the defect area of each patient was marked as an Area Of Interest (AOI). The shape and extent of these AOIs was extracted from perimetric measurements using the scotoma classifier that was presented in Chapter 4. The AOIs were imported into D-Lab to analyze the viewing behavior of the patients towards them. The following gaze-related parameters were analyzed:

Horizontal Gaze Activity (HGA) Specifies the standard deviation of the pupil on the x-axis in pixel and was used as an overall measure of eye movements.

Proportion of Glances in Percent (PGP) The proportion of gazes towards a defined AOI during a specific time interval in percent. The PGP was measured for the following AOIs: (i) beyond the 30° area of the visual field, (ii) beyond the 60° area of the visual field, and (iii) towards the area of the visual field defect. These AOIs are illustrated in Figure 6.3.

(a) (b) (c)

Figure 6.3: The proportion of gazes towards three AOIs (transparent blue) was computed: (a) AOI beyond the central 30° visual field (PGP beyond 30°), (b) AOI beyond the 60° visual field (PGP beyond 60°), and (c) AOI of the visual field defect (PGP towards VFD). The PGP towards the AOIs in (a) and (b) was calculated for all participants. For the AOIs in (c), the PGP was calculated only for the groups HP and GP (since control subjects did not have visual field defects).

Horizontal Gaze Distribution (HGD) The HGD describes the PGP in five different AOIs as illustrated in Figure 6.4:

(L2): left outer area ($> 60°$) of the visual field

(L1): left area of the visual field between 60° and 20°

(C): central visual field area between 20° left and 20° right

(R1): right area of the visual field between 20° and 60°

(R2): right outer area of the visual field ($> 60°$)

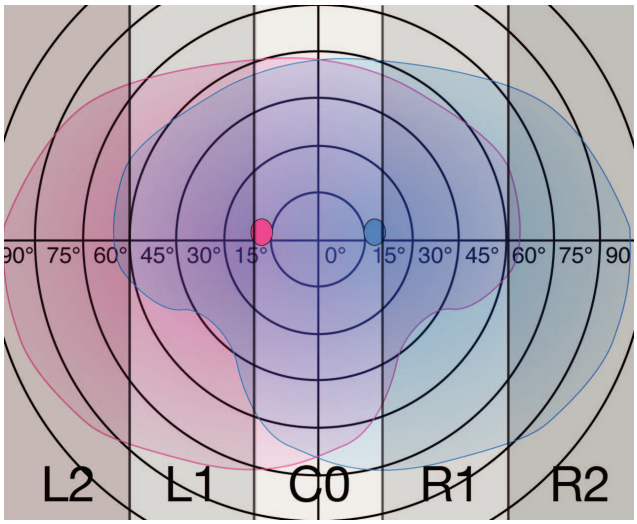

Figure 6.4: Distribution of the five different AOIs over the visual field for the assessment of HGD.

6.1.6 Statistical analysis

The R tool [119] was used to conduct the statistical analysis of the data. In order to identify driving skills and gaze parameters associated with successful task performance, the above listed parameters were compared across the following participant groups based on a one-way *Analysis of Variance* (ANOVA) test:

- Control subjects who passed the driving test (C_p), patients who passed (P_p) and patients who failed the test (P_f)
- Glaucoma control subjects who passed (GC_p), glaucoma patients who passed (GP_p), and glaucoma patients who failed the test (GP_f)
- HVFD control subjects who passed (HC_p), right-sided HVFD patients who passed (HR_p), left-sided HVFD patients who passed (HL_p) and HVFD patients who failed the test (HP_f)

ANOVA is the most commonly used statistical test for the comparison of means between different groups of measurements. It is based on three assumptions: (1) each measurement is independent of the others, (2) the measurement variable within each group is normally distributed, and (3) the groups are homogeneous in term of variances. In a first step, the mean of the observed data within each group is calculated. Then the variance among these means is compared to the average variance within each group. The null hypothesis is that there is no difference in the mean values of the different groups. This null hypothesis is rejected, if the among-group variance is significantly different from the within-group variance, thus implying that the measurements in the different groups are specific to those groups (i.e., the division into groups is meaningful from a statistical point of view). The test statistics is the ratio of the among-group-variance to the average within-group variance, i.e., the F-statistics [139].

However, since ANOVA does not explicitly reveal between which pairs of means there is a significant difference, the Tukey's HSD (Honestly Significant Difference) test was computed post-hoc. This test compares pairwise the means between groups based on the Studentized range statistic [139]. As multiple comparisons were carried out, the significance level was adjusted using a Bonferroni correction to an alpha-level of 0.05 [139].

6.2 Study results

6.2.1 Failure rate

13 out of 40 (32.5%) participants failed the driving assessment: 4 out of 10 (40%) patients from the HP group (more specifically, 0 from the HR and 4 out of 6 from the HL group), 6 out of 10 (60%) from the GP group, and 3 out of 20 (15%) from the C group. The subjects, who failed the on-road assessment and the reasons for failure are listed in Table 6.2.

Each subject is represented by an identifier, which is composed by the abbreviation of the participant's group (HL, HR, GP, C) and a unique identification number.

HL01	Difficulties with gap judgment, lane keeping, speed, and left turns.
C02	Difficulties with lane keeping.
C12	Difficulties following the speed limit and inappropriate scanning.
HL15	Difficulties with lane keeping and inappropriate scanning.
HL27	Difficulties with scanning, inadequate reaction to dangerous situations and following the traffic signs.
C28	Difficulties with lane keeping and left turns. Difficulties at crossroads.
HL33	Difficulties following the speed limit and with scanning.
GP63	Difficulties with gap selection, following the speed limit, and turning. Inadequate reaction to dangerous situations. Inappropriate scanning.
GP65	Difficulties following the speed limit.
GP67	Difficulties with lane keeping and scanning. Disregarded the right of way. Difficulties following the speed limit.
GP73	Difficulties with scanning and lane keeping. Intervention by the driving instructor.
GP75	Difficulties with lane keeping. Jumped a red light.
GP79	Difficulties with scanning and following traffic signs.

Table 6.2: List of participants who failed the on-road driving test and main reasons for failure.

6.2.2 Analysis of driving skill parameters

Table 6.3 presents the evaluation of the driving skill parameters. These parameters were compared for different subject subgroups using a one-way ANOVA test. Figures 6.5 and 6.6 present a detailed analysis of the differences between the subject subgroups regarding the parameters *lane keeping*, *head*, and *shoulder movements*.

Lane keeping: Patients who failed the driving task (P_f) performed significantly worse than control subjects who passed (C_p) ($p < 0.01$, Table 6.3). Lane keeping performance was significantly worse for GP_f than GP_p and GC_p ($p < 0.05$, Table 6.3). Furthermore, HP_f performed significantly worse than HC_p ($p < 0.05$, Table 6.3, Figure 6.5). This finding suggests that binocular visual field defects relates to difficulties in lane keeping.

Speed: All subject subgroups showed adequate performance regarding this parameter, and no significant difference was found between patients and controls subjects.

Gap judgment: P_f showed significantly worse gap judgment ability than C_p ($p < 0.05$, Table 6.3). This result indicates that binocular visual field defect can lead to difficulties in keeping a safe distance to moving or parked cars. There was no significant difference between the subgroups $\{GC_p, GP_p, GP_f\}$ and $\{HC_p, HR_p, HL_p, HP_f\}$.

	$\{C_p, P_p, P_f\}$	$\{GC_p, GP_p, GP_f\}$	$\{HC_p, HR_p, HL_p, HP_f\}$
Lane keeping	**	*	*
Speed	n.s.	n.s.	n.s.
Gap judgment	*	n.s.	n.s.
Scanning	*	n.s.	n.s.
Head movements	***	***	***
Shoulder movements	***	***	*

Table 6.3: Driving skills for control subjects who passed the driving assessment (C_p), patients who passed (P_p), patients who failed (P_f), glaucoma control subjects who passed (GC_p), glaucoma patients who passed (GP_p) and glaucoma patients who failed (GP_f), HVFD control subjects who passed (HC_p), right-sided HVFD patients who passed (HR_p), left-sided HVFD patients who passed (HL_p) and HVFD patients who failed (HP_f). Statistical comparisons were made between groups with p-values $p < 0.05$ (*), $p < 0.01$ (**), $p < 0.001$ (***). The short notation n.s. stands for non-significant differences. The significance level was adjusted using a Bonferroni correction to an alpha-level of 0.05 for multiple comparisons.

Scanning: Regarding scanning and attention to other traffic participants or signs, patients who failed (P_f) displayed significantly reduced scanning activity in comparison to control subjects who passed the test C_p ($p < 0.05$, Table 6.3). This result suggests that binocular visual field defects negatively effect the scanning behavior.

Head and shoulder movements: Subgroup analysis revealed that patients who failed the driving assessment (P_f) performed significantly less exploratory head and shoulder movements than control subjects C_p and patients who passed the driving test P_p ($p < 0.001$, Table 6.3). Similarly, GC_p and GP_p performed significantly more head and shoulder movements than GP_f ($p < 0.001$, Figure 6.5). Subgroup analysis of HVFD patients showed significantly more head movements in HC_p than HP_f ($p < 0.001$, Table 6.3). HR_p and HL_p also performed more head movements than HP_f ($p < 0.01$, Figure 6.6). Regarding shoulder movements, HP_f performed significantly less shoulder movements than HC_p ($p < 0.05$, Table 6.3).

6.2.3 Analysis of gaze-related parameters

Table 6.4 presents the one-way ANOVA results of the comparison of gaze-related parameters between the different subject subgroups.

HGA: Contrary to what was expected, no significant difference was found between the participant subgroups regarding the horizontal gaze activity.

PGP: There was no significant difference between the subject subgroups regarding the proportion of gazes in percent (PGP) beyond the 30° and 60° area of the visual field. However, patients who passed the driving test (P_p) performed significantly more glances

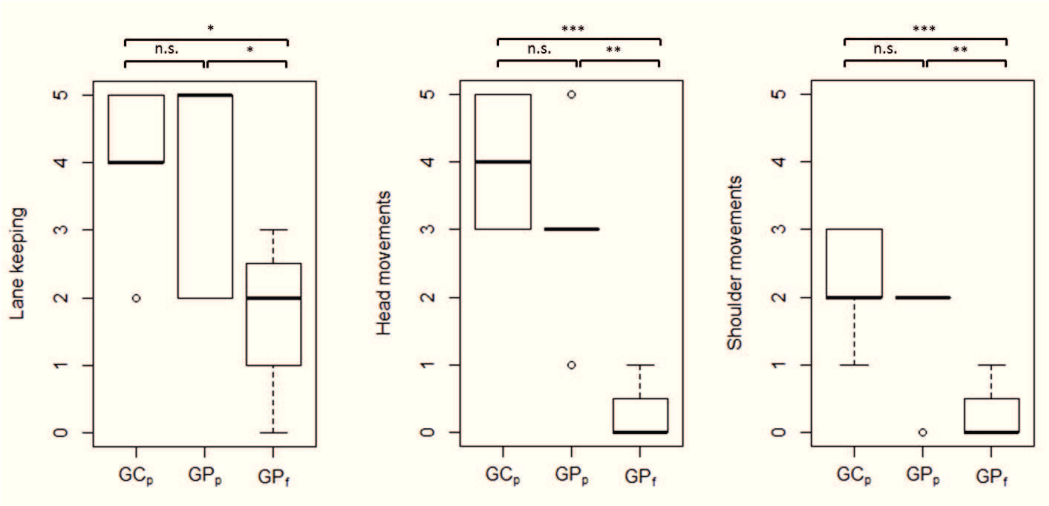

Figure 6.5: Comparison of driving skill parameters for glaucoma control subjects who passed (GC_p), glaucoma patients who passed (GP_p), and glaucoma patients who failed (GP_f) the driving assessment. Left: Comparison of lane keeping performance. Middle: Comparison of head movements. Right: Comparison of shoulder movements.

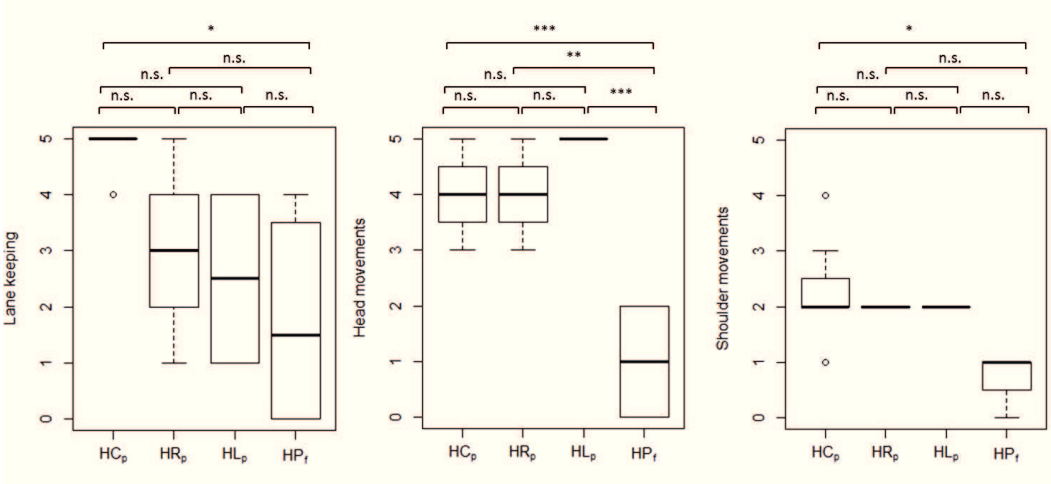

Figure 6.6: Comparison of driving skill parameters for HVFD control subjects who passed (HC_p), right-sided HVFD patients who passed (HR_p), left-sided HVFD patients who passed (HL_p), and HVFD patients who failed (HP_f) the driving assessment. Left: Comparison of lane keeping performance. Middle: Comparison of head movements. Right: Comparison of shoulder movements.

	$\{C_p, P_p, P_f\}$	$\{GC_p, GP_p, GP_f\}$	$\{HC_p, HR_p, HL_p, HP_f\}$
HGA	n.s.	n.s.	n.s.
PGP beyond 30°	n.s.	n.s.	n.s.
PGP beyond 60°	n.s.	n.s.	n.s.
PGP towards VFD	*	n.s.	n.s.
HGD L2	n.s.	n.s.	n.s.
HGD L1	n.s.	n.s.	n.s.
HGD C	*	n.s.	n.s.
HGD R1	n.s.	n.s.	n.s.
HGD R2	n.s.	n.s.	n.s.

Table 6.4: Gaze-related parameters for control subjects who passed the driving assessment (C_p), patients who passed (P_p), patients who failed (P_f), glaucoma control subjects who passed (GC_p), glaucoma patients who passed (GP_p) and glaucoma patients who failed (GP_f), HVFD control subjects who passed (HC_p), right-sided HVFD patients who passed (HR_p), left-sided HVFD patients who passed (HL_p) and HVFD patients who failed (HP_f). Statistical comparisons were made between groups with p-values $p < 0.05$ (*), $p < 0.01$ (**), $p < 0.001$ (***). The short notation n.s. stands for non-significant differences. The significance level was adjusted using a Bonferroni correction to an alpha-level of 0.05 for multiple comparisons.

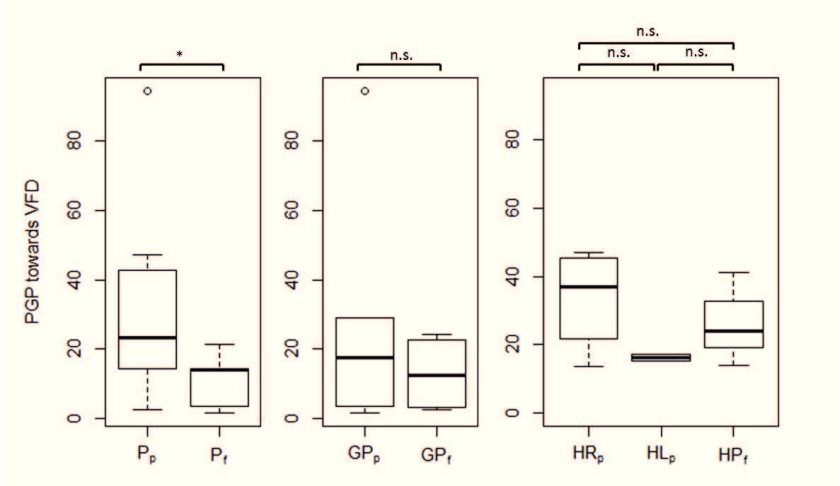

Figure 6.7: Left: Comparison of the proportion of glances in percent (PGP) towards the VFD between patients who passed (P_f) and patients who failed (P_f). Middle: Comparison of PGP towards VFD between glaucoma patients who passed (GP_p) and glaucoma patients who failed (GP_f). Right: Comparison of PGP towards VFD between patients with right-sided HVFDs who passed (HR_p), patients with left-sided HVFDs who passed (HL_p), and patients with HVFDs who failed (HP_f).

towards their visual field defect than patients who failed (P_f) ($p < 0.05$, Table 6.4 and Figure 6.7). Figures 6.8 and 6.9 present the values for PGP towards the visual field defect for glaucoma (GP) and HVFD patients (HP), respectively. For HVFD patients, no strong

correlation between the PGP towards the VFD and the VFD size could be found (Pearson's correlation coefficient: $r = 0.5312$). Stronger correlations could be found for the subgroups HL and HR (Pearson's correlation coefficient for HL: $r = 0.6320$ and for HR: $r = 0.8019$). The strongest correlation between the size of the VFD and the PGP towards it revealed the group GP ($r = 0.9611$). Both Figures 6.8 and 6.9 show that even large visual field defect areas can be compensated by means of exploratory eye and head movements.

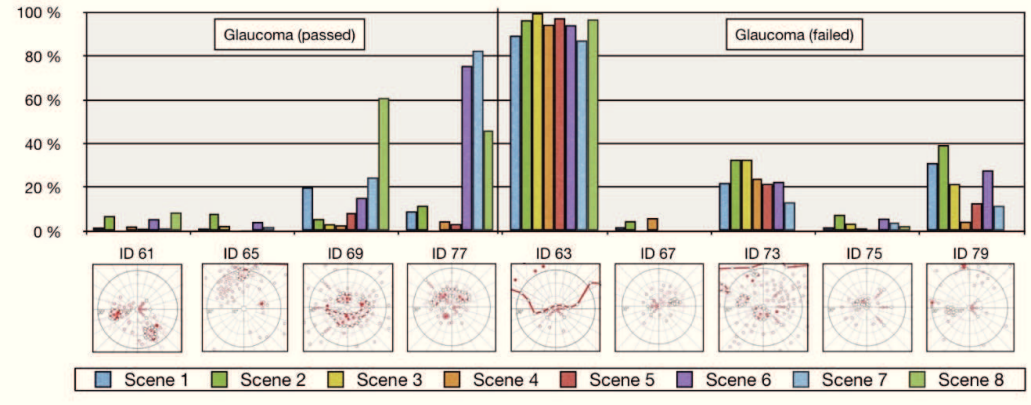

Figure 6.8: The proportion of gazes in percent (PGP) towards the VFD for the group of glaucoma patients. For each of the eight road scenes, the upper panel shows the PGP of each subject. The lower panel shows the corresponding VFD tested by binocular semi-automated kinetic perimetry. The red line represents the border of the homonymous scotoma.

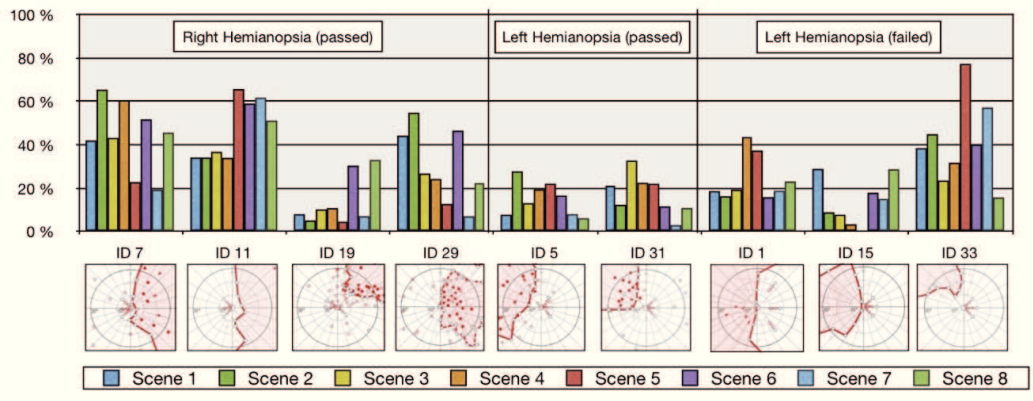

Figure 6.9: The proportion of gazes in percent (PGP) towards the VFD for the group of HVFD patients. For each of the eight road scenes, the upper panel shows the PGP of each participant. The lower panel shows the corresponding VFD tested by binocular semi-automated kinetic perimetry. The red line represents the border of the homonymous scotoma.

HGD: With respect with the previously defined areas of interest L2, L1, R1 and R2 (see Figure 6.4), no significant difference in the horizontal gaze distribution could be found (Table 6.4). However, patients who passed the test focused significantly longer on the central area of the visual field than patients who failed the test ($p < 0.05$, see Table 6.4).

6.2.4 Scanpath analysis of an exemplary hazardous situation

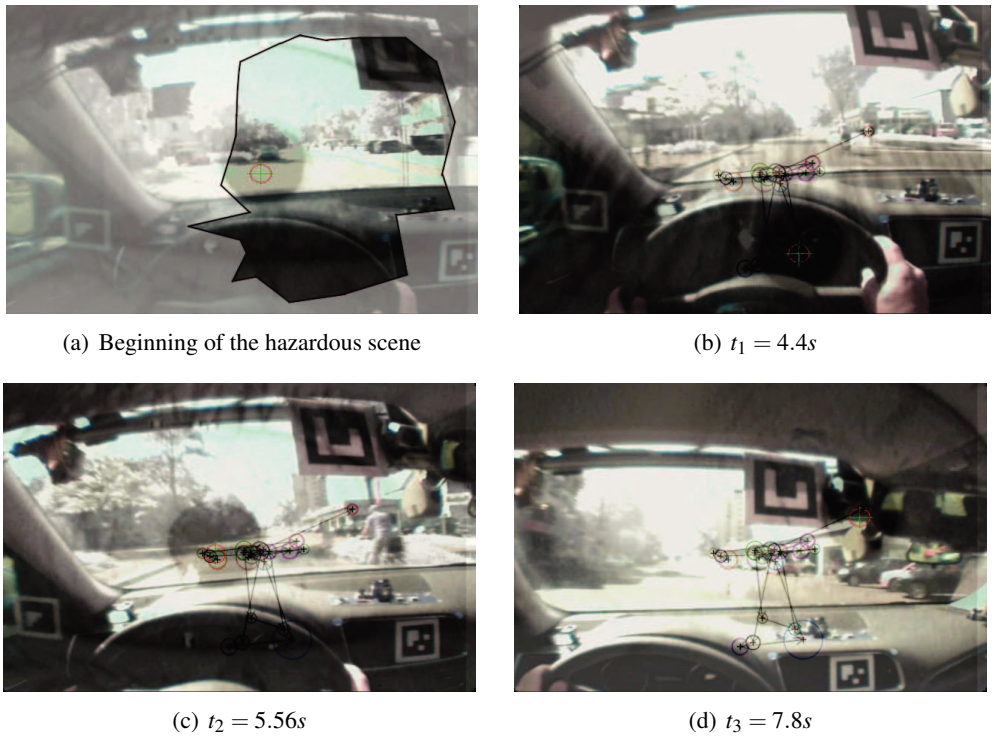

(a) Beginning of the hazardous scene

(b) $t_1 = 4.4s$

(c) $t_2 = 5.56s$

(d) $t_3 = 7.8s$

Figure 6.10: Scanpath computation for the analysis of the viewing behavior of a driver with a left-sided HVFD during a hazardous situation: (a) a video frame at the beginning of the hazardous scene. The clear area within the overlaid polygon represents the intact visual field of the patient. The blurred area represents the area of the visual field defect, where no visual perception occurs. The red circle with the green cross denotes the detected pupil position. (b) a video frame showing the hazardous scene at a later point in time $t_1 = 4.4s$. (c) a video frame at $t_2 = 5.56s$. The hazardous situation arises as a cyclist enters the scene from the right side of the road. At this point in time, the driver was looking at the speedometer. Unaware of the cyclist, this participant has driven very close to the cyclist. In order to avoid an accident, the driving instructor has intervened and alerted the driver. (d) a video frame at $t_3 = 7.8s$. In consequence, the participant made a saccade toward the mirror. Note that the overlaid visual scanpath in (b), (c), and (d) corresponds to the visual search behavior of the subject over the whole time span starting from the beginning of the hazardous scene in (a). Due to the impaired visual field and a poor visual exploration capability, the driver did not perceive the cyclist, which he also admitted afterwards. It is interesting to notice, that the visual field defect of this driver is on the left side of the visual field, but the cyclist was approaching from the right side. However, being aware of his visual field defect, the driver focuses primarily on the left side (i.e., for a longer time). In this case, the compensation of his visual field defect demands so much attention that the subject begins to disregard his healthy side of the visual field. The exploration strategy of this subject is ineffective. According to our findings, a long duration of gazes in the area of the visual field defect interferes with the driving performance. In contrast, an effective exploration strategy consists of frequent but short glances towards the visual field defect area. This subject failed the driving assessment.

Hazardous scenes were analyzed based on visual scanpath computations. A visual scanpath consists of a series of fixations, saccades, and smooth pursuits, which were detected from the raw eye-tracking data by the algorithm presented in Chapter 5. Within the scanpath (see Figure 6.10) each fixation cluster is visualized by a circle, where the circle midpoint corresponds to the location of the centroid of the fixation cluster; the larger the circle, the longer the fixation duration.

Figure 6.10 illustrates how the scanpath computation can be employed to analyze the driver's viewing behavior in hazardous situations. The driver in that example suffers from a left-sided HVFD, i.e., the participant is blind on the left side of the visual field. A thorough analysis of the exemplary hazardous situation represented in Figure 6.10 is described in the caption of the figure.

6.3 Discussion

In this section we summarize the main findings of the presented study and put them in the context of related studies.

Pass and failure rates A considerable number of patients with binocular visual field defects managed to pass the driving test. Six out of ten HVFD patients and four out of ten glaucoma patients were rated as fit to drive by the driving examiner, although they did not meet the 120° horizontal visual field requirement. In comparison, three out of twenty control subjects failed the on-road assessment. For two of them this was mainly due to speeding. The third subject failed because of inappropriate parking distance and speeding.

Previous studies have reported pass rates of drivers with HVFDs that range from 17% [155] to 73% [165]. The high variability in these reports can be attributed to different experimental settings, variability in the types of defects, and the applied rating. The success rates of the patients involved in our study are in line with these studies.

Driving skills Unsafe driving behavior in the our study was attributed to poor lane keeping, difficulties in gap judgment, and inadequate scanning behavior (defined as scanning and attention to other traffic participants or signs), see Table 6.2. More specifically, with respect to these parameters, we found out that patients who failed performed significantly worse than subjects who passed the driving assessment, see Table 6.3, Figure 6.5, and Figure 6.6. These findings are well in line with findings from previous studies, which have reported that poor steering control, difficulties in lane keeping and gap judgment, and inadequate detection of potential blindside hazards are the primary reasons for failing the driving tests [16, 17, 18, 19, 53, 143, 144, 156, 165].

Influence of the visual field defect size and location on driving performance Furthermore, in agreement with previous on-road and simulator studies [109, 165], we found out that the extent of the visual field defect does not necessarily lead to a degradation

in driving performance, because some patients are able to compensate their defects by means of exploratory shoulder, head, and eye movements.

For example, when comparing the driving performance of the HVFD patients with the largest visual field defects (ID01, ID07, ID11 in Figure 6.9), it can be seen that the subject with ID01 (left-sided HVFD) failed, whereas the subjects with IDs 07 and 11 (both suffering from a right-sided HVFD) passed the driving test, although the extent of the individual visual field defect of each of the above subjects is of similar size. However, all failed HVFD subjects suffered from a left-sided defect, which is associated with right hemispheric lesions. In addition, we found out that patients with left-sided HVFDs showed more difficulties in traffic observation, lane keeping, gap selection, and speed than patients with right-sided HVFDs. Thus, the side of the HVFD seems to have an effect on the driving ability. Note, however, that in light of the small number of patients suffering from a left-sided HVFD, the above hypothesis should be considered with care. In fact, previous studies that included a larger number of participants did not find significant differences in driving performance between patients with left- and right hemispheric lesions [16, 109, 143, 165, 172]. Additional research is necessary in order to deliver further insights on the influence of the side of the lesion on driving performance.

A strong association between the extent of the visual field defect (see Figure 6.8) and the fitness to drive could not be found for the group of glaucoma patients either. Our findings are well in line with previous studies with glaucoma patients [92, 145].

Visual exploration strategy We found significant differences in the visual exploration strategy between patients who passed and patients who failed the driving assessment:

- Patients who passed the driving test (P_p with the subgroups GP_p, HR_p, and HL_p) performed significantly more head and shoulder movements and received higher ratings regarding scanning activity than patients who failed the driving test (see Table 6.3, Figure 6.5, and Figure 6.6).
- In addition, patients who passed the driving test (P_p), showed a significantly higher proportion of gazes (PGP) towards their visual field defect than patients who failed (P_f), see Table 6.4 and Figure 6.7.
- As indicated by the horizontal gaze distribution in the central 20° area of the visual field (HGD C), patients rated as fit to drive, focused for a significantly longer time on the central area of the visual field than patients who failed the test, see Table 6.4.

These findings suggest that an adequate driving performance of patients with binocular visual field defects is associated with active scanning of (i.e., short but frequent glances towards) the area of the visual field defect and a focus on the central area of the visual field.

Note that this is the first on-road study where eye tracking was employed to assess the visual exploration. The above findings confirm the hypothesis of previous on-road studies

with HVFD patients [165] that effective scanning of the area of the visual field defect is associated with superior driving performance. Furthermore, the results of our study are also in line with prior simulator studies [51, 109], which have employed eye movement analysis by means of eye tracking.

Gaze patterns of glaucoma patients during driving tasks have been subject of few studies. In a hazard perception test [30] was reported that glaucoma patients made more saccades when viewing driving scenes than control subjects. In another study, which examined traffic gap judgment and eye movements [28], no significant difference in saccade amplitudes between glaucoma patients and control subjects could be found. In our study, we found no differences regarding the eye movement parameters between glaucoma patients who passed and glaucoma patients who failed the driving assessment. However, this may be due to the small sample size, since the PGP towards the visual field defect was significantly higher for patients who passed the test, when all patients (glaucoma and HVFD patients) were analyzed as a group. Interestingly, for glaucoma patients we found a correlation between the PGP towards the visual field defect and its size. Head and shoulder movements were also more pronounced in the case of glaucoma patients who passed the driving test; thus highlighting the importance of active exploration for the compensation of visual field defects.

Possibilities for further improvement Note that despite the considerable total number of participants in our study (40 subjects), the number of participants in some of the subgroups was relatively small to derive significant differences between them (e.g., between left- and right-sided HVFD patients). For such subgroups, further studies involving a larger number of subjects would have to be conducted. Furthermore, for the detailed analysis of further eye movement parameters (e.g., saccade amplitude, frequency of smooth pursuits, etc.) mobile eye trackers at higher sampling rates would have to be employed. A better detection of the exact pupil position during driving, would lead to an improved scanpath analysis. Despite the above suggestions for improvement, our study has revealed many important insights on the impact of visual field defects on driving performance.

6.4 Conclusion

The most important insight gained from this study is that patients with binocular visual field defects can compensate their visual impairment, if they perform effective exploratory head and eye movements. An effective exploration strategy consists of a primary focus on the central area of the visual field and frequent glances towards the area of the visual field defect.

The above insight indicates that a driving ban for patients with binocular visual field defects is not always necessary. Rather an automated, adaptive, and individual driving assistance can help such patients maintain their mobility. A driving assistance system in

this context would have to analyze the driver's viewing behavior in alignment with the driving scene and smoothly guide the driver's gaze over the scene for a better exploration.

All the scanpath analysis methods employed in this study are geared towards the individual scanpath analysis in an online fashion. Together with the study that will be presented in the next chapter, the results hint at the feasibility of a driving assistance system such as the one mentioned above.

7 Feasibility of the online detection of assistance need in a driving simulator study

According to the findings from the on-road study that was presented in the previous chapter, patients with binocular visual field defects can compensate their visual impairment, if they perform effective exploratory head and eye movements. Instead of being banned from driving, an automated, adaptive driving assistance system could help such patients maintain their mobility. A prerequisite for such a driving system is the reliable detection of hazardous objects that might be overlooked by the driver.

The main focus of this chapter is on the applicability of the methods that were presented throughout this thesis to the online analysis of the driver's visual scanpath, with the goal to detect potential traffic hazards. The viability of the methods was evaluated in a driving simulator study with patients suffering from binocular visual field defects. Section 7.1 will introduce the methodology and setting that have been used in this study. The main findings regarding the driving performance of the subjects are summarized in Section 7.2. Section 7.3 will describe how the scene information and the visual scanpath of the driver were aligned to detect overlooked objects. The viability of the methods will be presented and discussed in Section 7.4, and Section 7.5 will conclude this chapter.

7.1 Study materials and setting

7.1.1 Participants

All subjects involved in this simulator study were a subset of the subjects that participated in the on-road study that was described in detail in Chapter 6. Overall, twenty-seven eligible subjects (with mean age of 57 ± 10 years) absolved the simulated drive. 14 of these subjects were patients suffering from binocular visual field defects (8 HVFD patients and 6 glaucoma patients) and 13 were control subjects. 3 HVFD patients had a right-sided defect, the remaining 5 had a left-sided HVFD. Due to the extent of the visual field defect, none of the patients met the legal requirement for driving.

The research study was approved by the Institutional Review Board of the University of Tübingen (Germany) and was performed according to the Declaration of Helsinki. Following verbal and written explanation of the experimental protocol, all subjects gave their written consent, with the option of withdrawing from the study at any time.

7.1.2 Driving simulator

The experiment was conducted in the moving-base driving simulator [170] shown in Figure 7.1(a) at the Mercedes-Benz Technology Center in Sindelfingen, Germany. The facility allows simulating acceleration forces in all directions with up to 1g into the direction of a twelve-meter long rail. As depicted in Figure 7.1(b), the cabin contained a real car body (Mercedes S class with automatic transmission) amidst a 360° projected virtual reality. The car body was oriented perpendicular to the rail. Thus curve and lane changing movements were simulated most realistically, while acceleration and braking resulted in a movement that was often described as diving. All in all, acceleration, sound effects, and car environment contributed to a close-to-realistic driving experience.

(a) (b)

Figure 7.1: The moving base driving simulator; (a) the entire cabin is mounted on a hexapod, moving along the 12m rail resulting in up to 1g acceleration force, (b) the car body inside the hexapod and the virtual reality projection around it. Figures were provided by Daimler AG.

7.1.3 Driving course

The driving route had an overall length of 37.5 km and contained rural as well as urban areas with different speed limits up to 100 km/h. The average driving time for the whole course was 39 min (± 3 min).

Ten hazardous traffic situations, e.g., pedestrians suddenly appearing behind parking cars and trying to cross the road or risky overtaking maneuvers, were induced at predefined positions of the driving course. Figure 7.2 shows an example of such a hazardous situation that arises as a pedestrian tries to cross the road from the left. In this case, if the driver does not react to the appearance of the pedestrian, the simulation avoids the crash, e.g., by having the pedestrian quickly leap backwards. Similar crash avoidance strategies are simulated for all other hazards; hence, (additional) psychological stress of the driver can be mitigated.

(a) (b)

Figure 7.2: Scenes from a simulated drive: (a) a pedestrian intending to cross the road from the left side and (b) a white car coming from the right side.

Position (km)	Traffic hazard
9.5	Pedestrian crossing from the left
15.7	Overtaker on the left curve
24.9	Overtaker on the right curve
30.7	Pedestrian crossing from the right
31.6	Lane blocked by a truck
32.4	Swing-out from the right
33.9	Car crossing from the left
35.1	Car crossing from the right
36.8	Pedestrian crossing from the right
37.5	Pedestrian crossing from the left

Table 7.1: Description of traffic hazards and their occurrence position in the driving course.

More specifically, the driving course consisted of three parts, each with a different design. The first five kilometers of the course were designed to enable the adjustment of the driver to the virtual environment and her responsiveness of the car. The course began with a simple straight road without oncoming traffic and became slowly more complex as it turned into an urban scenario, where oncoming traffic became successively denser and traffic signs more frequent. This session served as an opportunity for the online classification method from Chapter 5 to learn an initial visual behavior model, with parameters adjusted to the current driver. In the second part of the course, which had a length of 25.7 km, a more realistic scenario was simulated. It contained also the first four hazardous situations. Representing typical driving scenarios, this second part of the course allowed the assessment of the driving performance of the subjects, i.e., in terms of the

ability to keep an adequate position within the lane, the ability to follow the speed limits, etc. The third part of the course had a length of 6.8 km and was the most demanding part, as it contained six hazardous situations occurring shortly after each other. A description of the traffic hazards and their position in the driving course is presented in Table 7.1. Figure 7.3 presents the traffic scenario at each of the hazardous situations.

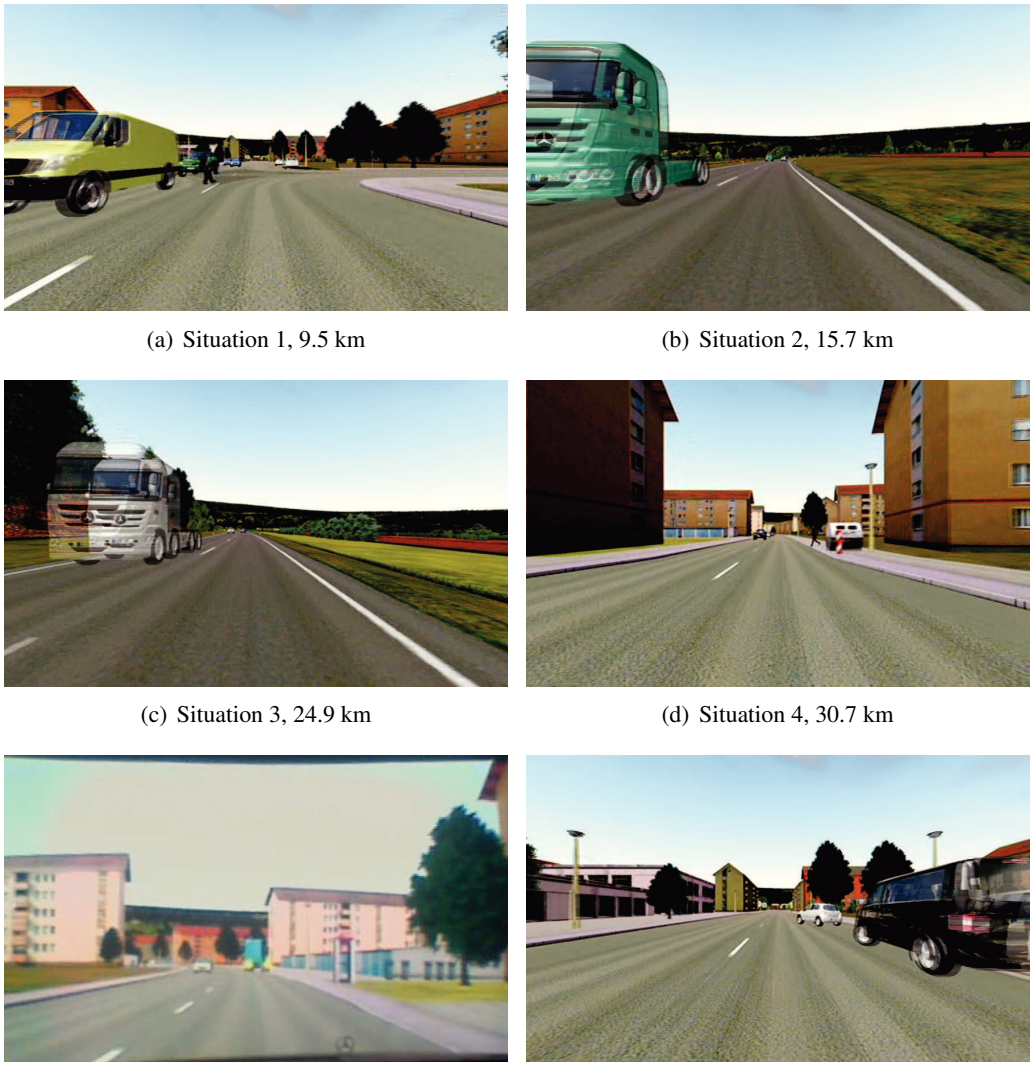

(a) Situation 1, 9.5 km

(b) Situation 2, 15.7 km

(c) Situation 3, 24.9 km

(d) Situation 4, 30.7 km

(e) Situation 5, 31.6 km

(f) Situation 6, 32.4 km

Figure 7.3: Virtual reality simulation of the hazardous situations in the order of their occurrence in the driving course.

(h) Situation 7, 33.9 km

(i) Situation 8, 35.1 km

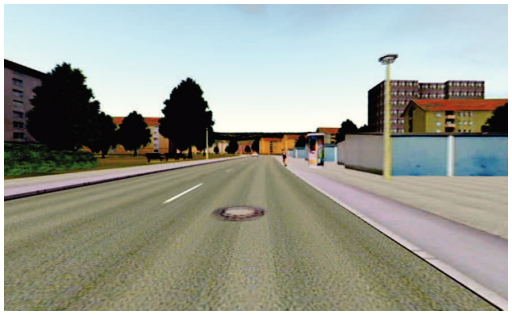

(j) Situation 9, 36.8 km

(k) Situation 10, 37.5 km

Figure 7.3 (continued)

7.1.4 Eye and head tracking

During the drive, eye movements were recorded by a head-mounted Dikablis eye-tracking device [35]. This device was already employed in the previous on-road study and is described in detail in Section 6.1.3.

The head position and orientation was measured using an infrared laser-based 3D tracking system [4] that allows head tracking at very high precision. The sensor was attached to a head band; the receiver was mounted over the passenger's seat. The sampling rate was 240 Hz. The subjects reported that the eye and head tracker did not restrict the head movements and driving ability.

7.2 Analysis of the driving performance

Although the driving behavior of the subjects that participated in this study was already analyzed in the on-road study from Chapter 6, we repeated the analysis with respect to the parameters presented in Section 6.1.4 (e.g., lane keeping ability, scanning, gap judgment, etc.). In contrast to the on-road study, where the drive absolved by each subject was unique in the sense that each subject was faced with different traffic conditions, the driving simulator ensured the same conditions and scenarios for all drivers. As with the on-road study (see Chapter 6), the driving performance was evaluated by a driving examiner

according to the standard criteria of driving license tests in Germany. The detailed results of this analysis are reported in [77, 78]. Many of the findings of this study confirm the results of the previous on-road study. Therefore, we give here only a summary of the main findings:

- Seven out of 14 subjects with binocular visual field defects passed the driving assessment: three out of six patients suffering from glaucoma, and four out of eight patients suffering from HVFD. Only one control subjects failed the driving task. Thus, 50% of the patients were able to pass the driving test without abnormalities.
- As with the on-road study (see Chapter 6), unsafe driving behavior was attributed to difficulties in lane keeping, in identification of traffic signs, and inappropriate scanning behavior.
- As with the on-road study (see Chapter 6), we found no correlation between the driving performance and the time since the diagnosis of the visual field impairment. Furthermore, we found no correlation between the driving performance and the size of the visual field defect area.
- HVFD patients drove slower than their controls. This may have several reasons. One reason might be the lack of driving experience, since they had quited driving due to their visual field impairment. It also might be associated with the fact that these subjects, being aware of their visual impairments, intuitively drove slower in order to gain longer reaction time in case of hazardous situations. For glaucoma patients, we found a strong correlation between speed reduction and the pass rate.
- As with the on-road study (see Chapter 6), patients who passed the driving assessment performed significantly more head and eye movements than patients who failed.

The above findings confirm once again that patients with binocular visual field defects can compensate their visual field impairment, if they perform effective exploratory head and eye movements.

7.3 Alignment of the driving scene with the visual scanpath of the driver

Annotation of the objects on the scene The spatial extent and the position of the traffic hazards was manually annotated using bounding boxes. For this purpose, the hazardous situations were analyzed starting from the moment when the hazardous objects entered the driving scene and up to the moment when the hazardous situation was resolved (e.g., the driver reacted to the approaching hazard or the simulation resolved the hazardous situation). The annotation was performed manually and frame-wise on the video recordings of the driving scene.

Scanpath computation of the driver The visual scanpath of the driver was analyzed in an online fashion based on the Bayesian mixture model and Principal Component Analysis (PCA) presented in Chapter 5. After the separation of fixation clusters from saccades by the Bayesian mixture model, fixation clusters were distinguished from smooth pursuits by means of the PCA-based approach.

The spatial extent of the points in a fixation or smooth pursuit cluster was approximated by an ellipse with axes defined by the length of the two largest principal components (see Figure 7.4).

Alignment of the driving scene and the AOIs of the driver The resulting bounding boxes were matched with the classified eye-tracking data. Whenever a fixation or a smooth pursuit cluster intersected the bounding box enclosing the hazardous object (see Figure 7.4), a traffic hazard was considered as seen by the driver. Four possible scenarios exist:

(i) *The driver looked at the traffic hazard and reacted to it*: This was the case whenever the bounding box enclosing the traffic hazard was intersected by a fixation or a smooth pursuit cluster and the driver reacted adequately to the upcoming danger, e.g., by braking.

(ii) *The driver looked at the traffic hazard but did not react to it*: This was the case whenever the bounding box enclosing the traffic hazard was intersected by a fixation or a smooth pursuit cluster of the driver, but the driver did not show any reaction to the approaching hazard.

(iii) *The driver overlooked the traffic hazard and did not react to it*: This was the case whenever there was no intersection between the bounding box enclosing the traffic hazard and the driver's fixation clusters, and the driver did not react to the hazardous situation.

(iv) *The driver overlooked the traffic hazard but reacted adequately to it*: This was the case whenever the bonding box was not intersected by a fixation cluster but the driver reacted adequately to the upcoming hazard.

In addition, we were interested to see whether the perception of traffic hazards by the driver can be predicted by aligning the scanpath analysis of the eye-tracking data with annotated hazards on the driving scene. In this context, the above categories can be interpreted as follows: Situations from category (i) correspond to true positives, situations from category (ii) correspond to false positives, situations from category (iii) correspond to true negatives, and situations from category (iv) correspond to false negatives.

7.4 Analysis of the alignment with focus on hazardous situations

In total, there were 140 hazardous situations, i.e., 10 for each of the 14 subjects with binocular visual field defects. However, some of the study participants aborted the driving session due to motion sickness. Thus, we were only able to analyze 120 out of 140 hazardous situations in detail. For each of these situations, the visual scanpath of the driver and the information from the driving scene were aligned (as described in Section 7.3) to identify whether the driver perceived the approaching traffic hazard. Table 7.2 presents the results of this analysis:

		Situations
Driver looked at the traffic hazard and reacted	TP	103
Driver looked at the traffic hazard but did not react	FP	5
Driver overlooked the traffic hazard and did not react	TN	4
Driver overlooked the traffic hazard but reacted nevertheless	FN	8

Table 7.2: Analysis of all hazardous situations based on the alignment of the visual scanpath of the driver with information from the corresponding driving scene.

In 103 situations, in which the hazard was considered as perceived (i.e., an intersection between the fixation cluster and the bounding box occurred), the driver reacted by performing a braking or an obstacle avoidance maneuver. An example of a successful intersection between the driver's gaze and the bounding box is shown in Figure 7.4. In 4 hazardous situations, the bounding box was not intersected by a fixation or smooth pursuit cluster and no reaction to the situation happened. In a real-world scenario, these situations would have led to accidents, probably with fatal consequences.

Figure 7.4: A car appears on the left of the driving scene and is about to cut the driver's way. The red bounding box around the approaching hazard and the driver's fixation cluster are shown. Once the bounding box is intersected by the fixation cluster, the traffic hazard is marked as perceived, highlighted by the green bounding box.

In 5 situations, the bounding box was intersected by a fixation or smooth pursuit cluster, but the driver did not react ("looking but not acting" cases). Again, in reality, such situations would have led to accidents. "Looking but not acting" cases were also reported in [41], where the gaze of the (healthy-sighted) drivers was aligned with the on-road events to monitor the attention of the driver. There might be several reasons for this behavior. As driving does not only involve proper visual functioning but also a series of cognitive processes, e.g., attentive mechanisms, memory, etc., [80], looking in the direction of an object of interest may not always be sufficient for an adequate reaction. However, in this study, such a behavior could also be related to missing driving experience, since these subjects had quited driving or reduced it due to their visual field defects.

In 8 situations, the bounding box was not intersected by a fixation cluster of the driver, but the driver reacted nevertheless. Obviously, these hazards were perceived by the driver, even though the driver did not explicitly look at them. The general assumption while driving is that the visual perception of scene features such as signs, pedestrians, and obstacles requires foveated vision (i.e., explicit fixation of the object of interest) [41]. Although peripheral vision is considered as sufficient for some subtasks, such as keeping the vehicle centered in the lane [142], in [85] was reported that peripheral vision is insufficient for the detection of traffic hazards. This means, that to have seen a traffic hazard, the driver must have fixated it. Our findings are in disagreement with the above assumption.

We also found that the side of the road from which a traffic hazard approaches does not interfere with the driver's response to the hazard. In addition, we found that 6 out of 9 cases where the driver did not react to the hazardous object concerned the first hazard presentation (see Table 7.1). In consequence, a higher alertness level could be observed for the remainder of the driving course.

There are two questions that arise from looking at the data from Table 7.2:

- ***How reliable are the proposed techniques with respect to predicting whether the driver has seen a traffic hazard?*** To answer this question, one can derive the following values that characterize the prediction quality: a *precision* of 95.3%, an *accuracy* of 89.1% and a *recall* (sensitivity) of 92.8%.
- ***How would a driver be assisted in an automated way based on these findings?*** Note, that in order to answer this question we should acknowledge that we are in a typical empirical risk minimization scenario, where there is relatively sparse information on the critical situations (e.g., 4 true negatives, 5 false positives, and 8 false negatives) and the loss in comparable real-world situations (e.g., driver overlooks the hazard and does not react) might be immense. The reason for the low numbers in these cases (fortunately) is a natural one: Every driver in the study was concentrated to perform as well as possible; this is similar to real-world driving scenarios, where drivers try to be concentrated, being aware of the consequences of an accident. Given the high potential loss, a driving assistance system that

would make use of our techniques could use a three-tiered assistance strategy. For cases where the system predicts that the driver has seen the traffic hazard (i.e., the object was fixated or pursued by the driver's gaze), the system could gently display information about the hazard (e.g., position, type of hazard, etc.) and thus increase the driver's awareness without distracting her. In case the driver does not react to the hazard in time, the system should intervene to prevent the accident (e.g., through automated braking). For those cases where the system predicts that the driver has not seen the upcoming hazard, the driver's gaze could be guided towards the hazard by means of visual or acoustic stimuli. If the driver does not react in time, the system should intervene to avoid the accident. Figure 7.5 schematically illustrates the above strategy based on a flow diagram.

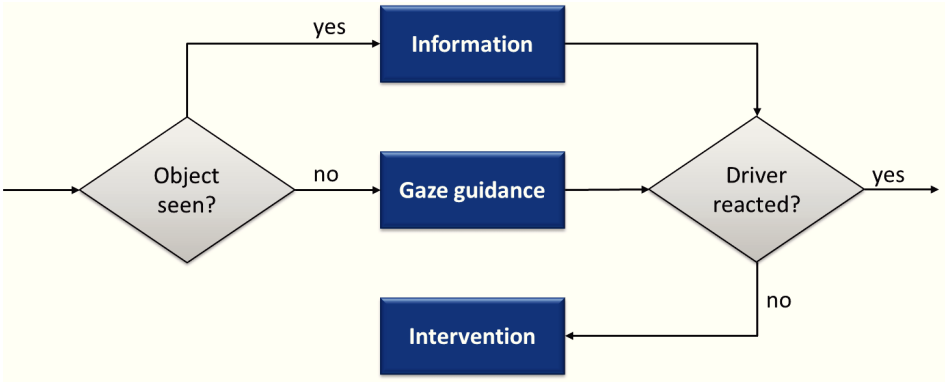

Figure 7.5: Flow diagram illustrating the strategy of a driving assistance system that adapts to the assistance need of drivers with visual impairments.

7.5 Conclusion

This study demonstrated the viability of the proposed methods for the online analysis of the driver's visual scanpath in alignment with the scene information to identify objects that might have been overlooked by the driver. Our method showed high quality in predicting whether the driver has seen a traffic hazard. However, the fixation of an object of interest did not always evoke adequate reaction by the driver. Similarly, an adequate reaction of the driver was not always anticipated by a fixation.

Based on the above findings, we made a suggestion on how a driver could be assisted in order to prevent accidents in cases of overlooked objects. We believe that an adaptive driving assistance system based on this design would help patients with binocular visual field defects maintain their mobility. However, many findings from our studies reach far beyond such patients and concern also healthy-sighted people. Hence, also the methods designed in this work have a broader application.

8 Other application areas

8.1 Visual search behavior of patients with binocular visual field defects in a supermarket search task

In addition to the driving context, we also applied the methods that were developed in this thesis to the analysis of the visual search behavior in a supermarket search task. The goal of this study was to investigate the impact of binocular visual field defects on the individual visual search strategies in everyday life. The subjects had to collect ten specifically marked products in a drugstore as quickly as possible. Their eye movements were recorded by a mobile eye tracker. The main findings of this study are listed below:

- We found no significant differences between patients who passed and patients who failed the task with regard to the number of correctly collected items.
- Due to an effective visual exploration strategy, patients who passed the test needed significantly less time per correctly collected object than patients who failed.
- For this task, frequent glancing towards the visual field defect area and towards the peripheral visual field between 30° and 60° was identified as the main criterion for an effective visual search exploration strategy. Figure 8.1 illustrates the visual search strategy of two HVFD patients.

(a) Subject 1, failed (b) Subject 2, passed

Figure 8.1: Heatmaps showing the distribution of glances of two HVFD patients for the supermarket search task. The warmer the color of a location in the figure, the longer the observation time on that location. The impaired area of the visual field was derived from perimetric examination and was superimposed with the images as the gray area. While Subject 1 focused mainly on the healthy area of the visual field, Subject 2 showed wider exploration and, thus, could compensate for the visual field defect.

These findings confirm the main findings from the on-road and the driving simulator study (Chapter 6 and 7); namely, that the impact of binocular visual field defects on the everyday visual search activities is highly individual and can be compensated through effective visual exploration strategies. Furthermore, this study demonstrated that the methods that were developed can have a broader application than the one in the context of driving.

8.2 Assessing the Exploratory Field of View (EFOV)

Our studies with patients suffering from binocular visual field defects showed that a good exploration capability is decisive for a good performance in visual search tasks. In order to quantify the visual exploration capability, which cannot be captured by standard perimetric measurements, we developed a new testing method, named the *Exploratory Field of View* (EFOV) test [147].

In contrast to usual perimetric examinations, where the subject has to keep the eyes fixated on a stimulus, during EFOV eye movement are allowed, i.e., when a stimulus is presented, the subject is allowed to move her eyes, in order to find and fixate it. The eye movements performed to find and fixate the stimulus are recorded and analyzed. Figure 8.2(a) and 8.2(b) present the EFOV results of Subjects 1 and 2 (who participated in the supermarket search task) from Figure 8.1, respectively.

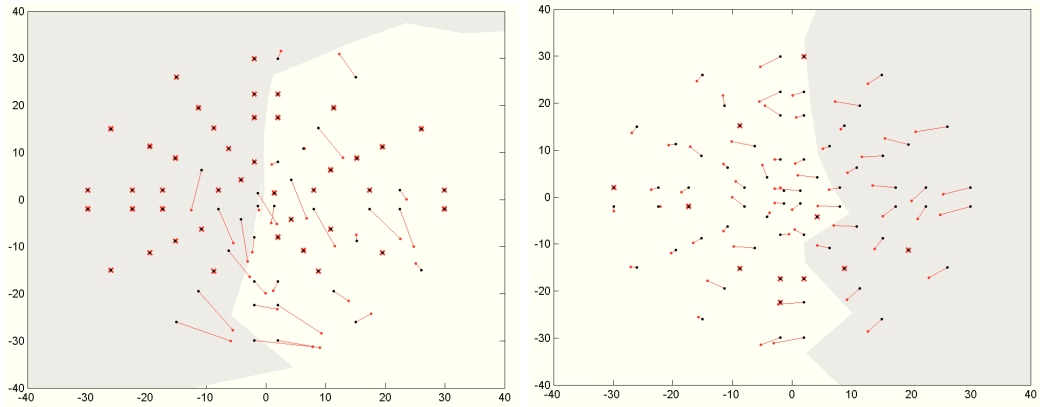

(a) Subject 1, poor exploration (b) Subject 2, good exploration

Figure 8.2: EFOV results of the HVFD patients from Figure 8.1. As before, the gray area in the images represents the impaired visual field area of the subjects; it was derived from standard perimetric examinations. The black dots represent the stimuli locations, whereas the red dots correspond to the locations of the subject's fixations. The presented stimulus (black dot) and its corresponding fixation point (red dot) are connected by a red line. The longer this line, the greater the mismatch between the presented stimulus and the location of the subject's fixation. Hence, the length of the line represents the ineffectiveness of exploration. (a) shows the EFOV result of Subject 1 (from Figure 8.1(b)) with a poor exploration capability. (b) shows the EFOV result of Subject 2 (from Figure 8.1(a)) who showed a better exploration capability.

The EFOV test is currently being evaluated in a pilot study with patients suffering from binocular visual field defects. A sample analysis has already shown the practical benefit of EFOV in quantifying the visual exploration capability. When used complementary to the information on extent and location of the visual field defect, EFOV can help gain more insights on the impact of visual field defects on visual search tasks.

9 Conclusion

On the journey towards the automated recognition of assistance need for drivers with impaired visual field, we have encountered and solved many challenges. The most decisive for the completion of this work were: (i) the analysis of the individual visual field deficit, (ii) the online analysis of the visual search behavior, and (iii) the integration of the above tasks to reliably detect situations in which assistance is needed.

For Challenge (i), we developed the Tübingen Mobile Campimeter (TMC), a light-weight mobile tool, which reliably measures the visual field of the driver. For the accurate detection of the type and extent of the visual field defects (from measurement results), a rule-based classification method that integrates expert knowledge was developed. For Challenge (ii), an online Bayesian method was combined with Principal Component Analysis to detect fixations, saccades, and smooth pursuits by analyzing the scanpath of the driver. Challenge (iii) was approached by aligning the above methods with detailed scene analysis for the detection of traffic objects that might be overlooked by the driver.

All the above methods in combination represent improvements over state-of-the-art techniques in terms of flexibility, adaptivity, and reliability. They were evaluated on real-world data derived from on-road and driving simulator studies with patients with binocular visual field defects and healthy-sighted control subjects. Furthermore, the driving simulator experiments, which were highly encouraged and enabled by our cooperation partner, Daimler AG, served as a feasibility study for the reliable online detection of traffic objects that are seen or overlooked by the driver.

From the point of view of drivers with visual field impairments (who are often banned from driving, as they are considered unfit for this task) the key insight from the above studies is that patients with effective visual exploration strategies can compensate for their visual field defects. This finding supports the underlying hypothesis of this work that patients with binocular visual field defects can maintain their mobility if they are adequately assisted while driving. Along these lines, we proposed a strategy for the gentle automated driving assistance for such patients, which could similarly be used for healthy-sighted drivers.

An automated driving assistance system that is in accordance with our vision, should aim at gentle and unpatronizing gaze guidance. Further work in this direction would have to focus on the prediction of scanpath continuation by leveraging fixation and smooth pursuit clusters. Such a prediction might help gain precious time for the driver to react. Another important question concerns effective ways to gently capture the driver's gaze,

especially for patients with visual field defects. Cross-modal, adaptive stimuli (e.g., based on sound, haptics, vision, etc.) that take the visual deficits and the scene information into account could be employed. The feasibility would have to be tested in detailed multidisciplinary user studies, involving the expertise of engineers, ophthalmologists, acousticians, technicians from the automobile industry, and many more.

In any case, we hope that this interdisciplinary work and its findings will motivate and pave the way for further work in this direction.

List of Figures

List of Tables

List of Abbreviations

ACC Accuracy

ANOVA Analysis of Variance

BMU Best Matching Unit

DLS Differential Luminance Sensitivity

FN False Negatives

FP False Positives

GATE German Adaptive Threshold Estimation

HAC Hierarchical Agglomerative Clustering

HGA Horizontal Gaze Activity

HGD Horizontal Gaze Distribution

HMM Hidden Markov Model

HVFD Homonymos Visual Field Defect

ICA Indipendent Component Analysis

MCC Matthews Correlation Coefficient

PCA Principal Component Analysis

PGP Proportion of Glances in Percent

QE Quantization Error

SOM Self-Organizing Map

SP Specificity

SVM Support vector machines

TE Topographic Error

TMC Tübingen Mobile Campimeter

TN True Negatives

TP True Positives

VF Visual Field

VFD Visual Field Defects

Bibliography

[1] E. Alhoniemi, J. Himberg, J. Parhankangas, and J. Vesanto. Matlab SOM Toolbox. http://www.cis.hut.fi/projects/somtoolbox/. Accessed 16-07-2013.

[2] D. R. Anderson. *Perimetry, With and Without Automation*. C.V. Mosby, St Louis, 2 edition, 1987.

[3] U. M. Anicho and D. Yager. The design of a simple, low cost perimetry instrument for visual field screening in developing regions of the world. In *Perimetry Update 2000/2001*, pages 293–298. Kugler Publications, The Hague, The Netherlands, 2001.

[4] Ascension Technology Corporation. laserBIRD 2. http://www.ascension-tech.com/realtime/laserbird2.php. Accessed 16-07-2013.

[5] E. Aulhorn and H. Karmeyer. Frequency distribution in early glaucomatous visual field defects. *Documenta Ophthalmologica Proceedings Series*, 14:75–83, 1977.

[6] P. Baldi, S. Brunak, Y. Chauvin, C. A. F. Andersen, and H. Nielsen. Assessing the accuracy of prediction algorithms for classification: an overview. *Bioinformatics*, 16(5):412–424, 2000.

[7] B. Bengtsson, D. Bizios, and A. Heijl. Effects of input data on the performance of a neural network in distinguishing normal and glaucomatous visual fields. *Investigative Ophthalmology & Visual Science*, 46(10):3730–3736, 2005.

[8] D. J. Berg, S. E. Boehnke, R. A. Marino, D. P. Munoz, and L. Itti. Free viewing of dynamic stimuli by humans and monkeys. *Journal of Vision*, 9(5):1–15, 2009.

[9] C. Berger, M. Winkels, A. Lischke, and J. Höppner. GazeAlyze: a MATLAB toolbox for the analysis of eye movement data. *Behavioral Research Methods*, 44(2):1–16, 2011.

[10] D. P. Bergsma, J. A. Elshout, G. J. van der Wildt, and A. V. van den Berg. Transfer effects of training-induced visual field recovery in patients with chronic stroke. *Topics in Stroke Rehabilitation*, 19(3):212–225, 2012.

[11] D. P. Bergsma and G. J. van der Wildt. Visual training of cerebral blindness patients gradually enlarges the visual field. *British Journal of Ophthalmology*, 94(1):88–96, 2010.

[12] C. M. Bishop. *Machine Learning and Pattern Recognition*. Springer-Verlag, New York, Inc. Secaucus, NJ, USA, 2006.

[13] D. Bizios, A. Heijl, and B. Bengtsson. Trained artificial neural network for glaucoma diagnosis using visual field data: a comparison with conventional algorithms. *Journal of Glaucoma*, 16(1):20–28, 2007.

[14] P. Blignaut. Fixation identification: The optimum threshold for a dispersion algorithm. *Attention, Perception, & Psychophysics*, 71(4):881–895, 2009.

[15] C. Boden, K. Chan, P. A. Sample, J. Hao, T. Lee, L. M. Zangwill, R. N. Weinreb, and M. H. Goldbaum. Assessing Visual Field Clustering Schemes Using Machine Learning Classifiers in Standard Perimetry. *Investigative Ophthalmology & Visual Science*, 48(12):5582–5590, 2007.

[16] A. R. Bowers, A. J. Mandel, R. B. Goldstein, and E. Peli. Driving with hemianopia, I: Detection Performance in a Driving Simulator. *Investigative Ophthalmology & Visual Science*, 50(11):5137–5147, 2009.

[17] A. R. Bowers, A. J. Mandel, R. B. Goldstein, and E. Peli. Driving with hemianopia, II: lane position and steering in a driving simulator. *Investigative Ophthalmology & Visual Science*, 51(12):6605–6613, 2010.

[18] A. R. Bowers, E. Peli, J. Elgin, G. McGwin Jr., and C. Owsley. On-road driving with moderate visual field loss. *Optometry & Vision Science*, 82(8):657–667, 2005.

[19] A. R. Bowers, M. Tant, and E. Peli. A Pilot Evaluation of On-Road Detection Performance by Drivers with Hemianopia Using Oblique Peripheral Prisms. *Stroke Research and Treatment*, page n. pag., 2012.

[20] D. H. Brainard. The Psychophysics Toolbox. *Spatial vision*, 10(4):433–436, 1997.

[21] L. Brigatti, K. Nouri-Mahdavi, M. Weitzmann, and J. Caprioli. Automatic Detection of Glaucomatous Visual Field Progression with Neural Networks. *Archives of Ophthalmology*, 115(6):725–728, 1997.

[22] A. Bruckmann, N. J. Volpe, J. Paetzold, R. Vonthein, and U. Schiefer. Comparison of advanced visual field defects measured with the Tübingen Mobile Campimeter and the Octopus 101 perimeter. *European Journal of Ophthalmology*, 20(1):149–157, 2010.

[23] G. T. Buswell. *How people look at pictures*. University of Chicago Press, Chicago, 1935.

[24] H. Bynke and A. Heijl. A portable hemianopsia tester. *Acta Ophthalmologica (Copenhagen)*, 54(2):174–184, 1976.

[25] M. Camilli, R. Nacchia, M. Terenzi, and F. Di Nocera. ASTEF: a simple tool for examining fixations. *Behavior Research Methods*, 40(2):373–382, 2008.

[26] Cedrus Corporation. SuperLab. http://www.superlab.com. Accessed 16-07-2013.

[27] F. Chédru, M. Leblanc, and F. Lhermitte. Visual searching in normal and brain-damaged subjects (contribution to the study of unilateral inattention). *Cortex*, 9(1):94–111, 1973.

[28] A. M. Y. Cheong, D. R. Geruschat, and N. Congdon. Traffic gap judgment in people with significant peripheral field loss. *Optometry & Vision Science*, 85(1):26–36, 2008.

[29] T. R. M. Coeckelbergh, W. H. Brouwer, F. W. Cornelissen, and A. C. Kooijman. Predicting practical fitness to drive in drivers with visual field defects caused by ocular pathology. *Human Factors*, 46(4):748–760, 2004.

[30] D. P. Crabb, N. D. Smith, F. G. Rauscher, C. M. Chisholm, J. L. Barbur, D. F. Edgar, and D. F. Garway-Heath. Exploring eye movements in patients with glaucoma when viewing a driving scene. *PloS One*, 5(3):e9710, 2010.

[31] B. Damato and C. Groenewald. Multifixation campimetry on line: a perimeter for the detection of visual field loss using the internet. *British Journal of Ophthalmology*, 87(10):1296–1298, 2003.

[32] A. Duchowski. *Eye tracking methodology: Theory and practice*. Springer, London, 2007.

[33] R. O. Duda, P. E. Hart, and D. G. Stork. *Pattern Classification (2nd Edition)*. Wiley-Interscience, 2 edition, 2000.

[34] J. Elgin, G. McGwin, J. M. Wood, M. S. Vaphiades, R. A. Braswell, D. K. DeCarlo, L. B. Kline, and C. Owsley. Evaluation of on-road driving in people with hemianopia and quadrantanopia. *The American Journal of Occupational Therapy*, 64(2):268–278, 2010.

[35] Ergoneers GmbH. Dikablis and D-Lab Products. http://www.ergoneers.com/de/products/dlab-dikablis/overview.html. Accessed 16-07-2013.

[36] European Union. Directive 2006/126/EC of the European Parliament and of the Council. http://eur-lex.europa.eu/LexUriServ/LexUriServ.do?uri=OJ:L:2006:403:0018:0060:EN:PDF, 2006. Accessed 16-07-2013.

[37] Eyetellect. GazeTracker. http://www.eyetellect.com/gazetracker/. Accessed 16-07-2013.

[38] V. P. Ferrera. Task-dependent modulation of the sensorimotor transformation for smooth pursuit eye movements. *Journal of Neurophysiology*, 84(6):2725–2738, 2000.

[39] W. Fink. Neural attractor network for application in visual field data classification. *Physics in Medicine and Biology*, 49(13):2799–2809, 2004.

[40] P. Flach. *Machine Learning: The art and science of algorithms that make sense of data*. Cambridge University Press, 2012.

[41] L. Fletcher and A. Zelinsky. Driver inattention detection based on eye gaze-road event correlation. *The International Journal of Robotics Research*, 28(6):774–801, 2009.

[42] G. D. Forney Jr. The viterbi algorithm. *Proceedings of the IEEE*, 61(3):268–278, 1973.

[43] J. S. Gilhotra, P. Mitchell, P. R. Healey, R. G. Cumming, and J. Currie. Homonymous visual field defects and stroke in an older population. *Stroke*, 33(10):2417–2420, 2002.

[44] D. R. Gitelman. ILAB: a program for postexperimental eye movement analysis. *Behavioral Research Methods, Instruments and Computers*, 34(4):605–612, 2002.

[45] M. H. Goldbaum. Unsupervised learning with independent component analysis can identify patterns of glaucomatous visual field defects. *Transactions of the Americal Ophthalmological Society*, 103:270–280, 2005.

[46] M. H. Goldbaum, G. J. Jang, C. Bowd, J. Hao, L. M. Zangwill, J. Liebmann, C. Girkin, T. P. Jung, R. N. Weinreb, and P. A. Sample. Patterns of glaucomatous visual field loss in SITA fields automatically identified using independent component analysis. *Transactions of the Americal Ophthalmological Society*, 107:136–144, 2009.

[47] M. H. Goldbaum, P. A. Sample, K. Chan, J. Williams, T. W. Lee, E. Blumenthal, C. A. Girkin, L. M. Zangwill, C. Bowd, T. Sejnowski, and R. N. Weinreb. Comparing machine learning classifiers for diagnosing glaucoma from standard automated perimetry. *Investigative Ophthalmology & Visual Science*, 43(1):162–169, 2002.

[48] M. H. Goldbaum, P. A. Sample, H. White, B. Colt, P. Raphaelian, R. D. Fechtner, and R. N. Weinreb. Interpretation of automated perimetry for glaucoma by neural network. *Investigative Ophthalmololgy & Visual Science*, 35(9):3362–3373, 1994.

[49] C. Haacke, A. Althaus, A. Spottke, U. Siebert, T. Back, and R. Dodel. Long-term outcome after stroke: evaluating health-related quality of life using utility measurements. *Stroke*, 37(1):193–198, 2006.

[50] Haag-Streit AG. OCTOPUS 900 User manual. http://www.haag-streit-usa.com/Portals/0/OCTOPUS%20900_UserManual.pdf, 2008. Accessed 16-07-2013.

[51] J. Hamel, A. Kraft, S. Ohl, S. De Beukelaer, H. J. Audebert, and S. A. Brandt. Driving simulation in the clinic: testing visual exploratory behavior in daily life activities in patients with visual field defects. *Journal of Visualized Experiments*, 67:e4427, 2012.

[52] M. Hayhoe and D. Ballard. Eye movements in natural behavior. *Trends in Cognitive Science*, 9(4):188–194, 2005.

[53] S. A. Haymes, R. P. LeBlanc, M. T. Nicolela, L. A. Chiasson, and B. C. Chauhan. Glaucoma and on-road driving performance. *Investigative Ophthalmology & Visual Science*, 49(7):3035–3041, 2008.

[54] D. B. Henson, S. E. Spenceley, and D. R. Bull. Spatial classification of glaucomatous visual field loss. *British Journal of Ophthalmology*, 80(6):526–531, 1996.

[55] D. B. Henson, S. E. Spenceley, and D. R. Bull. Artificial neural network analysis of noisy visual field data in glaucoma. *Artificial Intelligence in Medicine*, 10(2):99—113, 1997.

[56] K. Holmqvist, M. Nyström, R. Andersson, R. Dewhurst, H. Jarodzka, and J. Van de Weijer. *Eye tracking: A comprehensive guide to methods and measures*. Oxford University Press, 2011.

[57] J. C. Horton. Vision restoration therapy: confounded by eye movements. *British Journal of Ophthalmology*, 89(7):792–794, 2005.

[58] L. Itti. Quantifying the contribution of low-level saliency to human eye movements in dynamic scenes. *Visual Cognition*, 12(6):1093–1123, 2005.

[59] L. Itti and C. Koch. A saliency-based search mechanism for overt and covert shifts of visual attention. *Vision Research*, 40(10-12):1489–1506, 2000.

[60] L. Itti, C. Koch, and E. Niebur. A model of saliency-based visual attention for rapid scene analysis. *IEEE Transactions on Pattern Analysis and Machine Intelligence*, 20(11):1254–1259, 1998.

[61] A. K. Jain, M. N. Murty, and P. J. Flynn. Data clustering: a review. *ACM Computing Surveys*, 31(3):264–323, 1999.

[62] C. A. Johnson and J. L. Keltner. Incidence of visual field loss in 20,000 eyes and its relationship to driving performance. *Archives of Ophthalmology*, 101(3):371–375, 1983.

[63] I. T. Jolliffe. *Principal Component Analysis*. Springer-Verlag, New York, USA, 1986.

[64] C. Jürgens, T. Koch, R. Burth, U. Schiefer, and A. Zell. Classification of perimetric results and reduction of number of test locations using artificial neural networks [arvo abstract nr. 4539]. *Investigative Ophthalmology & Visual Science*, 42(4):846, 2001.

[65] H. O. Karnath and P. Thier. *Neuropsychologie*. Springer Verlag, Berlin, Heidelberg, 2006.

[66] S. Kaski. Data exploration using self-organizing maps. In *Acta Polytechnica Scandinavica: Mathematics, Computing and Management in Engineering Series No 82*, 1997.

[67] E. Kasten, U. Bunzenthal, and B. A. Sabel. Visual field recovery after vision restoration therapy (VRT) is independent of eye movements: an eye tracker study. *Behavioral Brain Research*, 175(1):18–26, 2006.

[68] E. Kasten, S. Wust, W. Behrens-Baumann, and B. A. Sabel. Computer-based training for the treatment of partial blindness. *Nature Medicine*, 4(9):1083–1087, 1998.

[69] D. Keating, E. Mutlukan, A. Evans, J. McGarvie, and B. Damato. A back propagation neural network for the classification of visual field data. *Physics in Medicine and Biology*, 38(9):1263, 1993.

[70] T. Kohonen. The self-organizing map. *Proceedings of the IEEE*, 78(9):1464–1480, 1990.

[71] T. Kohonen, M. R. Schroeder, and T. S. Huang, editors. *Self-Organizing Maps*. Springer-Verlag New York, Inc., Secaucus, NJ, USA, 3rd edition, 2001.

[72] N. Koiava, Y. H. Ong, M. M. Brown, J. Acheson, G. T. Plant, and A. P. Leff. A 'web app' for diagnosing hemianopia. *Journal of Neurology, Neurosurgery & Psychiatry*, 83(12):1222–1224, 2012.

[73] O. V. Komogortsev, S. Jayarathna, D. H. Koh, and S. M. Gowda. Qualitative and quantitative scoring and evaluation of the eye movement classification algorithms. In *Proceedings of the 2010 Symposium on Eye-Tracking Research & Applications*, ETRA '10, pages 65–68, New York, NY, USA, 2010. ACM.

[74] O. V. Komogortsev and A. Karpov. Automated classification and scoring of smooth pursuit eye movements in the presence of fixations and saccades. *Behavior Research Methods*, 45(1):203–215, 2013.

[75] A. Kooijman, W. Brouwer, T. Coeckelbergh, M. Tant, F. Cornelissen, R. Bredewoud, and B. J. M. Melis-Dankers. Compensatory viewing training improves practical fitness to drive of subjects with impaired vision. *Visual Impairment Research*, 6(1):1–27, 2004.

[76] A. Kotecha, A. Spratt, and A. Viswanathan. Visual function and fitness to drive. *British Medical Bulletin*, 87(1):163–74, 2008.

[77] T. C. Kübler, E. Tafaj, M. Bogdan, W. Rosenstiel, U. Schiefer, and E. Papageorgiou. Driving with visual field loss: can exploratory eye and head movements predict successful obstacle recognition? *In Review with: Journal of Vision*, 2013.

[78] T. C. Kübler, E. Tafaj, M. Bogdan, W. Rosenstiel, U. Schiefer, and E. Papageorgiou. Stress-related parameters as a complementary and confirmatory tool for exploratory gaze movements in patients with binocular field loss. *In Review with: Transportation Research Part F: Traffic Psychology and Behaviour*, 2013.

[79] M. F. Land. Vision, eye movements, and natural behavior. *Visual Neuroscience*, 26(1):51–62, 2009.

[80] M. F. Land and B. W. Tatler. *Looking and acting: vision and eye movements in natural behaviour*. Oxford University Press, 2009.

[81] LC Technologies Inc. Eye tracking for research, analysis, human interaction. http://www.eyegaze.com/eye-tracking-research-analysis-human-interaction/. Accessed 16-07-2013.

[82] R. J. Leigh and D. S. Zee. *The neurology of eye movements*. Oxford University Press, 2006.

[83] D. Li, D. Winfield, and D. J. Parkhurst. Starburst: A hybrid algorithm for video-based eye tracking combining feature-based and model-based approaches. In *Proceedings of the 2005 IEEE Computer Society Conference on Computer Vision and Pattern Recognition*, CVPR'05, pages 1–8, San Diego, CA, USA, 2005. IEEE.

[84] B. Machner, A. Sprenger, D. Kömpf, T. Sander, W. Heide, H. Kimmig, and C. Helmchen. Visual search disorders beyond pure sensory failure in patients with acute homonymous visual field defects. *Neuropsychologia*, 47(13):2704–2711, 2009.

[85] M. Maltz and D. Shinar. Imperfect in-vehicle collision avoidance warning systems can aid drivers. *Human Factors: The Journal of the Human Factors and Ergonomics Society*, 46(2):357–366, 2004.

[86] A. Mandahl. Red square test for visual field screening. a sensitive and simple bedside test. *Acta Ophthalmologica (Copenhagen)*, 72(6):683–687, 1994.

[87] P. Mangiameli, S. K. Chen, and D. West. A comparison of som neural network and hierarchical clustering methods. *European Journal of Operational Research*, 93(2):402–417, 1996.

[88] J. Markoff. Google cars drive themselves, in traffic. *The New York Times*, 10:A1, 2010.

[89] T. Martin, M. E. Riley, K. N. Kelly, M. Hayhoe, and K. R. Huxlin. Visually-guided behavior of homonymous hemianopes in a naturalistic task. *Vision Research*, 47(28):3434–3446, 2007.

[90] G. W. McConkie. Evaluating and reporting data quality in eye movement research. *Behavior Research Methods & Instrumentation*, 13(2):97–106, 1981.

[91] G. McGwin Jr., A. Mays, W. Joiner, D. K. DeCarlo, T. A. Hall, and C. Owsley. Visual field defects and the risk of motor vehicle collisons among patients with glaucoma. *Investigative Ophthalmology & Visual Science*, 46(12):4437–4441, 2005.

[92] G. McGwin Jr., A. Mays, W. Joiner, D. K. DeCarlo, S. McNeal, and C. Owsley. Is glaucoma associated with motor vehicle collision involvement and driving avoidance? *Investigative Ophthalmology & Visual Science*, 45(11):3934–3939, 2004.

[93] T. Minka, J.M. Winn, J. P. Guiver, and D. A. Knowles. Infer.NET 2.5. MicrosoftResearchCambridge.http://research.microsoft.com/infernet, 2012. Accessed 16-07-2013.

[94] I. Mueller, H. Mast, and B. A. Sabel. Recovery of visual field defects: a large clinical observational study using vision restoration therapy. *Restorative Neurology and Neuroscience*, 25(5-6):563–572, 2007.

[95] E. Mutlukan. Computerised campimetry with static dark-on-bright stimuli. *Documenta Ophthalmologica*, 85(4):335–350, 1993.

[96] E. Mutlukan, B. E. Damato, and J. L. Jay. Clinical evaluation of a multi-fixation campimeter for the detection of glaucomatous visual field loss. *British Journal of Ophthalmology*, 77(6):332–338, 1993.

[97] E. Mutlukan and D. Keating. Visual field interpretation with a personal computer based neural network. *Eye*, 8(3):321–323, 1994.

[98] E. Mutlukan and G. L. Spaeth. A portable visual field screener using a back-projection method with a laser pointer in the diagnosis of glaucomatous field loss. In *Perimetry Update 2000/2001*, pages 277–281. Kugler Publications, The Hague, The Netherlands, 2001.

[99] Neurobehavioral Systems, Inc. Presentation. http://www.neurobs.com. Accessed 16-07-2013.

[100] J. Nevalainen, E. Krapp, J. Paetzold, I. Mildenberger, D. Besch, R. Vonthein, J. L. Keltner, C. A. Johnson, and U. Schiefer. Visual field defects in acute optic neuritis - distribution of different types of defect pattern, assessed with threshold-related supraliminal perimetry, ensuring high spatial resolution. *Graefe's Arch Clin Exp Ophthalmol*, 246(4):599–607, 2007.

[101] D. Noton and L. W. Stark. Eye movements and visual perception. *Scientific American*, 224(6):34–43, 1971.

[102] K. Nouri-Mahdavi, N. Nassiri, A. Giangiacomo, and J. Caprioli. Detection of visual field progression in glaucoma with standard achromatic perimetry: A review and practical implications. *Graefe's Archive for Clinical and Experimental Ophthalmology*, 249(11):1593–1616, 2011.

[103] A. Nuthmann and J. M. Henderson. Object-based attentional selection in scene viewing. *Journal of Vision*, 10(8):20, 2010.

[104] C. Owsley, K. Ball, G. McGwin, M. E. Sloane, D. L. Roenker, M. F. White, and E. T. Overley. Visual processing impairment and risk of motor vehicle crash among older adults. *JAMA: The Journal of the American Medical Association*, 279(14):1083–1088, 1998.

[105] A. Pambakian, S. Mannan, T. Hodgson, and C. Kennard. Saccadic visual search training: a treatment for patients with homonymous hemianopia. *Journal of Neurology Neurosurgery and Psychiatry*, 75(10):1443–1448, 2004.

[106] A. L. Pambakian and C. Kennard. Can visual function be restored in patients with homonymous hemianopia? *British Journal of Ophthalmology*, 81(4):324–328, 1997.

[107] A. L. Pambakian, D. S. Wooding, N. Patel, A. B. Morland, C. Kennard, and S. K. Mannan. Scanning the visual world: a study of patients with homonymous hemianopia. *Journal of Neurology Neurosurgery & Psychiatry*, 69:751–759, 2000.

[108] E. Papageorgiou, G. Hardiess, H. Ackermann, H. Wiethoelter, K. Dietz, H. A. Mallot, and U. Schiefer. Collision avoidance in persons with homonymous visual field defects under virtual reality conditions. *Vision Research*, 52(1):20–30, 2012.

[109] E. Papageorgiou, G. Hardiess, H. A. Mallot, and U. Schiefer. Gaze patterns predicting successful collision avoidance in patients with homonymous visual field defects. *Vision Research*, 65:25–37, 2012.

[110] E. Papageorgiou, G. Hardiess, F. Schaeffel, H. Wiethoelter, H. O. Karnath, H. Mallot, B. Schoenfisch, and U. Schiefer. Assessment of vision-related quality of life in patients with homonymous visual field defects. *Graefe's Archive for Clinical and Experimental Ophthalmology*, 245(12):1749–1758, 2007.

[111] J. W. Peirce. PsychoPy–Psychophysics software in Python. *Journal of Neuroscience Methods*, 162(1-2):8–13, 2007.

[112] V. S. Pelak, M. Dubin, and E. Whitney. Homonymous Hemianopia: a critical analysis of optical devices, compensatory training, and NovaVision. *Current Treatment Options in Neurology*, 9(1):41–47, 2007.

[113] G. Pölzlbauer. Survey and comparison of quality measures for self-organizing maps. In *Proceedings of the Fifth Workshop on Data Analysis*, WDA '04, pages 67–82, Sliezsky dom, Vysoké Tatry, Slovakia, 2004. Elfa Academic Press.

[114] D. A. Pomerleau. ALVINN: an autonomous land vehicle in a neural network. In D. S. Touretzky, editor, *Advances in Neural Information Processing Systems 1*, pages 305–313. San Francisco, CA: Morgan Kaufmann, 1989.

[115] C. M. Privitera and L. W. Stark. Scanpath theory, attention, and image processing algorithms for predicting human eye fixations. In L. Itti, G. Rees, and J. Tsotsos, editors, *Neurobiology of Attention*, pages 269–299, 2005.

[116] Psychology Software Tools, Inc. E-Prime 2. http://www.pstnet.com/eprime.cfm. Accessed 16-07-2013.

[117] D. Purves. *Neuroscience*. Sinauer, 4th edition, 2008.

[118] H. A. Quigley and A. T. Broman. The number of people with glaucoma worldwide in 2010 and 2020. *British Journal of Ophthalmology*, 90(3):262–267, 2006.

[119] R Development Core Team. *R: A Language and Environment for Statistical Computing*. R Foundation for Statistical Computing, Vienna, Austria, 2009.

[120] L. Racette and E. J. Casson. The impact of visual field loss on driving performance: evidence from on-road driving assessments. *Optometry & Vision Science*, 82(8):668–674, 2005.

[121] R. S. Ramrattan, R. C. W. Wolfs, S. Panda-Jonas, J. B. Jonas, D. Bakker, H. A. Pols, A. Hofman, and P. T. V. M. de Jong. Prevalence and Causes of visual field loss in the elderly and associations with impairment in daily functioning: The Rotterdam Study. *Archives of Ophthalmology*, 119(12):1788–1794, 2001.

[122] J. Reinhard, A. Schreiber, U. Schiefer, E. Kasten, B. A. Sabel, S. Kenkel, R. Vonthein, and S. Trauzettel-Klosinski. Does visual restitution training change absolute homonymous visual field defects? A fundus controlled study. *British Journal of Ophthalmology*, 89(1):30–35, 2005.

[123] F. J. Rowe, H. Sueke, and S. D. Gawley. Comparison of damato campimetry and humphrey automated perimetry results in a clinical population. *British Journal of Ophthalmololy*, 94(6):757–762, 2010.

[124] G. S. Rubin, E. S. W. Ng, K. Bandeen-Roche, P. M. Keyl, E. E. Freeman, S. K. West, and And The See Project Team. A prospective, population-based study of the role of visual impairment in motor vehicle crashes among older drivers: The See Study. *Investigative Ophthalmology & Visual Science*, 48(4):1483–1491, 2007.

[125] D. Salvucci and J. Goldberg. Identifying fixations and saccades in eye-tracking protocols. In *Proceedings of the 2000 Symposium on Eye Tracking Tesearch & Applications*, ETRA '00, pages 71–78, New York, NY, USA, 2000. ACM.

[126] J. San Agustin, H. Skovsgaard, E. Mollenbach, M. Barret, M. Tall, D. W. Hansen, and J. P. Hansen. Evaluation of a low-cost open-source gaze tracker. In *Proceedings of the 2010 Symposium on Eye-Tracking Research & Applications*, ETRA '10, pages 77–80, New York, NY, USA, 2010. ACM.

[127] A. Santella and D. DeCarlo. Robust clustering of eye movement recordings for quantification of visual interest. In *Proceedings of the 2004 Symposium on Eye Tracking Research & Applications*, ETRA '04, pages 27–34, New York, NY, USA, 2004. ACM.

[128] D. Sauter, B. J. Martin, N. Di Renzo, and C. Vomscheid. Analysis of eye tracking movements using innovations generated by a Kalman filter. *Medical and biological Engineering and Computing*, 29(1):63–69, 1991.

[129] U. Schiefer, J. P. Pascual, B. Edmunds, E. Feudner, E. M. Hoffmann, C. A. Johnson, W. A. Lagreze, N. Pfeiffer, P. A. Sample, F. Staubach, R. G. Weleber, R. Vonthein, E. Krapp, and J. Paetzold. Comparison of the new Perimetric "German Adaptive Threshold Estimation (GATE)" strategy with conventional Full-Threshold and SITA standard Strategies. *Investigative Ophthalmology & Visual Science*, 50(1):488–494, 2009.

[130] U. Schiefer, H. Wilhelm, and W. Hart. *Clinical Neuro-Ophthalmology: A Practical Guide*. Springer Verlag, 2008.

[131] R. Schmid, H. Luedtke, B. J. Wilhelm, and H. Wilhelm. Pupil campimetry in patients with visual field loss. *European Journal of Neurology*, 12(8):602–608, 2005.

[132] T. Schulte, H. Strasburger, E. Muller-Oehring, E. Kasten, and B. Sabel. Automobile driving performance of brain-injured patients with visual field defects. *American Journal of Physical Medicine & Rehabilitation*, 78(2):136–142, 1999.

[133] A. C. Schütz, D. I. Braun, and K. R. Gegenfurtner. Eye movements and perception: a selective review. *Journal of Vision*, 11(9):1–30, 2011.

[134] Seeing Machines Inc. faceLab 5. http://www.seeingmachines.com/product/facelab/. Accessed 16-07-2013.

[135] SensoMotoric Instruments GmbH. SMI BeGaze Eye Tracking Analysis Software. http://www.smivision.com/en/gaze-and-eye-tracking-systems/products/begaze-analysis-software.html. Accessed 16-07-2013.

[136] SensoMotoric Instruments GmbH. SMI Eye Tracking Glasses. http://www.smivision.com. Accessed 16-07-2013.

[137] F. Shic, B. Scassellati, and K. Chawarska. The incomplete fixation measure. In *Proceedings of the 2008 Symposium on Eye Tracking Research & Applications*, ETRA '08, pages 111–114, New York, NY, USA, 2008. ACM.

[138] K. Sippel, E. Tafaj, K. Aehling, M. Heister, W. Rosenstiel, U. Schiefer, and E. Papageorgiou. Binocular visual field loss and its impact on visual exploration: A supermarket study. *Submitted to: Vision Research*, 2013.

[139] R. R. Sokal and F. J. Rohlf. *Biometry*. WH Freeman & Co, New York, 1995.

[140] A. Sommer, J. M. Tielsch, J. Katz, H. A. Quigley, J. D. Gottsch, J. Javitt, and K. Singh. Relationship between intraocular pressure and primary open angle glaucoma among white and black americans. the baltimore eye survey. *Archives of Ophthalmology*, 109(8):1090–1095, 1991.

[141] SR Research Ltd. EyeLink 1000 and EyeLink II. http://www.sr-research.com/index.html. Accessed 16-07-2013.

[142] H. Summala, T. Nieminen, and M. Punto. Maintaining lane position with peripheral vision during in-vehicle tasks. *Human Factors: The Journal of the Human Factors and Ergonomics Society*, 38(3):442–451, 1996.

[143] J. Szlyk, M. Brigell, and W. Seiple. Effects of age and hemianopic visual field loss on driving. *Optometry and Vision Science*, 70(12):1031–1037, 1993.

[144] J. Szlyk, C. L. Mahler, W. Seiple, D. P. Edward, and J. T. Wilensky. Driving performance of glaucoma patients correlates with peripheral visual field loss. *Journal of Glaucoma*, 14(2):145–150, 2005.

[145] J. Szlyk, L. Myers, Y. Zhang, L. Wetzel, and R. Shapiro. Development and assessment of a neuropsychological battery to aid in predicting driving performance. *Journal of Rehabilitation Research and Development*, 39(4):483–496, 2002.

[146] E. Tafaj, J. Dietzsch, M. Bogdan, U. Schiefer, and W. Rosenstiel. Reliable classificatin of visual field defects in automated perimetry using clustering. In *Proceedings of the 8th IASTED International Conference on Biomedical Engineering*, BIOMED '11, 2011.

[147] E. Tafaj, S. Hempel, M. Heister, K. Aehling, J. Dietzsch, F. Schaeffel, W. Rosenstiel, and U. Schiefer. A new method for assessing the exploratory field of view (efov). In *Proceedings of the 6th International Conference on Health Informatics*, HEALTHINF 2013, 2013.

[148] E. Tafaj, G. Kasneci, W. Rosenstiel, and M. Bogdan. Bayesian online clustering of eye movement data. In *Proceedings of the Symposium on Eye Tracking Research & Applications*, ETRA '12, pages 285–288, New York, NY, USA, 2012. ACM.

[149] E. Tafaj, T. Kübler, J. Peter, U. Schiefer, M. Bogdan, and W. Rosenstiel. Vishnoo - an open-source software for vision research. In *Proceedings of the 24^{th} IEEE International Symposium on Computer-Based Medical Systems*, CBMS' 11, pages 1–6. IEEE, 2011.

[150] E. Tafaj, T. C. Kübler, G. Kasneci, W. Rosenstiel, and M. Bogdan. Online classiffication of eye tracking data for automated analysis of traffic hazard perception. In *Proceedings of the 23rd International Conference on Artificial Neural Networks*, ICANN 2013, 2013.

[151] E. Tafaj, K. Sippel, K. Aehling, M. Heister, W. Rosenstiel, U. Schiefer, and E. Papageorigiou. Driving with binocular visual field loss? a study on a supervised on-road parcours with simultaneous eye tracking. *In Review with: Plos One*, 2013.

[152] E. Tafaj, C. Uebber, J. Dietzsch, U. Schiefer, M. Bogdan, and W. Rosenstiel. Introduction of a Portable Campimeter Based on a Laptop/Tablet PC. In *Proceedings of the 19th Imaging and Perimetry Society*, IPS '10, 2010.

[153] E. Tafaj, C. Uebber, J. Dietzsch, U. Schiefer, M. Bogdan, and W. Rosenstiel. Mobile and fast detection of visual field defects for elderly drivers as a necessary input into driver assistance systems for mobility maintenance. In *GMM-Fachbericht Band 64, AmE 2010 - Automotive meets Electronics*, pages 47–52. VDE VERLAG GmbH, 2010.

[154] P. N. Tan, M. Steinbach, and V. Kumar. *Introduction to Data Mining*. Addison Wesley, 2005.

[155] M. Tant, W. Brouwer, F. Cornelissen, and A. Kooijman. Driving and visuospatial performance in people with hemianopia. *Neuropsychological rehabilitation*, 12(5):419–437, 2002.

[156] M. L. Tant, F. W. Cornelissen, A. C. Kooijman, and W. H. Brouwer. Hemianopic visual field defects elicit hemianopic scanning. *Vision Research*, 42(10):1339–1348, 2002.

[157] B. W. Tatler, M. M. Hayhoe, M. F. Land, and D. H. Ballard. Eye guidance in natural vision: reinterpreting salience. *Journal of Vision*, 11(5):5, 2011.

[158] J. F. Taylor. Vision and driving. *Ophthalmic and Physiological Optics*, 7(2):187–189, 1987.

[159] Tobii Technology AB. Eye Tracking for Research and Analysis. http://www.tobii.com/en/eye-tracking-research/global/. Accessed 16-07-2013.

[160] A. Ultsch. Self-organizing neural networks for visualisation and classification. In *Information and classification*, pages 307–313. Springer, 1993.

[161] C. Urmson, J. Anhalt, D. Bagnell, C. Baker, R. Bittner, et al. Autonomous driving in urban environments: Boss and the urban challenge. *Journal of Field Robotics*, 25(8):425–466, 2008.

[162] T. Urruty, S. Lew, N. Ihadaddene, and D. A. Simovici. Detecting eye fixations by projection clustering. *ACM Transactions on Multimedia Computing, Communications, and Applications (TOMCCAP)*, 3(4):1–20, 2007.

[163] J. S. Wani, M. S. Mir, and A. R. Nasti. Automated perimetry: interpreting the data. *Jk-Practitioner*, 12:219–223, 2005.

[164] H. Widdel. Operational problems in analysing eye movements. In A. G. Gale and F. Johnson, editors, *Theoretical and Applied Aspects of Eye Movement Research Selected/Edited Proceedings of The Second European Conference on Eye Movements*, volume 22 of *Advances in Psychology*, pages 21 – 29. North-Holland, 1984.

[165] J. Wood, G. McGwin, J. Elgin, M. Vaphiades, R. Braswell, D. K. DeCarlo, et al. On-road driving performance by persons with hemianopia and quadrantanopia. *Investigative Ophthalmology & Visual Science*, 50(2):577–585, 2009.

[166] J. Wood, G. McGwin, J. Elgin, M. Vaphiades, R. Braswell, D. K. DeCarlo, L. B. Kline, and C. Owsley. Hemianopic and quadrantanopic field loss, eye and head movements, and driving. *Investigative Ophthalmology & Visual Science*, 52(3):1220–1225, 2011.

[167] D. S. Wooding. Fixation maps: quantifying eye-movement traces. In *Proceedings of the 2002 Symposium on Eye Tracking Research & Applications*, ETRA '02, pages 31–36, New York, NY, USA, 2002. ACM.

[168] N. Yamada, P. P. Chen, R. P. Mills, M. M. Leen, M. F. Lieberman, R. L. Stamper, and D. C. Stanford. Screening for glaucoma with frequency-doubling technology and damato campimetry. *Archives of Ophthalmology*, 117(11):1479–1484, 1999.

[169] A. L. Yarbus. *Eye movements and vision*. Plenum Press, New York, 1967.

[170] E. Zeeb. Daimler's New Full-Scale, High-dynamic Driving Simulator–A Technical Overview. In *Proceedings of the Driving Simulator Conference Europe*, pages 157–165. Institut national de recherche sur les transports et leur sécurité, 2010.

[171] X. Zhang, S. Kedar, M. J. Lynn, N. J. Newman, and V. Biousse. Homonymous hemianopia in stroke. *Journal of Neuro-Ophthalmololy*, 26(3):180–183, 2006.

[172] J. Zihl. Visual scanning behavior in patients with homonymous hemianopia. *Neuropsychologia*, 33(3):287–303, 1995.

[173] J. Zihl. *Rehabilitation of visual disorders after brain injury*. Taylor & Francis US, 2010.